Holographic Particle Image Velocimetry of Ink Jet Streams

MCKEAGUE, THOMAS,ANDERSON

Holographic Particle Image Velocimetry of Ink Jet Streams

A thesis submitted in partial fulfilment of the requirements for the degree of Doctor of Philosophy in the University of Durham by,

Anderson McKeague

Department of Chemistry

University of Durham

October 2014

Abstract

Ink jet technology is a rapidly growing and diverse field of research. Ink jets are used to deliver very precise and small (picolitre) volumes of fluid to a surface. Recent advances in ink jet technology demand a better understanding of the dynamics of the fluid during jetting. The aim of this project was to design a method capable of measuring the flow velocities inside ink jet streams. This objective has been achieved by the use of digital holographic particle image velocimetry.

The difficulty with measuring flows inside tightly curved samples is that the refractive index change over the boundary leads to an optical distortion and therefore particles cannot be viewed or tracked reliably. Optical distortion is compensated for by taking advantage of the ability to replay a holographically recorded wave. The light scattered by particles is propagated numerically back through the sample's surface, to form a three-dimensional image in which all refractions at the interface have been accounted for. Three dimensional particle fields are then analysed using custom particle detection and correlation code to extract the displacement of individual particles between exposures, which facilitates the construction of full flow profiles. Holograms were recorded with a simple off-axis holographic microscope, comprising two point sources of divergent light, formed from the same objective lens, acting as the source of illumination and reference light, respectively.

Experiments were conducted on continuous ink jet streams of water issuing from a nozzle with 100 μm diameter. For a few millimetres after the nozzle exit, the jet is cylindrical, it then starts to form swells and necks; the swells continue to grow at the expense of the necks until the jet breaks up into a stream of droplets. Measurements of the stream wise component of velocity have been successful in the cylindrical parts of the jet, in swells and in necks greater than 20 μm in diameter. To my knowledge measurements of particle velocities on fluid jets at this scale have not been accomplished previously.

Acknowledgements

I am indebted to my supervisors Prof. Colin Bain and Prof. Jeremy Coupland for their support, guidance and patience over the course of this project. Thanks are due to Dr. Andrew Wormald for help with holographic reconstructions and Dr. David Woods for help with coding in the early stages of this project. I appreciate the help I have received from the departmental services, especially the machinists in the mechanical workshops who supplied me with some custom parts.

I would also like to thank the members of the Bain group, both past and present, for their kindness, good advice and good company throughout my time here. Particular mention should go to Mario, David, Yan, Celine, Ash and Elin who were always there to share a pint on a Friday night.

I am grateful for the love and support of all my family, without their encouragement I would not have got this far. Finally, a special thanks must go to Ffion for her patience and good humour while I endeavoured to write this up.

Glossary of Symbols

A	Complex amplitude of a scalar field
$\mathbf{A}$	Vector amplitude of the electric field
a	Scalar amplitude
c	Speed of light in a vacuum
$D_{\min}$	Minimum distance between the source and detector in the microscope
$D_{lensless}$	Distance from source to detector in a single point-source microscope
$d_{lensless}$	Distance from source to sample in a single point-source microscope
D	Diffusivity [Chapter 1]
	Distance from point source to detector in the microscope [Chapter 3 onwards]
Dt	Inter-frame time
d	Distance from illumination source to sample in the microscope
E_a	Scalar field in air
E_s	Scalar field in sample
$E_{scattered}$	Scalar field scattered by the sample
$\mathbf{E}$	Electric field
$\mathcal{F}$	Fourier Transform
f	Spatial frequency
G	Green's function
I	Intensity

ID	Inner diameter
i	Complex unit
k	Wavenumber
L	Coherence length [Chapter 2]
	The length of the detector in the microscope [Chapter 3]
	The length scale of a flow [Chapter 6]
$\vec{n}$	Normal unit vector
$\frac{\partial}{\partial n}$	Partial differential in the outward normal direction
NA	Numerical aperture
n	Refractive index
$\boldsymbol{N}$	Normal to a surface
O	Object wave
P_O	Object point source position in the microscope
P_R	Reference point source position in the microscope
P	A point in space
Q	Volume flow rate
$\vec{r}_{surf}$	A set of points on a sample surface
r_{01}	Distance between two points, subscripted 0 and 1 respectively
R	Sample radius
R	Reference wave
r	Radial coordinate [all except Chapter 3]
	Half sample width [Chapter 3]

$\boldsymbol{r}$	Position vector
S	Closed surface of integration
s	Source separation in the microscope
T	Absolute temperature
t	Time
U_0	Scalar field on Π
U_1	Scalar field on Σ
$\bar{u}$	Mean fluid velocity
U	A scalar electric field [Chapter 2]
u	Fluid velocity
v_i	Distance between a lens and image
v_o	Distance between a lens and object
V	Volume of integration
x_a	Axial resolution
x_t	Transverse resolution
x	A spatial coordinate perpendicular to the optical axis (horizontal coordinate in holograms)
y	A spatial coordinate perpendicular to the optical axis (vertical coordinate in holograms)
z	Coordinate along the optical axis
α	Azimuthal angle
∇^2	Laplacian operator
Δ	Pixel pitch
ε_B	Relative error in velocity due to Brownian motion

ϵ_0	Vacuum permittivity
κ	Boltzmann's constant
λ	Wavelength
Ω	Half-angular aperture
ω	Angular frequency [Chapter 2] Bandwidth [Chapter 3]
Π	Plane close to sample
φ	Angle of incidence or refraction of a ray of light (depending on subscript) [Chapter 1] Phase of a scalar field [Chapter 2]
ϕ	Half angle of divergence of the illumination and reference beams in the microscope
Σ_-	Surface just inside the boundary of the sample
Σ_+	Surface just outside the boundary of the sample
Σ	Hologram aperture
θ	Angle of incidence of a reference beam
μ	Dynamic viscosity

Contents

1 Introduction

Liquid jets are used in many industrial applications. They are used extensively within the manufacturing, automotive and agricultural industries to deliver atomised sprays of liquid, where the exact properties of the delivery affect performance, efficiency and longevity of equipment.[1] The breakup of a cylindrical stream of liquid into a series of droplets can be one of the most precise and reproducible flow phenomena. Commercial inkjet technology takes advantage of this to accurately deliver consistent droplets of fluid for applications including graphical printing, 3D rapid prototyping and printing electronic circuits.[2] Improved modelling and the subsequent experimental feedback is necessary for the development of reliable printing rigs for increasingly complex inks. However, the occurrence of a tightly curved interface between a jetted medium and the outside world creates an optical distortion, which hampers the collection of reliable experimental data by traditional velocimetry techniques. The work described in this thesis targets the development of a prototypical system capable of measuring the flow field within a large (full width and several diameters stream-wise) section of a micro-scale liquid jet in a single shot.

The remainder of Chapter 1 discusses liquid jets and the motivation to study inkjet systems, existing fluid velocimetry methods and possible strategies to account for optical distortion at interfaces. I conclude that a holographic method is worth investigating to achieve the goals of this work. In Chapter 2, background information on the behaviour of light and the basics of holography is presented, along with the mathematical framework necessary to manipulate holograms digitally. Chapter 3 details the design of the holographic microscope used to record the raw data. Chapter 4 discusses the numerical methods used to process the recorded holograms. Chapter 5 is an experimental chapter and describes the flow system used to produce the liquid jets. Flow profiles are presented in Chapter 6, showing the internal fluid velocity of a continuous inkjet stream during breakup. Finally, Chapter 7 contains a summary of the work described along with a discussion and conclusions.

1.1 Liquid Jets

The first documented evidence of interest in liquid jets dates back to the 15th century when Leonardo Da Vinci wrote extensively on the behaviour of water in the Codex Leicester.[1] He not only sketched the trajectories of liquid jets flowing out of holes in a vessel full of liquid but also remarked on the cohesion of fluids, deducing that a drop detaches from a dripping tap when gravity overcomes the cohesive forces.

It wasn't until the early 19th century that Laplace and Young[3,4] demonstrated that although the cohesive force, surface tension, is the force holding a drop on a dripping tap; it is also the force that drives the breakup of a collimated jet. This is contrary to the argument given by Mariotte,[1] who built on Da Vinci's ideas and wrongly concluded that a jet only breaks up when the ligament of fluid attaching a droplet to the bulk becomes so thin that it can no-longer hold the droplet's weight. Laplace and Young correctly deduced that breakup happens as the system is driven towards the configuration with the lowest surface area and, the greater the cohesive forces, the faster the breakup occurs.

The breakup of a jet is driven by surface tension. Any small perturbations in the environment of a jet will cause local variations in its diameter. Laplace found that the pressure inside a fluid is inversely proportional to its radius of curvature.[1] Parts of the jet with a smaller radius of curvature have higher internal pressure than parts with a larger radius of curvature. This difference in pressure pumps fluid from the narrower parts of the jet into the neighbouring wider parts; giving rise to 'swells' and 'necks' (figure 1.1). The swells continue to grow at the expense of the necks until the jet breaks up into a stream of drops.

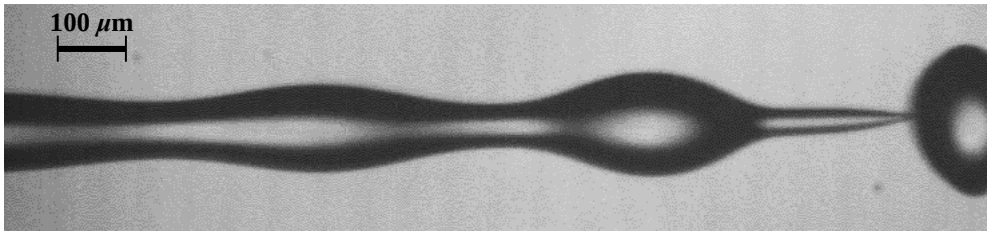

Figure 1.1 A shadowgraph image of a continuous inkjet (CIJ) stream of water. The CIJ nozzle size is 100 μm.[5]

Plateau found that any perturbation that reduces the surface area of a jet is amplified along its length.[6] Further work from Rayleigh added to this simple model by examining the dynamics of the system,[7] concluding that given a spectrum of initial perturbations, the one that has the highest growth rate along the jet will dominate and eventually set the drop size. Taking advantage of this theory, jets can be deliberately perturbed so that a reproducible and regular stream of drops is formed. The ability to deliver discrete and precise quantities of material – particularly at a small scale – makes liquid jets a useful tool in science and industry.

Inkjet printing really began in the 1951 when Siemens developed the first commercial inkjet printer.[8] Today, graphical printing with inkjets is a market worth in excess of $50 billion, and predicted to rise to $85 billion by 2019.[9] In the last 20 years, inkjets have been applied to a huge number of research areas outside of graphical printing. Their uses include printing of metallic, organic and polymeric electronics, rapid prototyping of components in ceramics, waxes, low-molecular weight polymers and UV-curable resins as well as bio-printing of proteins, cells and scaffolds for the prosthetics industry.[10-18]

Inkjet printing is an attractive tool in these industries because of its potential to deliver material simply, with low energy requirements and with very little waste. Low wastage of material is of particular importance in the manufacture of electronics, especially in producing economically viable solar cells – which contain rare elements such as indium and gallium.[12] The organic electronics market is rapidly growing, expected to be worth over $75 billion by 2020, and the possibility of quick and efficient production of organic light emitting diode displays and organic thin-film transistors has meant that inkjets are fast becoming an important area of research in this sector.[13] Other uses of inkjets in the field of electronics involve printing solder onto micro-electronic circuits and printing of magnetic nanoparticles for printed digital memory.

Inkjets are also used in small-scale manufacture; successive layers of material can be built up to form a three dimensional model of a prototype or functional part. It is not yet possible to print high molecular weight polymers; however models can be created from waxes or low-molecular weight polymers as well as ceramics. Functional micro-optical

elements such as arrays of micro lenses and wave guides have been produced by inkjet printing of UV-curable resins. The micro lenses produced by Ishii *et al.* are sized between 20 –140 μm.[14]

As early as 2005, Xu *et al.* were able to print viable mammalian cells using a modified Hewlett Packard printer (HP 55C) and ink cartridge (HP 51626a).[15] Even with such a crude system, the vast majority of the printed cells survived the process, with less than 8 % being lysed during printing. These results are an encouraging step towards the goal of printing whole tissues and whole tissues and research interest continues in this exciting area.[16] Inkjet-printed solid structures also have potential uses in the field of bio-engineering as they can serve as scaffolds on which tissues for use as replacements for damaged biological structures such as blood vessels may be grown.[17]

For all of the examples given previously, inks are printed from small nozzles onto a substrate, which, in some situations, may be a layer of cured or dried ink. Printing is made up of two distinct processes, the formation of individual droplets and the interaction of these droplets with the substrate. It is the formation of well-defined droplets that this project focuses on. The breakup of a filament of liquid into a single, well-defined and reproducible drop, becomes complex when the ink is heavily solid- or polymer- loaded or contains surfactant. A significant amount of modelling work has been done on the breakup of liquid filaments,[18] but no direct measurements of the flow inside a liquid jet have yet been reported. Measurement of the flow inside inkjet streams, will not only help to assess the validity of assumptions made in computational models, but will also help to enhance models for situations where results do not closely follow reality.

Currently, the prevalent non-invasive technique used to measure flows with dimensions ranging from metres to microns is particle image velocimetry (PIV). In PIV, flows must be seeded with tracer particles. The particles are imaged at at least two points in time and their displacements are measured to give a fine-grained velocity map extending over a large area of the imaged flow. PIV, however, can only be directly applied to flows where an accurate photograph of seeding particles can be taken therefore one needs to see the particles and know their position within the volume of a flow. Curved interfaces between media of different refractive index cause refractions that distort

particles images and give uncertainties in their positions. These refractions are particularly extreme in the case of the micro-scale inkjet streams.

The remainder of this chapter will review existing methods of fluid velocimetry as well as techniques used to account for the uncertainties caused by refraction at curved sample boundaries.

1.2 Velocimetry

There exist a number of common techniques used for measuring the velocity of fluids; Pitot tube, hot wire anemometry, laser Doppler anemometry (LDA), particle image velocimetry (PIV) and holographic particle image velocimetry (HPIV). The Pitot tube and hot wire anemometer methods, described elsewhere,[19] are invasive; both techniques involve inserting a probe into a fluid and are therefore inappropriate for measurements on inkjets. Laser Doppler anemometry is non-invasive and provides a point-wise measurement of flow velocity. Incident light is scattered by a particle in the flow and the Doppler shift of the scattered light is measured to give the particle's velocity. The technique has been used to measure flows in millimetric jets previously[20] but, in order to build up a flow map of a large section of a jet, an enormous number of single-point measurements are required.

PIV provides a velocity map of a large area of a flow in a single measurement by imaging a large number of particles and measuring their displacements. PIV can be adapted to microfluidic samples and can even be used to obtain three-component velocimetric data. Holographic PIV (HPIV) is an emerging technique that combines holographic imaging with the principles of PIV. Holograms are two-dimensional recordings that can be used to generate a three-dimensional image. All three components of particle velocity in all three dimensions can be measured in this way. This section will discuss PIV, in particular the enhancements that allow it to be applied at the micro-scale, and HPIV of micro-scale flows.

1.2.1 Particle Image Velocimetry

Particle image velocimetry (PIV) is a non-invasive optical flow measurement technique capable of measuring the speed and direction of flows by conventional imaging. The measurement is obtained from observing particles either added to, or naturally occurring in, the flow.

In PIV, two images of a seeded flow are taken in quick succession (with a known time delay) and the positions of particles in each are compared. The change in the position of particles over a known time gives an estimate of the velocity. PIV was introduced in parallel by Adrian,[21] and Pickering and Halliwell[22] in the late 1980s and has since become a standard technique to measure flows due to the unique ability to yield a fine-grained velocity measurement over the whole field of view of the imaging system. PIV provides a huge improvement over earlier techniques such as laser Doppler anemometry, where velocity can only be measured at a single point.

Experimentally, the flow is seeded with small tracer particles and then illuminated by two successive laser pulses while a specialised digital camera records a pair of images. Figure 1.2 depicts a general PIV set up. The flow is illuminated by a thin sheet of light so that only particles in a single plane are imaged. Light is provided typically by a laser source, either a single double-pulsed laser or a pair of lasers with a tuneable delay. Pulsed lasers are chosen so that the particles are arrested in the recorded images – appearing as dots as opposed to streaks. Since the measured quantity in PIV is the displacements of particles, they must be chosen so that they follow the flow faithfully and their presence does not alter it.

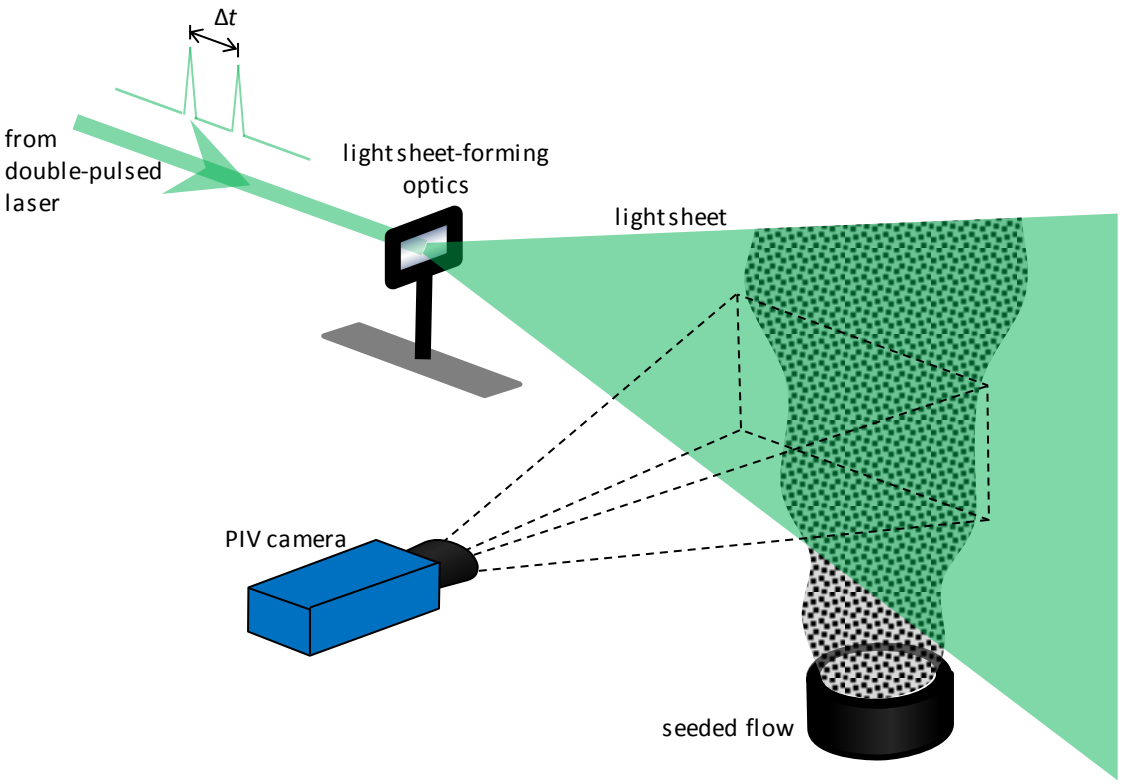

Figure 1.2 General PIV system.

Approximately 10 years after the invention of PIV, users began to apply the general techniques to flows on the micro-scale.[23] This alternative technique is known as μPIV due to certain issues that are unique to the scaled-down version. One such issue is that, in general, the depth of particles illuminated can no-longer be controlled by the thickness of a light sheet. The difficulty in imaging particles in a single plane, with a depth which is small compared to the length-scales of the flow, led some groups to develop confocal μPIV.[42] Others successfully implemented stereoscopic μPIV to obtain information about the third component of velocity.[52] Finally, some workers saw potential in the observation that a lot of information in a volume-illuminated sample comes from particles out of the focal plane of the imaging optics.[61,68] From this, the defocussed methods in μPIV were developed. Defocussed methods rely on the shape and size of the out-of-focus particle blurs to estimate their depth, which facilitates the estimation of a three-component, three-dimensional velocity map. The application of PIV to micro-scale flows is reviewed in subsection 1.2.2.

The holographic recording method has also been applied to PIV; rather than imaging the particles in a flow with a photograph, the scattered light from particles is recorded on a hologram. Holograms can be reconstructed optically or, if they are captured on a digital device, numerically to generate a three-dimensional image of the particle field. With holographic PIV, particles can be located and tracked in three-dimensions. Although modern digital cameras are far more user friendly than film, they have a much lower resolution. Recording a hologram with a digital camera results in a loss of information contained in the fine detail. This results in the loss of resolution along the optical axis in the reconstructed image. In microscopic holographic PIV (μHPIV), magnified versions of holograms are recorded which circumvents the problems with digital recording of an unmagnified hologram. Digital μHPIV is discussed further in subsection 1.2.4.

1.2.2 Particle Velocimetry at the Micro-Scale

In 1998, Santiago *et al*. published the first paper on micro-scale particle image velocimetry (μPIV),[23] in which they studied the creeping (~10 μm s^{-1}) flow of water around an approximately 30 μm diameter cylindrical obstruction. Particle images were recorded using an interline-transfer charge coupled device (CCD) attached to a commercial epifluorescent microscope (figure 1.3a). The sample was continuously illuminated using a mercury arc lamp and exposures recorded with an inter-frame time of 68.5 ms. Velocity vectors were subsequently extracted using a super-resolution PIV algorithm,[24] yielding velocity maps with a lateral resolution of 3.45 μm over a 120 μm × 120 μm field of view (figure 1.3b). In this work, Santiago *et al*. highlight three key issues that complicate micro-scale particle velocimetry: the illumination of the sample, the scattering efficiency of the smaller particles necessary, and the effect of Brownian motion on measurements.

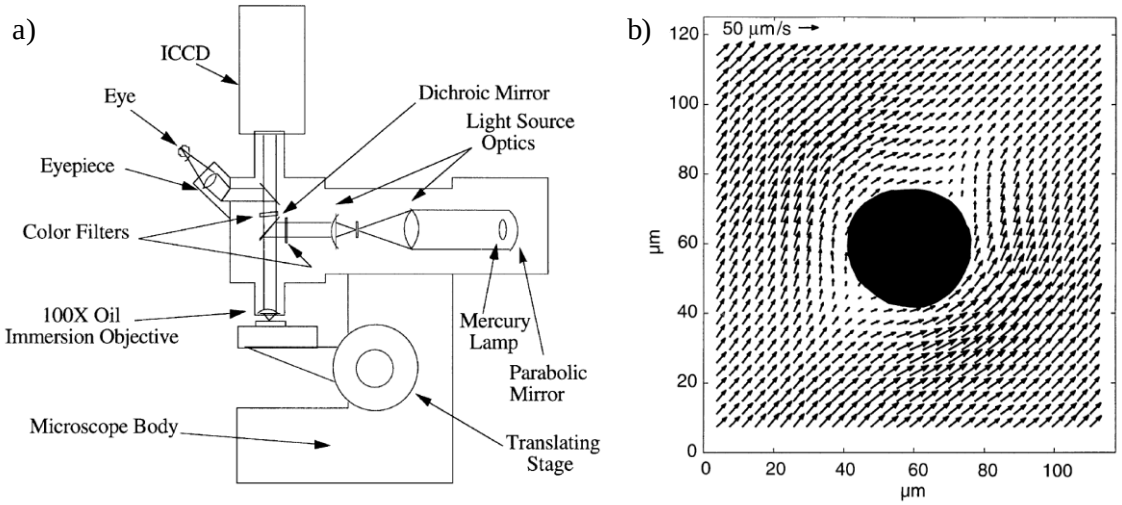

Figure 1.3 a) A schematic of the μPIV system used by Santiago *et al*. b) Eight-image ensemble averaged flow vector field around a cylindrical obstruction. Reproduced from reference [23].

For larger-scale PIV, a sheet of light selectively illuminates particles in a plane with a thickness which is small compared to the length scales of the flow. Particles are imaged with the thickness of the sheet defining the depth of the measurement. Given the difficulty associated with producing a light sheet of appropriate depth as well as introducing it into a microfluidic cell, Santiago *et al*. opted for a volume illumination approach. The consequence of volume illumination is that depth of focus is not strictly limited and any illuminated particles outside of the microscope focal plane will contribute to recorded images as an out of focus blur. If a gradient exists in the flow along the optical axis, the movement of out of focus particles will bias the result of a correlation. As out of focus particles reduce the signal to noise ratio, an upper limit is also imposed on seeding density, resulting in fewer particles per exposure than in an ideal macro-PIV experiment. In their work, Santiago *et al*. applied a threshold to their images to minimise the effect of out of focus particles on correlations.

In order to follow the flow faithfully, tracer particles are required to be much smaller in μPIV experiments – typically ranging from 200 nm to 1 μm.[25] Particles must not only follow the fluid flow in particle velocimetry techniques, they must also be visible in the recorded images. As such, fluorescent particles are imaged through a filter which blocks out the excitation light so that smaller, and therefore more weakly-scattering particles, are more distinct from the background.

Brownian motion, due to random thermal noise in the fluid, is another fundamental consideration in μPIV. Santiago *et al*. quantified this error relative to the ideal particle displacement as:[23]

$$\varepsilon_B = \frac{1}{u}\sqrt{\frac{2D}{\Delta t}}$$

where ε_B is the relative error due to Brownian motion in the position of a particle with diffusivity D travelling at a velocity u over the time interval Δt. D is given by Einstein[26] as

$$D = \frac{\kappa T}{3\pi\mu d_p}$$

where κ is Boltzmann's constant, T is the absolute temperature of the fluid, μ is the dynamic viscosity of the fluid and d_p is the particle diameter. The error in the particle position is inversely proportional to the fluid velocity and to the square root of the particle diameter. When dealing with small particles in a slowly flowing fluid, the relative positional error ε_B can become large. For example in their original μPIV paper, Santiago *et al*. quoted a relative error due to Brownian motion of approximately 9 % in a single pair of exposures.

As an alternative to increasing particle size, a longer interval between exposures (Δt) also has the capacity to reduce the relative positional error. Such a strategy is, however, only applicable in regions of flow with small velocity gradients so that it can be assumed that velocity is constant over the whole path of a particle during Δt. Santiago *et al.* took advantage of the unbiased nature of the diffusive effects and averaged velocity vectors obtained at the same interrogation region over many pairs of exposures. The diffusive uncertainty then becomes $\varepsilon_B/\sqrt{N}$, where N is the total number of particles averaged.[23] In this case they recorded 8 instantaneous images, yielding 40 independent samples at each interrogation region, showing that the theoretical uncertainty due to Brownian motion in the averaged vector could be reduced to approximately 1.4 %.

In 1999, Meinhart *et al*. published a modified experimental approach to μPIV.[27] This time, using an inverted epifluorescent microscope, volume illumination was provided by a pair of pulsed Nd:YAG lasers. Using a laser pulse duration of 5 ns, which is

effectively the exposure time, facilitated the study of much faster (~10 mm s^{-1}) flows. Images were recorded of flow in a 35 μm deep × 300 μm wide × 25 mm channel with 200 nm fluorescent polystyrene seeding particles. Using a correlation algorithm, a velocity map was obtained with a vector spacing of just 450 nm in the wall-normal direction. Results agreed to within 2 % of the analytical solution of flow in a rectangular channel.

Ensemble averaging was employed in this work to improve signal-to-noise ratio, however, rather than averaging the extracted velocity vectors from each image pair, the correlation peaks were averaged before the velocity was extracted. Averaging in this order helps to mitigate any bias from wildly erroneous vectors. Three possible strategies for ensemble averaging were later compared by Meinhart *et al*.[28] The first of these involves averaging the image data which results in effectively increasing the seeding density. This has a hard upper limit to the number of realisations that can be averaged as particles start to overlap. The second strategy is the averaging of extracted vectors but with this method there is a risk that a single erroneous vector can skew, particularly the angle of, the result. The final method involves averaging the correlations before a peak is fitted and a vector extracted. Using the same set of particle images for each method, Meinhart *et al*. found that averaging in correlation space yielded the highest quality velocity data.

In 1999, Koutsiaris *et al*. published a first attempt at estimating the velocity field in a 236 μm inner diameter (ID) glass capillary.[29] The capillary was imaged inside a bath of refractive index-matching liquid to prevent the introduction of an aberration due to imaging through such a tightly curved air/glass interface. The fluid inside the capillary, glycerol, was seeded with 10 μm glass spheres, an unusually large size compared to the scale of the capillary. Particles were illuminated with a continuous 20 W halogen lamp and images recorded using a CCD camera running at 331 frames per second. Using this system, velocity profiles inside the capillary were estimated with a resolution of 26.2 μm in the wall-normal direction. A figure for the relative displacement error of 1.78 % is reported, however it should be noted that the flow profile was distorted close to the capillary walls due to imperfect refractive index matching between the glass and the flowing suspension.

In 2000, Meinhart *et al*.[30] continued to address the problems associated with volume illumination. A theoretical expression for the depth of the two-dimensional measurement plane was derived in terms of the wavelength of illumination, the numerical aperture (NA) of the optical system and the diameter of the seeding particles, and found to agree well with experimental data. In a volume-illuminated system, seeding densities must be chosen judiciously in order to balance the signal-to-noise ratio to the resolution of the reconstructed velocity fields. They note that the signal-to-noise ratio may be improved by increasing the ratio of in-focus to out-of-focus particles, accomplished by; (1) decreasing the measurement depth i.e. increasing the NA, (2) decreasing the total depth of the test fluid and (3) decreasing the particle concentration.

In the same year, Olsen and Adrian made a significant advance in the understanding of the effects of out-of-focus particles.[31] Rather than being solely concerned with the visibility of out-of-focus particles in recorded images, their effects on the correlation function, and consequently the extracted vectors, were quantified. Equations which describe the cross-correlation function of a μPIV system were derived, and the concept of a theoretical depth-of-correlation was discussed. A cross-correlation of μPIV data is made up of the weighted sum of correlations from particles at different depths. By deciding a limit after which contributions are no-longer significant, bounds can be put on the depth of the section of fluid over which the velocity is averaged.

In a separate publication, Olsen and Adrian focused their attention on another problem specific to μPIV, the effects of Brownian motion on correlations.[32] Equations describing correlation functions were derived including Brownian motion for the case of a plane-illuminated and a volume-illuminated sample. They found that the effect of Brownian motion in a plane-illuminated experiment would be to broaden the correlation peak, a potentially useful effect as it may enable the simultaneous non-invasive measurement of velocity and temperature. In the case of a volume-illuminated experiment, Brownian movements along the optical axis cause particle images to change in size, leading to a bias in correlations. Brownian motion therefore has the effect of further increasing the depth of correlation in a μPIV experiment.

Realising that Brownian motion only introduces a significant error on particle displacements for slow (< 1 cm/s) flows, Meinhart and Zhang applied μPIV to a much more extreme flow environment.[33] They studied the flow inside a commercial inkjet

print head, where velocities were measured up to 8 $m\,s^{-1}$ and accelerations were found to reach up to 7×10^{5} $m\,s^{-2}$. The measurement plane, with a depth of 8 – 10 μm, was kept intentionally close to the wall to reduce noise from out-of-plane particle movements. Ensemble phase-averaged velocity maps were published at all stages of the ejection cycle with a vector spacing of 4 μm × 11 μm. Phase averaging refers to the averaging of several instantaneous velocity maps recorded at the same point during the recurring ejection cycle, a technique common in PIV measurements of periodic flows.

Nowadays, μPIV is a well-established technique for measuring flows in microfluidic systems. The technology has become sufficiently mature that turnkey systems are available from a number of companies,[34,35,36] opening the technique up to a wider community of researchers. However, in situations where all three components of the velocity are required, seeding cannot be controlled or optical access is not available through flat optical windows, μPIV in its basic form is not appropriate. The following section will discuss the various adaptations and enhancements to the original μPIV method.

1.2.3 Extensions to Traditional μPIV

The traditional μPIV of Santiago *et al.*[23] has become a standard technique in the characterisation of microfluidic flows.[37,38,39,40] Traditional μPIV, however, is only capable of measuring two components of velocity on a two-dimensional plane (2D2C). The behaviour of flows that have significant gradients along the optical axis or significant out-of-plane components of velocity is estimated poorly by a 2D2C technique. This section describes the important techniques used to extend the method beyond two components in two dimensions.

1.2.3.1 Confocal μPIV

Confocal microscopy, invented in the 1950s by Minsky,[41] essentially provides a point-wise measure of reflected intensity from a sample. The light emanating from the sample is focussed through, and spatially filtered by, a pinhole between the objective lens and detector. The pinhole aperture only allows light from a very small region around the focus of the objective lens to reach the detector. The ability of confocal microscopy to reduce the depth probed at a single measurement is particularly attractive in μPIV, where the background glow due to particles outside of the measurement plane is undesirable.

In 2004, Park *et al*. first used the existing technique of spinning disk confocal microscopy to examine micro-scale flows.[42] The microscope used, illustrated in figure 1.4, contains a pair of spinning disks; one with an array of micro lenses and the other with an array of matching pinholes. The spinning disk system removes the need to continually move the sample laterally relative to the imaging system. Each microlens-pinhole pair probes a different point on a single measurement plane; the light from each pair is directed onto a different part of the CCD. Multiple slices in the axial direction are obtained by moving the sample relative to the collection optics in this direction. Since a full measurement takes a relatively long time to complete, confocal μPIV is only applicable to steady flows.

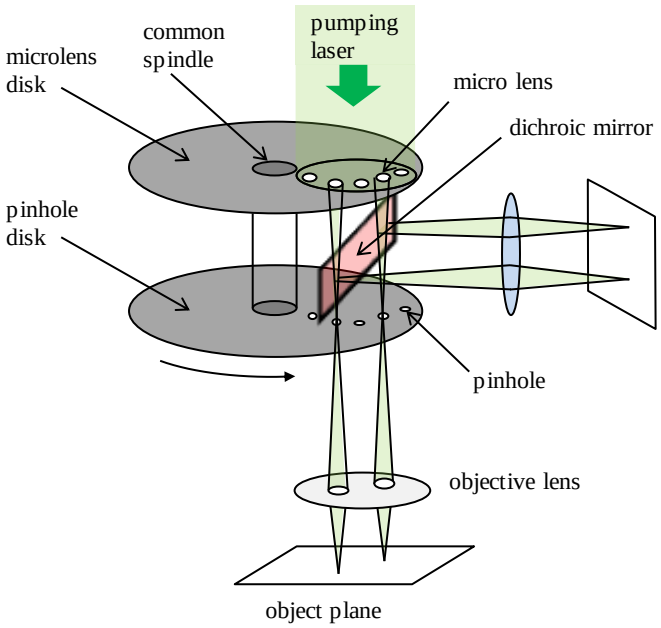

Figure 1.4 A schematic of the spinning-disk confocal microscope used by Park *et al*. Reproduced from reference [42].

Park *et al*. were able to measure velocities of fluids flowing inside glass tubes with inner diameters of 516 μm and 99 μm. The resulting measurements had a confocal depth of 2.8 μm and frames were recorded at 30 frames per second. Viewing particles inside a tightly curved cylindrical sample did, however, cause some problems. The sample was mounted between a pair of microscope cover glasses and secured with cyanoacrylate glue. The refractive index differences between all four media – crown glass cover slip ($n = 1.475$), glue (n~1.33), tube wall ($n = 1.544$) and flowing water ($n = 1.33$) – resulted in refraction at every interface, creating an uncertainty in particle positions and astigmatised particle images. This uncertainty was corrected for by estimating the optical path length at each point across the sample, effectively curving the measured planes.

The confocal measurements were compared to conventional epifluorescent microscopic measurements of the same flow system. The difference in visibility of particles between the two methods is shown in figure 1.5. Considering the flow profiles extracted using the two techniques, confocal μPIV appears to yield much more reliable results. Results obtained using conventional microscopy display a bias towards the mean velocity compared to the new confocal results (figure 1.6). This bias occurs because particles in

a greater depth of the sample contribute to the correlation function, that is, profiles taken of the axial mid-plane of the tube are biased by the slower particles closer to the walls in front of, and behind this plane. Similarly, profiles close to the front face of the tube are biased by the much faster particles in the centre of the tube. It has been noted by Park *et al*. that faster particles appear as streaks[42] because the laser continuously illuminates the sample, rather than being delivered in discrete pulses with nanosecond duration that can effectively freeze particles.

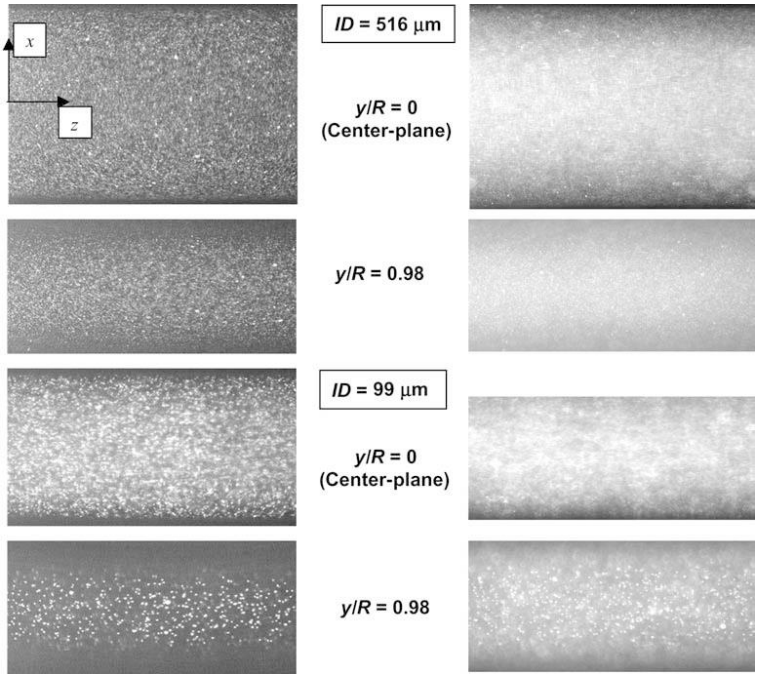

Figure 1.5 A comparison of particle images at two different planes along the optical axis by spinning disk confocal (*left*) and conventional (*right*) microscopy. Reproduced from reference [42]. *Note: the coordinate system used in this diagram is not the same as any coordinate system referred to in my text. The ratio y/R is the ratio of their y-coordinate to the internal radius of the capillary.*

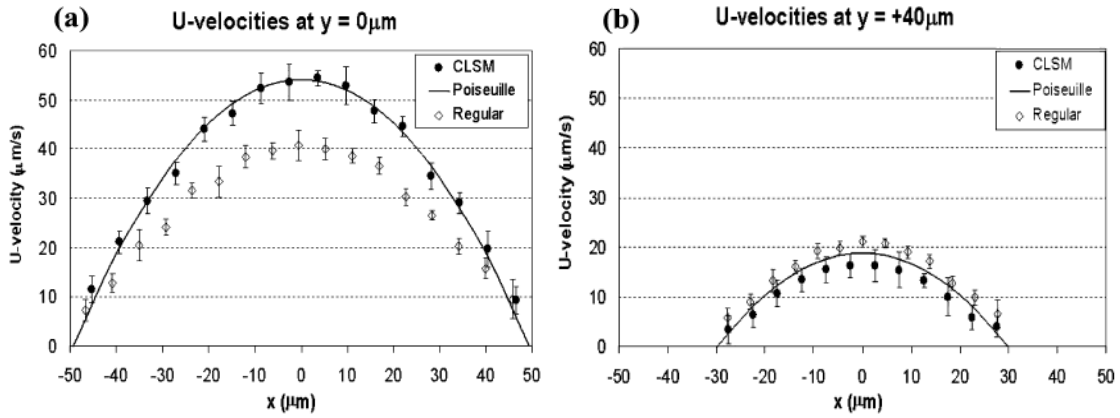

Figure 1.6 A comparison of velocity profiles measured by spinning disk confocal μPIV and conventional μPIV at two different depths within a 99 μm ID capillary. Reproduced from reference [42]. *The y-coordinate in these figures refers to the position along the optical axis relative to the central plane of the capillary, referred to in my text as the z-axis.*

In 2006, Kinoshita *et al*. incorporated a high speed confocal scanner, capable of recording a sequence of images at different axial planes at 2000 frames per second, into their system.[43] This setup was used to study the internal flows of a droplet travelling along a microchannel with a 100 μm × 58 μm cross-section and a confocal depth of 1.88 μm. The faster scanning rate of this microscope allowed Kinoshita *et al*. to record images with a finer resolution in the axial direction than previous workers. Using the increased number of planes of 2-component velocity data, they inferred the third component of velocity by making use of the continuity equation. The result was a full 3D 3-component measurement of the recirculating flow inside the moving droplet.

At the time of writing, the pioneering work on confocal μPIV by Park *et al*. has been cited 83 times within the literature. This particular confocal technique finds use within a wide range of areas,[39] including bio-microfluidics where, for example, Lima *et al*.[44,45,46,47] and more recently, Patrick *et al*.[48] have employed it in the studies of red blood cell movements. Three colour confocal μPIV has also been used to simultaneously record 2-component velocity and pH by Ichiyangi *et al*.[49]

1.2.3.2 Stereoscopic μPIV

In stereoscopic μPIV, images of particles are taken from two different angles in order to gain information about the third component of the particle motion. Stereoscopic μPIV is a 2-dimensional, 3-component method as velocities are measured on a single plane at a time. By the time stereoscopic μPIV was introduced, stereoscopic macroscopic PIV was already established as a standard technique.[50] The layout of a stereoscopic PIV system is illustrated in figure 1.7. The relative positions of both the cameras to the sample must be accurately known in order to create the appropriate transformation matrix to convert between image coordinates and real-world coordinates.[51] This is usually achieved by taking a picture of a calibration grid with both cameras. In each image, the apparent movements of a particle are combined to estimate the true 3-dimensional motion. Fundamentally, stereoscopic μPIV relies on the same principles. There are, however, new challenges to the technique at the micro-scale. Firstly, it is difficult to record two simultaneous images with a large angular separation, without sacrificing numerical aperture, and secondly, calibration is more difficult as it is generally unfeasible to place a calibration grid inside a microfluidic flow system.

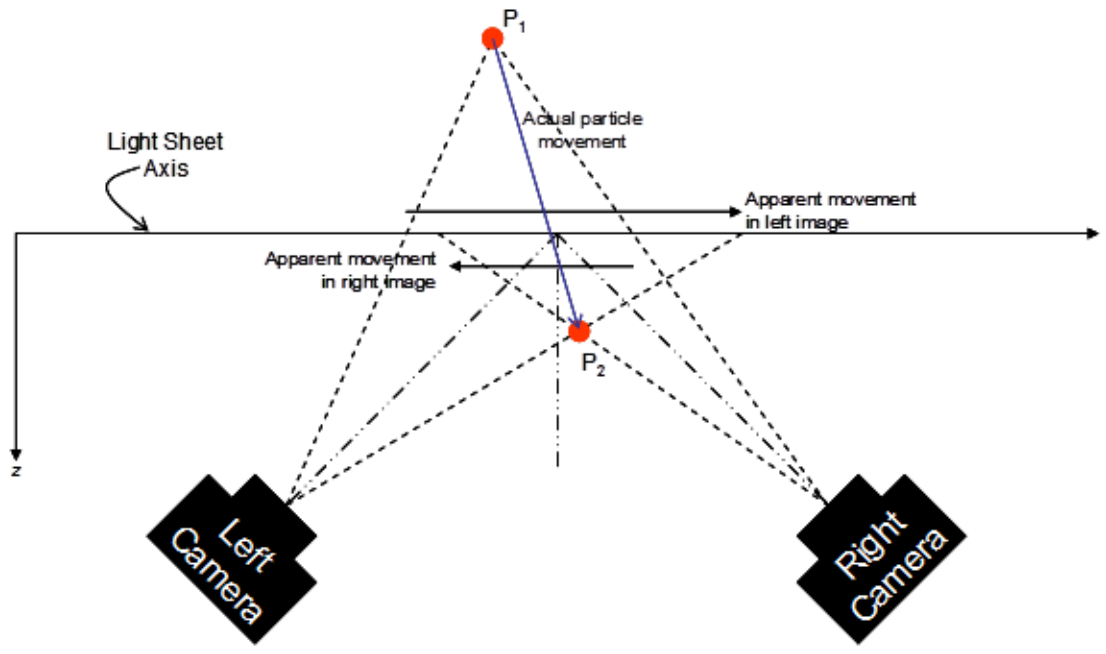

Figure 1.7 A general stereoscopic PIV setup.

Klank *et al*. published the first results from a stereoscopic μPIV system in 2002, with the study of flow inside part of a microfluidic cell sorter.[52] In this experiment, stereoscopic viewing was achieved using a single camera by moving the sample laterally relative to the objective lens between exposure pairs. Given that it is the velocity maps, rather than the images, that are transformed to give the third component of velocity, it is appropriate to use a single camera method to measure steady flows. Measurements were made at five planes with a 10 μm spacing and a field of view of 857 μm × 686 μm inside a microfluidic cell. Velocities showed good agreement with a CFD model, although there did not appear to have been any calibration.

Following on from the work of Klank *et al*., the majority of publications concerning stereoscopic μPIV experiments utilise commercial stereomicroscopes fitted with two digital cameras.[53-58] An illustration of a typical 'common main objective' stereomicroscope-based μPIV system is shown in figure 1.8. The view from each eyepiece comes from the sample at different angles, and gives the viewer a sense of depth. In a stereoscopic μPIV setup, two separate cameras are used to record the two views simultaneously. A stereomicroscope should not be confused with a compound microscope fitted with a binoviewer, where both eyepieces show exactly the same image. The binocular view of this latter microscope serves only to make its use more comfortable.

In macroscopic stereoscopic PIV, the focal planes of the cameras are tilted with respect to one another, meaning only a small area of the image is in focus for both cameras. Conversely, the use of a stereomicroscope in μPIV benefits from the focal planes of the views lying parallel, with an almost complete overlap.

The intrinsically low numerical aperture, and low magnification of stereomicroscope objectives, has been cited as both a disadvantage[53,54] and an advantage.[55,56,59] Although compared to a high-quality, high-magnification objective the depth of correlation is much larger, the low magnification gives a larger area of measurement and allows for less optically perfect windows on microfluidic cells.

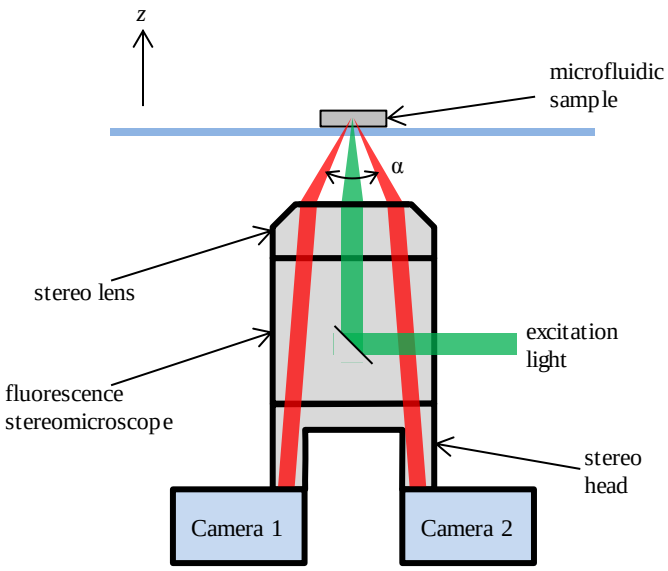

Figure 1.8 A general stereoscopic μPIV setup. Adapted from reference [54].

Lindken *et al*. were the first to develop a stereoscopic μPIV system based on a stereomicroscope.[53,54] In these experiments, measurements were carried out on a T-shaped micromixer and a self-calibration procedure[60] was used to refine the initial calibration (which was carried out in air) and minimise errors in alignment of the system. Calibration remains a complex procedure and must correct for the media between the imaged particle and the imaging optics. In the 200 µm deep channel, nine planes with a spacing of 22 µm were measured with a correlation depth of 15±5 µm. The error in the measured velocities in the axial direction was less than 7 %. The authors cite several potential sources of error in the measurements including the small viewing angle, a slight offset between the planes of the two views and problems with the self-calibration related to particles stuck to the cell walls.

Bown *et al*.[55] combined the basic stereoscopic μPIV method of Lindken *et al*. with the super-resolution method developed for macro-scale particle velocimetry in 1995 by Keane *et al*.[24] In super-resolution PIV, normal PIV analysis – i.e. cross-correlation of areas of image pairs containing multiple particles – is followed by particle tracking velocimetry (PTV), tracking individual particles to find their velocities. The results from the cross-correlations feed into the particle tracking algorithm, giving an indication of where to look for the particle in the second exposure. PTV analysis is usually restricted to very low seeding to minimise erroneous particle matches. Having an

estimate of the local velocity allows for much denser seeding as a small search radius can be defined for the second realisation of each particle. Bown *et al*. used the method to study flow over a backward-facing step in a microchannel. Particles were tracked in 3-dimensions and three components of velocity were recovered with a spatial resolution of $10 \times 10 \times 10$ μm, with each instantaneous measurement covering a volume of $900 \times 720 \times 45$ μm. Results were ensemble averaged over a sequence of 100 consecutive frames at a frame rate of 1 Hz. The authors claim that in order to match the axial resolution achieved with the super-resolution algorithm, a standard cross-correlation analysis with double the magnification would be required. In a subsequent paper, Bown *et al*. compare different methods of obtaining 3D3C velocity data.[56] One set of flow maps was obtained using stereoscopic μPIV. The other set was obtained by recording traditional μPIV data at a number of planes within the sample and using the continuity equation combined with the no-penetration boundary condition to infer the third component of velocity. Although the stereoscopic μPIV data agreed well with the model, the continuity-based data had a smaller experimental uncertainty with a better spatial resolution. The authors note, however, that the continuity-based approach is limited by the quality of data obtained at planes near the cell walls, where experimental errors are the often greatest.

In its simplest realisation, stereoscopic μPIV is capable of producing three-component velocity maps averaged on to a single measurement plane. Full 3-dimensional velocity measurement was achieved by Bown *et al*.[55] by a super-resolution technique, but the limited depth of field means that for many applications, the full flow volume would not be probed in a single measurement.

1.2.3.3 Defocussed methods in μPIV

While a number of research groups developed experimental and image-processing strategies to reduce the influence of out-of-focus particles, in order to produce clean, reliable 2D flow measurements in a single plane, others attempted to interrogate the light scattered from out-of-focus particles to gain 3-dimensional information. Two separate techniques make use of the light scattered from all particles within the depth of

the sample; these are defocussed μPIV and holographic μPIV. This section will contain a discussion on defocussed μPIV techniques.

There are two main approaches to defocussed μPIV, one can either analyse the shape and size of the diffraction pattern of out of focus particles to infer their axial position,[61,63-66] or apply a mask in the optical system so that a unique pattern is formed depending on a particles axial position.[68-74]

In 2000, Ovryn developed a method to obtain the depth of particles based on their out-of-focus images.[61] Particles were subjected to Köhler illumination and forward-scattered light was recorded on a CCD camera. The 3-dimensional velocity estimations were produced in a three step procedure; first, images of out of focus particles were obtained, then centroids were fitted to the diffraction pattern of each particle, and finally the transverse displacements of particles were measured. The diffraction patterns of the particles were compared to intensity patterns predicted by Mie theory[62] which allowed the depth of particles in each exposure to be estimated. The particles used were relatively large at 7 μm, however, the method does not impose any restriction on size or type of particles. The intensity patterns observed depend on a number of factors and reasonably good initial estimates are required so that the model correlates to the particles observed. The author warns against using laser illumination in this experiment as the speckle noise introduced by a coherent light source introduces an amount of noise in images. Short, intense pulses of light are hard to achieve without a laser source and as such, this method is limited to comparatively slow-moving flows.

In 2003, Speidel *et al*.[63] interrogated the diffraction patterns of out-of-focus particles imaged with an epifluorescent microscope to obtain depth information, a method known commonly as deconvolution microscopy. They measured the ring-like structures around out of focus particles and were able to track single fluorescent nanoparticles in 3-dimensions with sub-nanometer precision. The 3D distribution of intensity collected by a microscope from a single small bright source is its point spread function (PSF), the ring-like pattern observed around an out of focus particle is a slice through the PSF. Speidel *et al*. reason that the distance of the particle from the focal plane of the microscope is precisely encoded in these rings. Since the exact properties of a microscope are generally not accessible to a high degree of accuracy, they determined the PSF of their microscope experimentally. Latex beads with a diameter of around

216 nm were immobilised in a porous polymer network and imaged through a 100×, NA 1.3 oil-immersion objective for different positions along the optical axis. Results could only be obtained from a minimum distance of 500 nm from the focal plane, closer than that and there are no observable rings, and up to a maximum distance of 3.5 μm from the focal plane. Even at the largest measured distance of 3.5 μm, changes in particle position could be measured to a tolerance of 4 nm. The relatively small volume probed (40 μm × 60 μm × 3 μm) and the single-particle nature of this technique limits its applicability.

A similar deconvolution approach to Speidel *et al*. was adopted by Wu *et al*.[64] in 2005; they used the ring pattern around spherically abberated images of fluorescent particles to estimate distance from the focal plane. Wu *et al*. studied the movements of multiple bacteria tagged with a fluorescent marker within a measurement volume of 418 μm × 335 μm × 75 μm with a resolution of ~0.48 μm in the *z* direction. In 2006, Park and Kihm[65] developed a new algorithm capable of identifying particle centres and outermost fringe radii and tracking them in 3D. Fringe radii were compared to a theoretical PSF to estimate depth. They tested their method on flow around a spherical obstruction, seeded with 500 nm fluorescent micro-spheres such that the average inter-particular distance was around 19 μm. Flow vectors were obtained in a measurement region of 165 μm × 93 μm × 25 μm. The volumetric measurement resolution was 5.16 μm^3 with a velocity measurement uncertainty of ±5.4 % after ensemble averaging of 60 imaging frames. Peterson *et al*.[66] also conducted experiments on a similar system, looking at flow in a 50 μm deep rectangular microchannel. Flow vectors were found to agree to within 5 % of the theoretical flow, however, vectors were only obtained for around 70 % of the channel depth and seeding was very low, averaging 2.25 particles per image.

The factor that limits the probed depth in deconvolution-μPIV is the signal-to-noise ratio in the diffraction pattern of an out-of-focus particle. As a particle moves away from the focal plane the defocussed image gets larger, spreading the intensity over more pixels and eventually coming to a point where it cannot be reliably resolved from the background. The overlap of multiple out-of-focus particles is also a factor; the larger the ring structures are, the less dense seeding must be to avoid overlap which can be problematic for the image-processing algorithms. Given that a good initial model for the

point spread function must be known, or calibration experiments carried out, this method is not be appropriate for imaging particles inside a micro jet. A dynamically curving interface means that the PSF for particles changes not only with depth, but also with lateral position.

A different defocussed method, digital defocusing particle image velocimetry (DDPIV) has also been employed at the microscale to produce track particles in three-dimensions. DDPIV was introduced by Willert and Gharib[67] in 1992, and combined defocus with an aperture mask in the imaging system so that particles produce unique patterns depending on their distance from the focal plane. The basic arrangement is illustrated in figure 1.9; an aperture mask is placed close to the plane of the lens so that a scattering source away from the reference (focal) plane of the system is imaged as multiple spots. The distance between the spots *b* is a function of the distance from the focal plane. Using two pinholes as, sketched, loses information about which side of the reference plane the particle is on. Most experiments involve a mask with three pinholes arranged at the vertices of an equilateral triangle as the pattern observed with a triangular mask inverts as a particle passes from one side of the reference plane to the other. Pereira *et al*. used this method to measure a stream of sub-millimeter bubbles passing through a propeller in a ~300 mm^3 measurement volume, with an absolute error in velocity of 0.025 pixels.[68]

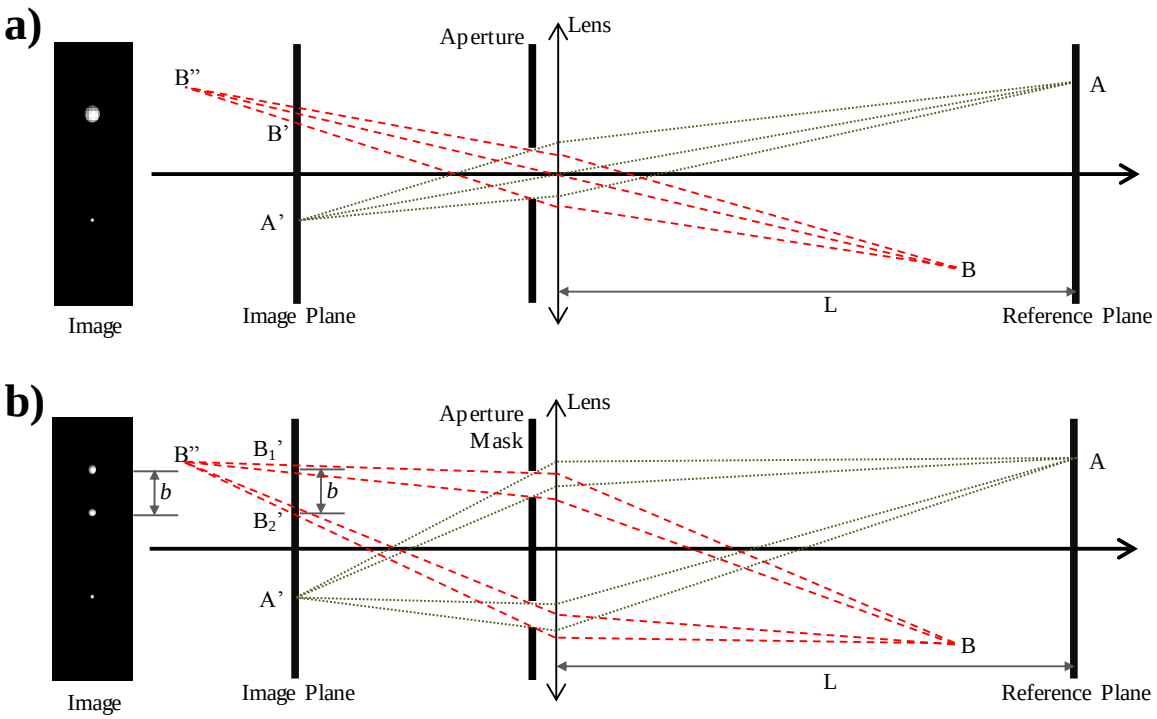

Figure 1.9 The defocusing principle. a) A normal imaging system; b) a defocussing arrangement. Adapted from reference [68].

In 2006, Yoon and Kim successfully applied the DDPIV method to flows on the micron-scale.[69] They modified a commercial inverted epifluorescence microscope by positioning a miniaturised pinhole mask behind the back exit pupil of the objective lens. They decided that the geometric optical analysis of the optical system was not appropriate for a pinhole mask inserted in a microscope for a number of reasons. Firstly, the assumption made by for macro-scale DDPIV that the pinhole mask is in the same plane as the lens[70] is not appropriate given that modern microscope objectives are made up of many optical elements and the mask is therefore a significant distance away from the lens vertex. The high magnification of a microscopic system also magnifies alignment errors so that assumptions based on pinholes being equidistant from the optical axis are no-longer appropriate. The calibration procedure involved imaging particles stuck to a microscope slide which was translated between exposures. An example particle image at different positions in *z* is shown in figure 1.10. A calibration curve was then drawn, giving the z position of particles versus the diameter of the circle defined by the triplet of spots. This system was used to measure flow over a backwards step in a microchannel; the measurement volume was 768 μm × 388 μm × 50 μm.

Images were recorded at 1000 frames per second, with fewer than 100 particles per image. The spatial resolution in the resulting velocity maps was 5 μm × 5 μm × 1 μm, with an RMS error in *z* displacement around three times that in the *x* and *y* directions. The measurement depth in these experiments was limited by the very low light intensities collected due to the small pinholes.

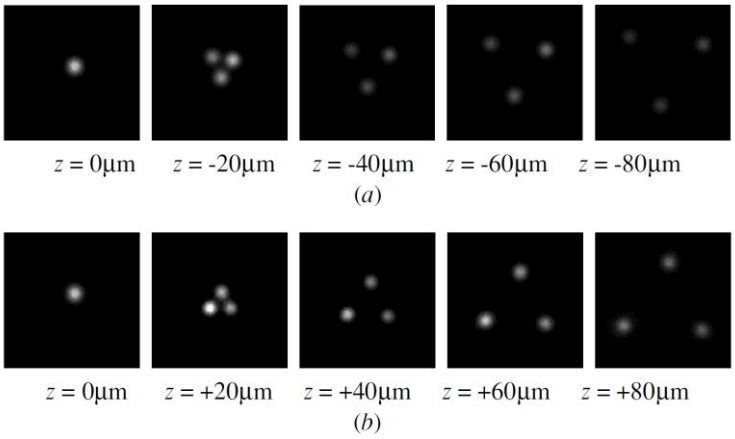

Figure 1.10 Images of a particle using three pinholes according to the distance from the reference plane ($z = 0$). Reproduced from reference [69].

In 2007, Pereira *et al*. used a digital defocussing μPIV (DDμPIV) system to measure the recirculating flows driven by evaporation within a 2 μl droplet of 5 % ethanol in water.[71] The droplet was imaged from below, to remove any complication from refraction at the curved air-solution interface, using a modified epi-fluorescent microscope. The mask used was an equilateral triangular arrangement of three 2 mm diameter pinholes, 7 mm away from each other. Calibration was performed by translating a flat glass substrate with 2 μm fluorescent particles stuck to it. Unlike Yoon and Kim, a more involved uncertainty analysis was carried out by Pereira *et al*. They found that the uncertainty in the *x*- and *y*-directions was around 0.5 μm compared to 1.0 – 1.5 μm in *z*, and that the maximum *z* displacement that could be measured was around 110 μm. Images of particles moving inside an evaporating drop were recorded at 250 frames per second, and the measurement volume was 300 μm × 250 μm × 150 μm. Images were processed and 3-dimensional particle tracks were produced.

The DDμPIV technique was successfully applied in the field of bioengineering by Lu *et al*. in 2008. They were interested in developing a tool to study embryonic blood flow[72] and used a system similar to Pereira *et al*. to study the cardiovascular blood flow and the motions of the heart walls of an embryonic zebra fish. The heart was approximately 80 μm in diameter and 100 μm long, the depth of measurement was around 40 μm.

Particle detection algorithms have to be able to locate the triplet of images due to each particle, however, the overlap of multiple triplets sets a limit on the maximum seeding density in DDμPIV. This problem was addressed separately by Tien *et al*.[73] and Lin *et al*.[74] Tien *et al*. combined a colour filter with the pinhole mask. Each of the three pinholes had its own colour (red, green or blue) and images were recorded with a three colour CCD camera. The result is not only a unique colour for each of a particle's three images, but also a unique colour for overlapping images. One potential limitation with this technique is that a white light source must be used, rather than a pulsed monochromatic laser source capable of delivering much higher power densities. Alternatively, Lin *et al*. introduced a differently shaped mask to solve the problem of overlapping particles.[74] The aperture was a clear annulus in an otherwise opaque mask. The annular aperture gives a ring for each particle with a radius dependant on the distance of a particle from the reference plane, see figure 1.11a. The interlocking rings due to overlapping particles are much easier to resolve than the pattern of dots with the triangular aperture; the rings were detected using the circular Hough transform (CHT), figure 1.11b. In this work results were shown for a ~410 μm × 310 μm × 120 μm measurement volume with a 180 nm uncertainty in the *z*-position of particles. This method allows for much higher seeding densities at the expense of losing the information on which side of the reference plane particles are on; ambiguity is avoided by ensuring that the reference plane is outside of the sample.

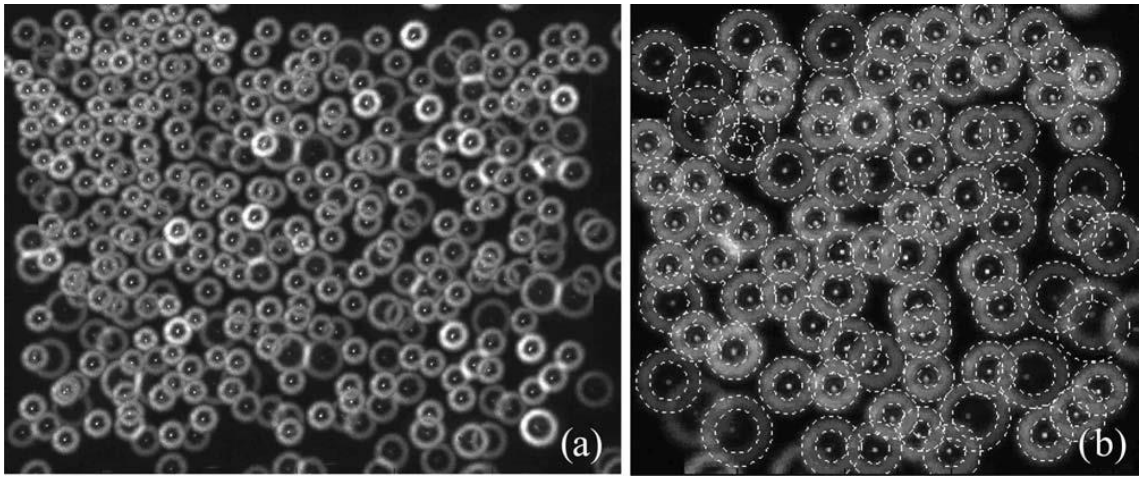

Figure 1.11 a) Image of multiple fluorescently doped microparticles from recorded with a microscope using an annular aperture. b) Identification of annular images by the CHT where each edge is indicated by a broken circle. Reproduced from reference [74].

1.2.4 Holographic μPIV

As mentioned previously, holograms are a means of producing three-dimensional images from a single two-dimensional recording. Holography is a two-step process, involving the recording of a hologram and subsequent reconstruction to give an image. Holographic recording is achieved by allowing the light scattered from an object to interfere with another, mutually coherent, 'reference' wave. The result is an interference pattern, modulated by the phase difference between the two waves. In this way, a full representation of the scattered light – i.e. both its amplitude and relative phase – is encoded on the hologram. The well-known Huygens' principle asserts that if the amplitude and phase of a wave is known on a single plane, then it is known for all space.[75]

If a hologram is recorded on film, the set of fine fringes due to the interference between the object and reference waves can act as a diffraction grating. If the reference wave is passed back through the film, it is diffracted to form a three-dimensional image of the recorded object. Holograms can be also recorded on digital cameras and reconstructed numerically using equations that model the diffraction of light. The underlying concepts important to holography as well as a description of the holographic method are presented in more detail in Chapter 2.

Holographic PIV (HPIV) is the application of the holographic recording method to record the motions of particles within a flow. HPIV is a three-dimensional (3D), three-component (3C) method of velocimetry and since holography is an intrinsically 3D imaging process it is distinct from the other 3D velocimetry techniques.

There are two basic recording geometries used in HPIV, differing in how the reference beam is delivered to the detector. The simplest arrangement, in-line holography, involves illumination of a highly-transmissive sample from behind while recorded from in front. The parts of the illuminating wave that do not get scattered by the sample form the reference wave, which interferes with the parts that do. In-line HPIV systems are simple to set up but are only appropriate for recording samples with low seeding density to ensure that a sufficient amount of unperturbed reference wave arrives at the detector. Since the zero order wave diffracted from the hologram overlaps with the image of the sample during reconstruction, reconstructions of in-line holograms are intrinsically noisy.

In the off-axis geometry a separate reference wave is used that does not pass through the sample and strikes the detector at an angle. The bulk modulation of the interference pattern results in the spatial separation of the diffracted orders so, at the expense of added complexity of the optical system, the noise inherent in in-line holograms is dispensed with.

Early holographic PIV systems used either in-line or off-axis recording geometries and photographic plates as the recording media.[86] Although by the early 2000s such HPIV systems were successful and robust,[76-80] few groups attempted to replicate them as it was a rather cumbersome process.[81] Photographic plates take time and expertise to develop making it slow to review the data collected, whether in alignment of the optical system or in assessing if the flow phenomena of interest were captured at all. Novel photosensitive substrates were developed with the aim of removing the darkroom work, these included photoreactive crystals,[82] thermosensitive plates[83,84] and bacteriorhodopsin.[85] Even with potentially more user-friendly recording media, the optical reconstruction requires precise alignment of the hologram in the reconstructing beam and may take hours to interrogate a single real 3D image of a particle field.[79]

Currently, most groups record their particle field holograms on digital imagers such as charge coupled devices (CCDs) or on complementary metal oxide semiconductor (CMOS) detectors. Although digital recording devices have resolutions at least an order of magnitude lower than holographic film, the technology is improving rapidly and the future of HPIV is generally seen as fully digital.

1.2.4.1 Limitations of Holographic Recording

Holograms can produce a 3D image of the light scattered from a sample, but there are some limitations to how well point-scattering bodies can be resolved spatially – the depth-of-focus (DOF) problem. There also exist limitations to the amount of information that can be stored on a single hologram – a speckle noise problem. Not only do the effects of increased DOF and speckle noise affect the quality of individual exposures of a particle field, they also impact the strategies of measuring particle displacement between different exposures.

The resolution of a holographic reconstruction, like any other optically-formed image, has a limited depth of focus. The axial and transverse resolutions are limited by the angular range of the interference pattern of light emanating from a single point reliably collected and recorded in the hologram. The spread of a point in the transverse direction (x_t) and axial direction (x_a) are related to the half-angular aperture of recording. For a diffraction limited imaging system:[62,86]

$$x_t \approx \frac{\lambda}{\Omega}\,, \tag{1.1}$$

$$x_a \approx \frac{\lambda}{\Omega^2} \tag{1.2}$$

where, λ is the wavelength of the illumination and Ω is the half-angular aperture of the collected light. The half-angular aperture is the sine of the half-angle of the cone of collected light. The axial resolution is much lower than the transverse resolution when $\Omega < 1$ leading to elongated, cigar-shaped reconstructions of particles.

The limiting factor in the angular range collected may be the size of the hologram, the pixel size of the detector or the angular range of light scattered from a particle itself. In film-based holography, where the light-sensitive emulsions used have a very fine grain size, the angular aperture and consequently the spatial resolution of the reconstruction is related to the size of the hologram and the recording distance. Digital recording devices have pixel pitches in the range of 100 – 200 mm^{-1}, compared to around 5000 mm^{-1} on a holographic film.[81] Fine fringes, due to light scattering from the sample at higher angles, are not recorded on a low-resolution detector. For example, a CCD camera with a pixel spacing (Δ) of 7.4 μm is incapable of recording fringes with a spatial period less than 14.8 μm resulting in finer fringes being blurred out. A digital hologram illuminated by a typical PIV laser with $\lambda = 532$ nm will therefore record only the amplitude and phase of incident light that has a maximum angular aperture of less than 0.04, corresponding to a half-angular range of 2.1°. Using equation (1.1) and (1.2), in digital reconstructions, light from a single point scatterer is smeared over an ellipsoid with a diameter of 25λ transversely and a length of 625λ along the optical axis. It is possible to mitigate this problem by recording holograms from multiple angles[78,79,87] and defining the particle position as the volume where the ellipsoids from two or more reconstructions overlap – the resolution in all three dimensions tends to the axial resolution. Alternatively, digital holographic microscopy (DHM) can be used where the fringes are magnified onto the detector by an optical system, effectively decreasing the pixel size by the magnification of the system.[94,102,112]

The angular aperture of collected light can also be limited by the Mie scattering of light by a particle. If the forward-scattered light is collected, the image is dominated by a narrow central lobe of diffracted light with an angular aperture of $\Omega = \lambda/d_p$.[81] The depth of focus of a 5 μm particle in forward-scatter hologram reconstruction is around 47 μm. The angular aperture of light scattered at 180° to the direction of illumination is greater, but the best case is the light scattered at 90° where there is no dominant scattering lobe.[86] The drawback with recording back- or side- scattered light is that much less light is collected from each particle compared to forward-scatter.

Holograms are formed by the interference of coherent light – usually provided by a laser. The pattern recorded by a hologram not only encodes the interference of individual particles with the reference beam, but also the interference of light scattered

by particles with each other and the interference of both the light from particles and the reference beam with any other scattering sources in the optical train. These extraneous interferences give rise to the effect known as speckle noise which is a non-uniform and quickly varying background. Speckle noise can be reduced by ensuring as few unwanted scattering sources as possible in the optical system and by post-processing of holograms; either by ensemble averaging or tens of exposures, or by a pixel-by-pixel median subtraction over a few exposures.[88,89] Although post-processing methods can go some way to removing the speckle due to imperfections in the recording system, the interferences between particles in the illuminated volume are inevitable and set an upper limit on the product of the seeding density and the depth illuminated. Speckle noise was examined by Meng *et al*. in 1993[90] for in-line holographic PIV, where the problem is compounded by additional speckle due to the mutual interference of different reconstructed orders, and by Pu and Meng in 2004[91] for off-axis holographic PIV. Speckle noise was shown to have statistically very similar properties in 3D to particle reconstructions; for this reason it is not possible to filter out speckle noise without destroying particle images. Meng *et al*. conclude that the only solution is to increase the signal-to-noise ratio (SNR) by ensuring that the intensities of reconstructed particles are greater than the mean intensity of the speckle noise. The SNR can be increased by using the largest possible angular aperture, to concentrate reconstructed particle light over the smallest volume, and by reducing the number of contributing particles by reducing the illuminated depth or the seeding density.[81]

1.2.4.2 Digital Holographic Microscopy in HPIV

The concept of holographic particle image velocimetry has been successfully combined with the methods of digital holographic microscopy by several groups interested in developing a three-component, three-dimensional velocity measurement tool. The microscopic imaging procedures effectively magnify interference fringes so that holograms may be recorded with a larger effective angular aperture, going some way to improving the particle depth of focus in a digital system. Speckle noise is potentially less of a problem in holographic microscopy as the depth scale of samples is typically

small (sub-millimeter) and therefore fewer particles contribute to the speckle background.

Although the pixel sizes of modern digital recording devices still impose an upper limit on the spatial resolution, digital recording does have several distinct advantages. Data can be reviewed in near-real time, which aids with alignment, and it is easier to record a time-series of images using a digital device, although low resolution cinematic holography on film has been attempted in the past.[92] Digital recording and reconstruction also offers access to the complex amplitude of the reconstructed light, allowing particles to be located more accurately to around two particle diameters,[93] and particle displacements to be calculated more accurately than possible with intensity information alone.

A digital holographic microscope (DHM) achieves the necessary magnification by either lensed or lensless method. In a lensless DHM, the sample is illuminated by a spherically expanding wave which projects a magnified version of the sample onto the detector. Typically these are in-line holograms; the parts of the illumination beam that are unperturbed by the sample form the reference beam that interferes with the forward-scattered light from the sample. A lensless digital holographic microscope was developed by Kreuzer and co-workers in 2001.[94-97] The remarkably simple system has been used for 3D imaging of a wide range of samples and particle tracking in fluids. A submersible version of the microscope has also been constructed for the purpose of studying microscopic marine wildlife in its natural environment.[98] Their lensless digital holographic microscope consists of a laser for illumination, a pinhole to act as the point source and a 1.5 Megapixel CCD camera for recording[94] and is based on the same principle as the point-source electron holographic microscope used by Fink *et al*.[99] The microscope is sketched in figure 1.12.

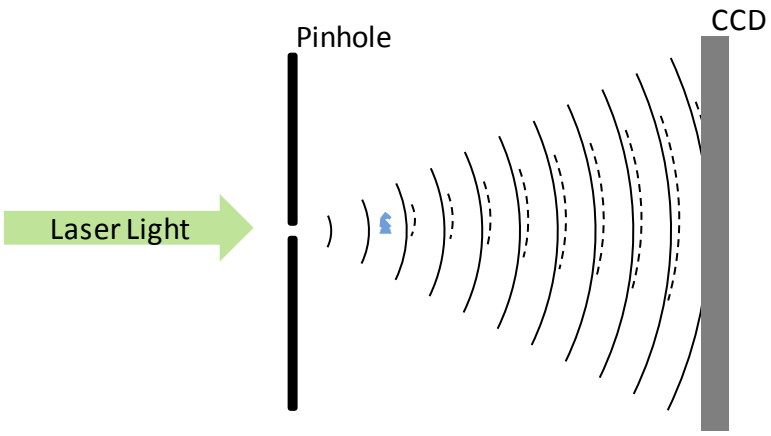

Figure 1.12 A point-source digital holographic microscope.

The sample is placed a distance $d_{lensless}$ from the pinhole and light is scattered on to the CCD placed a distance $D_{lensless}$ away from the sample. An image is formed with a magnification of $D_{lensless}/d_{lensless}$. Trajectories of swimming algae were recorded by Xu *et al*. as a proof of principle for a device that could be used for particle velocimetry.[96] The flow volume, of about 1 mm^3 was reconstructed numerically in 3D as a stack of individual planes of the reconstructed field, at different distances from the point source. The intensity of the planes is equivalent to a series of dark-field microscopic images taken with the focal plane at different depths within the measurement volume (figure 1.13). From the stack of images they were able measure the density of algae as 96 /mm^3 and estimate a mean swimming speed of ~150 μm/s; there was no description of the tracking algorithm used or value for the depth of focus given. The authors also present images from a larger, 1 cm^3, volume of measurement, a larger number of algae are visible but the resolution is lower as it decreases with increasing pinhole-to-sample distance.

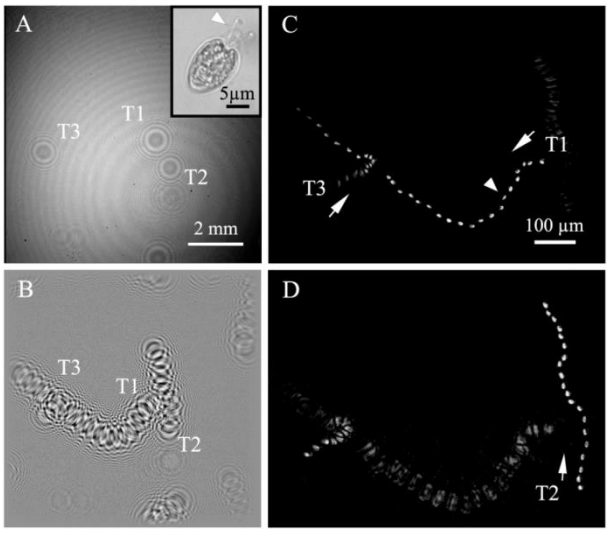

Figure 1.13 Holograms and reconstructions of algae by Xu *et al*. a) A single hologram containing three algae (T1-T3); inset, a bright-field image of a single alga. b) The sum of 10 filtered holograms. c) Reconstruction of the summed hologram in so that alga T1 is in focus. d) Reconstruction of the summed hologram at a plane 500 μm above the plane in c. Reproduced from reference [96].

Garcia-Sucerquia *et al*. presented measurements of flow around a spherical obstruction in a micro-channel using the point-source holographic microscope.[97] Speeds of 5 μm tracer beads of up to 350 μm/s were measured. They quote an error on the coordinates of tracer particles to be ±50 nm in favourable conditions; presumably this is the error in the (x, y) coordinate for a given reconstructed plane.

Four years after Kreuzer and co-workers first presented their work using the lensless point-source holographic microscope, other groups began to experiment with lensed systems. Lensed systems are similar to ordinary bright-field microscopes with coherent illumination. The earliest examples were in-line systems[100-111], without a separate reference beam, sketched in figure 1.14a. Off-axis systems, have also been developed[112-115]; the beam is split into two parts, one part illuminates the sample and scattered light is focussed by an objective lens onto a detector while the other part is directed through a matched objective and onto the digital detector at a small angle to normal (figure 1.14b).

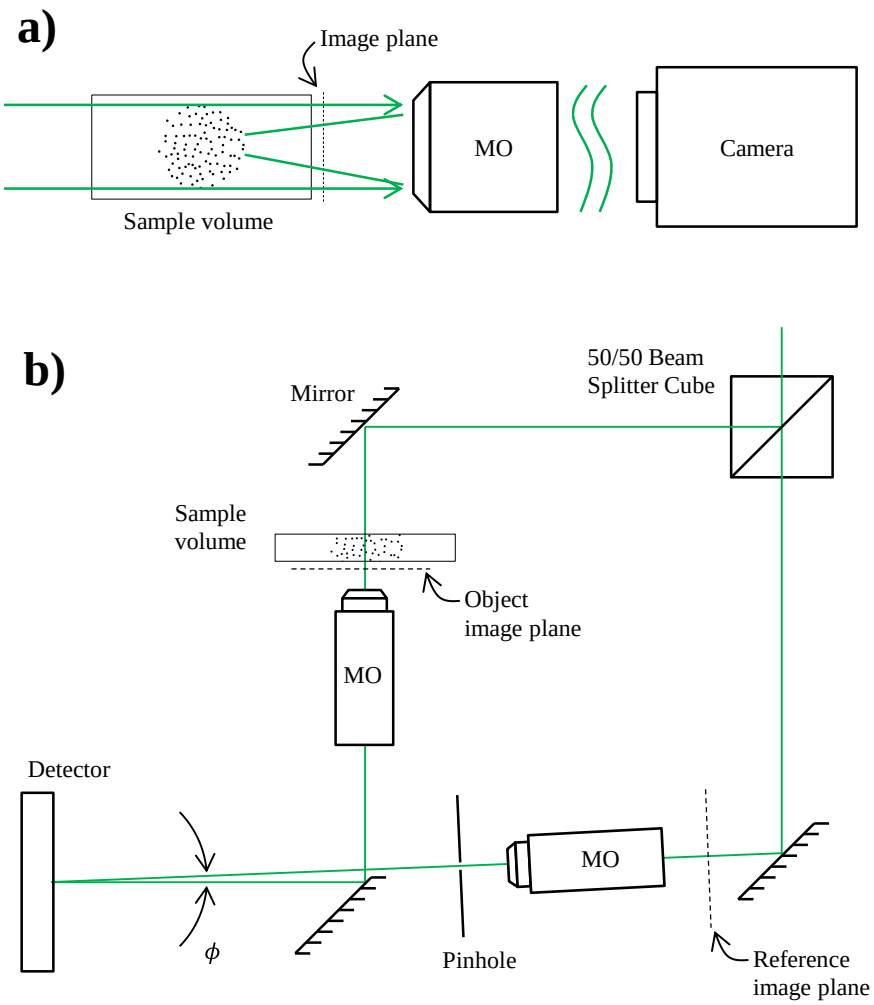

Figure 1.14 Lensed holographic microscopes. a) An in-line lensed holographic microscope. Adapted from reference [116]. b) A possible off-axis holographic microscope arrangement. Adapted from reference [113].

In their pioneering work on in-line lens-based holographic flow tracking in 2005, Satake *et al*. measured the 3D motions of 1 μm tracer particles in a microchannel with a width of 100 μm and a depth of 40 μm.[100] 130 velocity vectors could be obtained simultaneously with a time-resolution of 100 μs, using a system that consisted only of a laser, a mirror to direct it on to the sample, an objective lens and a 1 Megapixel CCD camera. Data processing took 26 hours for a series of 2000 frames, on a fast computer for the time (four AMD Opteron 850; 2.4 GHz processors). Flow profiles in both the transverse and axial directions appeared to be in good agreement to the theoretical velocity profile, although no uncertainty in velocity or in particle position was quoted.

In 2006, Satake *et al*. used the same holographic microscope to study flow in a cylindrical micro-pipe.[101] The micro-pipe had a diameter of 92 μm, so this time the depth of measurement was increased to more than double that in the previous work. In this publication, an attempt is made to analyse the uncertainty in estimating a particle's depth by imaging a test target, a glass plate with 1 μm spherical particles attached to its upper (towards the objective) side. The test target was moved along the z-axis (the optical axis) using a piezo actuator with a resolution of 10 nm. The accuracy in the measurement of the test case remains inconclusive. The error in locating one of an ensemble of particles on a flat plane fails to help estimate the error in locating a seeding particle in a microchannel other than providing a minimum value. Inside the microchannel, particles are distributed throughout a volume and the intensity distribution at the position of any single particle will be affected by the out-of-focus patterns from many other particles at different depths. Again, axial and transverse flow profiles were plotted along with the theoretical profiles. The uncertainty in flow velocity was around 2 % for the transverse profile and 12.5 % for the axial profile.

In 2006, Sheng *et al*. used a digital in-line holographic microscope to measure distributions of micrometer-size (3 μm) and submicrometer (0.75 μm) particles in flows with depths of 1 to 10 mm.[102] As well as presenting some particle tracking work, they present a detailed study of how the depth-of-focus of a particle changes for different measurement volumes, magnifications and particle sizes. For the very worst case of 3 μm particles imaged with 10× magnification and a total imaged depth of 10 mm, the mean depth-of-focus is 19.2 μm. It should be noted that worst-case DOF is an an order of magnitude better than the DOF possible in unmagnified in-line holography, while the total depth of the measured volume is two orders of magnitude higher than possible with an equivalent standard transmission microscope – allowing 5769 particles to be imaged simultaneously. The lowest particle DOFs were obtained with 40× magnification and were ~4 μm for a 3 μm particle and 2.5 μm for a 0.75 μm particle. In two subsequent papers, Sheng *et al*. used their technique combined with cinematic recording to image and track particles. Particle trajectories were measured in two very different flow environments: the prey-induced swimming behaviour of dinoflagellates[103] and near wall velocity and shear stress in a turbulent boundary layer[104]. In these papers, a guided trial and error approach was used in the particle tracking. First, thousands of holograms were recorded and reconstructed to give the 3D

intensity distribution at each measurement time, a resolution of 2 μm in *z* was found to give the best results. Subsequently, particles were located and a large number of possible tracks were computed by nearest-neighbour detection, assuming that the distance moved by a particle between exposures is less than the inter-particle distance. Once all possible tracks had been computed, they were filtered on criteria such as smoothness of trajectory, upper bounds for velocity and acceleration and the similarity of the size and shape of matched particles.

In 2007, Kim and Lee published their first results of flow in a micro-tube, with a similar in-line digital holographic microscope.[105] They used a 60× high-NA (NA = 1.1) water-immersion type objective to image flow inside a pipe with a 100 μm bore. The tube was made of fluorinated ethylene propylene (FEP), which has an index of refraction (1.338) close to that of water, using water as both the immersion medium and the flowing fluid inside. The index matching reduces problems with refraction at the inner and outer surfaces of the tube. Flows were measured with seeding densities of 0.25, 0.5 and 1 % by volume, corresponding to 160, 310 and 580 reconstructed particles per image; all three conditions yielded flow profiles in very good agreement to the theoretical prediction. The maximum RMS error for the case of 0.25 % seeding was 1.48 %. In these experiments, using a very high numerical aperture increased the accuracy to which particles could be located.

More recently, technique of lensed in-line digital holographic microscopy has been applied to measuring the velocity of suspended particles in fluids in a wide range of areas. Novel applications in the physical sciences include inertial migration in microtubes[106-108] and the motions of colloidal particles[109] and in biological sciences uses include the study of red blood cells[110] and frictional drag on the surface of filamentous algae.[111]

Lensed holographic microscopy has also been implemented using an off-axis configuration, sketched in figure 1.14b. In the off-axis configuration, a separate reference beam that does not pass through the sample provides the interference on the detector. Unlike an in-line lensed system, the off-axis lensed holographic microscope is not restricted solely to transmission configuration. The sample can be illuminated and imaged from any optically accessible direction. Off-axis holograms do not suffer from the noise intrinsic with in-line holograms. In their system, Coupland and co-workers

interfere a magnified image of the object field with an image of a plane reference wave, formed through a carefully aligned and matched objective lens.[112-114] The reconstruction procedure and geometry of holograms recorded in this way is no more complicated than reconstruction of an in-line microscopic hologram. Arranging the microscope in this way means that the complicated reconstruction geometry and paraxial approximations, used for example in the recent work by Abrantes *et al*.,[115] are unnecessary. There are several benefits of using a separate reference beam: the quality of the reference beam is not dependant on the quality of the optical access to the sample or on the seeding density of the sample, and the relative intensity of the reference beam can be adjusted to get the optimal object-reference intensity ratio to get the best contrast in holograms.

1.2.5 Summary

Particle-based velocimetry techniques are powerful tools we can use to measure flows on the micro-scale. Traditional μPIV relies on conventional microscopy and image processing methods to extract two-component velocities on a single plane of a microfluidic system. Stereoscopic μPIV is done by essentially taking two traditional μPIV measurements from different viewing angles to estimate the third component of velocity on a single plane. The confocal μPIV technique offers the highest spatial resolution, but its temporal resolution is limited as each flow field must be scanned progressively. The defocussed methods allow many particles to be located in three dimensions in a single measurement, albeit over a small depth (tens of microns). Holographic μPIV is capable of capturing 3D images of particles within a much greater (hundreds of microns) depth than other microscopic techniques. Holography uniquely gives access to the amplitude and phase of the reconstructed light inside the sample; this is particularly easy to access in digital holography.

Micron-sized inkjets have tightly, and dynamically, curved interfaces. Images – conventional or holographic – of particles inside an inkjet cannot be used directly to perform particle velocimetry methods. The following section will review the methods that have been used to correct for the optical distortion due to a curved air-medium interface in the literature.

1.3 Optical Distortion Compensation

Optical distortions are due to changes in refractive index between an imaged sample and the surrounding medium – usually air. A change in refractive index across a curved interface leads to a lensing effect. In particle velocimetry, the lensing effect results in aberrated and astigmatised images of particles and uncertainties in their positions. Optical distortions are ideally avoided altogether, rather than corrected for. Wherever possible, one tries to image through a flat interface, I have already discussed examples where droplets have been imaged through a flat transparent substrate or capillaries measured in roughly index-matched surroundings.[42,71] Although it is possible to surround a capillary or pipe in a fluid that matches the refractive index of its walls, there still exist refractions at the curved interface between the test fluid and the pipe wall – without changing the test fluid itself, these refractions are unavoidable. De Witt *et al*. were able to calculate the shape of, and machine, optical forms that compensate for refractions to allow faithful images of seeding particles inside pipes to be recorded.[117] In the case of a micro-scale ink-jet flowing in the surrounding air, index matching is not possible and no optical form can be placed in the recording system to account for the rapidly-changing, dynamic air-ink interface. We must therefore attempt to compensate for the distortion only after the images have been recorded.

In the literature, two methods exist which allow the restoration of images distorted by a curved optical interface; these are either based on ray-tracing[118-132] or by novel holographic reconstruction.[133-138] Figure 1.15a shows a uniform grid distorted by a hemispherical lens, the ray-tracing method effectively pulls parts of the image back towards the centre, achieving partial recovery of the information inside (figure 1.15b). The use of holography provides a unique means to replay the wave scattered by the sample. Replaying this wave back through a replica of the sample wall – either optically[133-137] or numerically[138] – compensates for all aberrations and distortions exactly. This section will review both the ray-tracing- and holographic-based methods of optical distortion compensation.

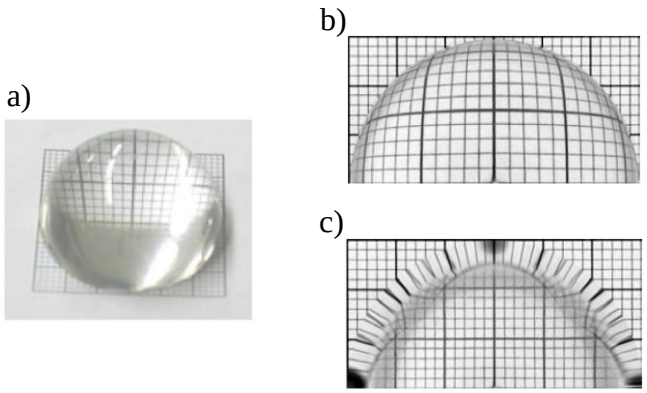

Figure 1.15 A hemispherical lens and its image distortion. (a) Hemispherical Plexiglas lens; (b) original image; (c) restored image. Reproduced from reference [118].

1.3.1 Ray-Tracing Methods

In 2004, Kang *et al*. published a method to restore the images of particles inside evaporating liquid droplets.[118] The droplets were illuminated by a sheet of light along their central plane and imaged at 90° to the light sheet, figure 1.16. Illumination by a light sheet allows only particles in a single plane to be imaged – greatly simplifying the mathematics of the mapping functions. The mapping function traces a single 'representative ray' back from the image plane of the camera, through the droplet's surface using Snell's law of refraction;

$$n_1 \sin \varphi_1 = n_2 \sin \varphi_2 \qquad (1.3)$$

where, n denotes refractive index and φ the angle the ray forms with the normal to the surface; the subscripts 1 and 2 denote the first (incident) and second (transmitted) media respectively. The authors are justified in their use of geometric optics in this case as the wavelength of the recorded light is much smaller than the dimensions of the sample.

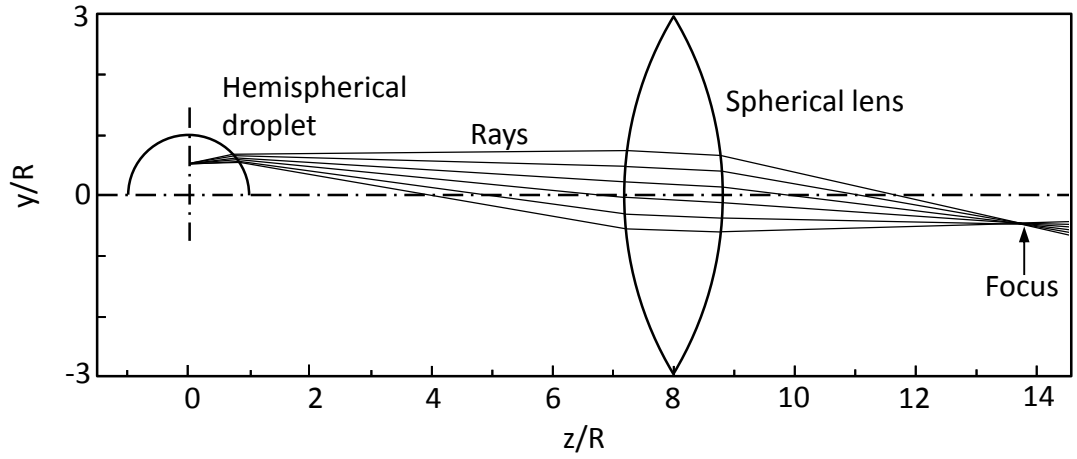

Figure 1.16 Ray tracing of light rays emanating from a point inside a hemispherical droplet. The broken vertical line depicts the plane of the light sheet. The axes are scaled by ***R***, the radius of the droplet. Reproduced from reference [118].

The geometry used in the mapping functions is shown in figure 1.17. A single representative ray, travelling normal to the image plane, emanating from P_i is traced back to the point P_s on the droplet surface. At the droplet surface, refraction is modelled by Snell's law and the direction of the refracted ray is modified relative to the surface normal **N**. The new ray is described by **B** and intersects with the object plane (the central plane of the drop) at the point P_0.

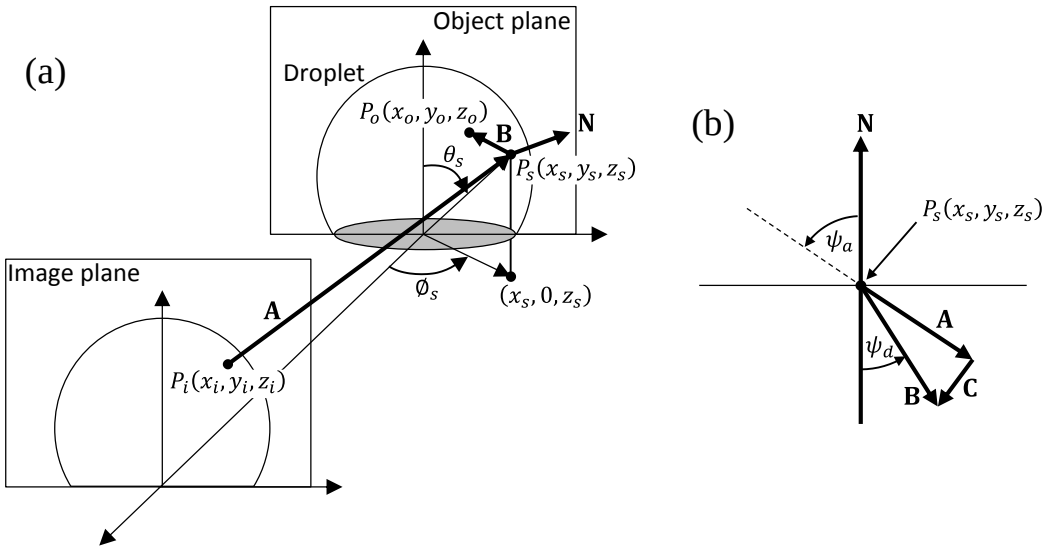

Figure 1.17 Coordinate system and vector relationship at the surface of the droplet. Reproduced from reference [118].

By assuming a simple mathematical form of the droplet surface, an algebraic expression for the relationship between P_i and P_o was derived. The authors reasoned that the shape of the drop can be described by the parametric function $F(r, \theta)$, defined as:

$$F(r, \theta) = r - \vartheta(\theta) = 0. \tag{1.4}$$

The shape function $\vartheta(\theta)$ is represented by a sum of the cosine series:

$$\vartheta(\theta) = R + \sum_{k=1}^{N} b_k \cos k\theta \cong R + b \cos \theta. \tag{1.5}$$

The shape of a droplet is usually well-represented by $\vartheta(\theta) = R + b \cos \theta$, ignoring all higher order terms for simplicity. The constants R and b are found from the digitised image of the drop using a least-squares method.

Kang *et al*. validate their mapping method by restoring an image of graph paper underneath a hemispherical Plexiglas ($n = 1.55$) lens, figure 1.15. The image is well restored in the central 75 % of its area – outside this area, the reconstructed image is badly corrupted. The uncorrupted area increases as the refractive index of the droplet medium decreases and, for particle images inside a droplet of a water/ethanol mixture, 80 % of the area inside was usable for PIV measurements (figure 1.18).

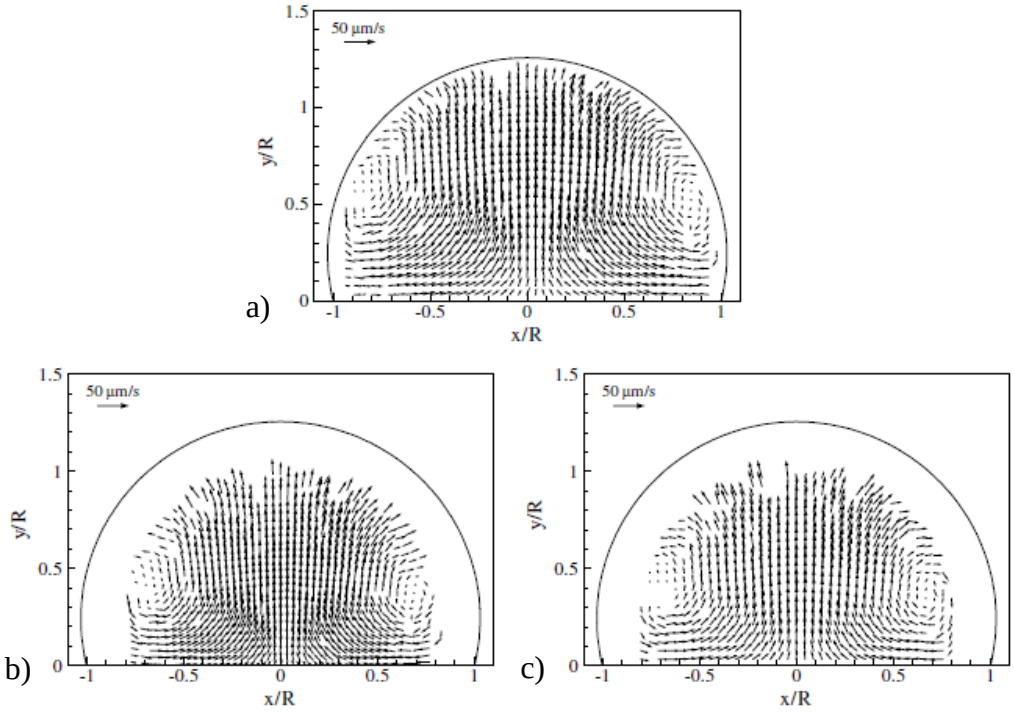

Figure 1.18 Instantaneous velocity fields inside a droplet containing 5 % ethanol in water. (a) results obtained with no correction; (b) results obtained with the mapping applied to velocity field; (c) results obtained with mapping applied to the image. The axes are scaled by the radius of the droplet, **R**. Reproduced from reference [118].

There are two ways of using the mapping method of Kang *et al*., either it can be applied to the raw images to correct them prior to the PIV analysis, or it can be applied after PIV analysis of raw images to correct the velocity fields (figure 1.18). The authors deemed data to be of a higher quality if the mapping is performed on the velocity fields, likely due to inaccuracies in the interpolation of the set of reconstructed points (P_0) onto a regular grid for correlations.

Minor *et al*. published corrections to the mapping function in 2007, having found that the original equations yield grossly unphysical results for droplets with a contact angle greater than 90° (figure 1.19).[119] A convincing derivation of the corrected equations, using the same geometry as Kang *et al*., is given along with some simulations, however no examples of restorations of real images are shown for validation.

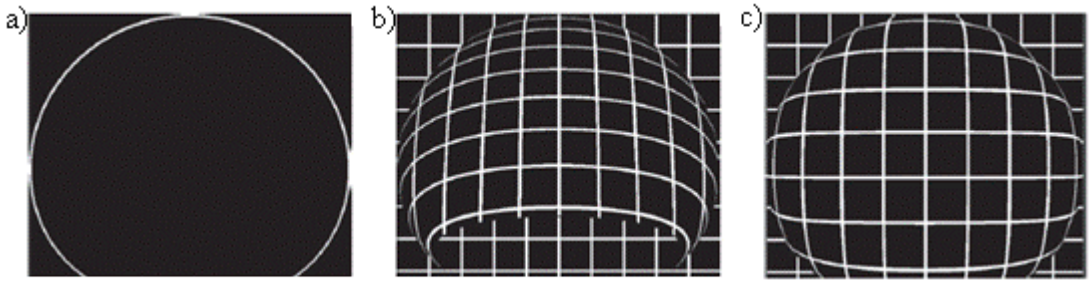

Figure 1.19 Droplet profile with a contact angle greater than 90° and distortion of a regular grid. The total size of each image is 575 × 697 pixels. (a) Droplet profile; (b) the result of distortion using the method of Kang *et al*.[118]; (c) result of distortion using the corrected method of Minor *et al*.[119] Reproduced from reference [119].

The ray-tracing method of Kang *et al*. and Minor *et al*. has been used by several groups interested in flows driven inside millimetre-sized droplets by evaporation[120-123] and electrohydrodynamic[124-126] effects. The limitations of the method are: the droplet shape must be adequately approximated by equation (1.4) or reconstructions are inaccurate,[122] as the droplet flattens images are dominated by reflections[127], and no information can be obtained close to the drop surface.[118] The highest gradients in velocity are often close to the surface in evaporating droplets – and the loss of this information is a great shortfall in the method.

In 2013, He and Duan addressed the issue of the loss of information near the drop surface.[128] They reasoned that not all of the rays emanating from a plane inside a drop can be captured by a camera perpendicular to the plane. They found that tilting the camera by a small angle (15 – 20°) from the normal to the light sheet, allowed them to recover 95 % of the total light-sheet area and measure the velocities of particles up to the droplet surface. The arrangement is sketched in figure 1.20. Two cameras are used in this technique; one records a shadowgraph image of the droplet, whilst the other records the particle images.

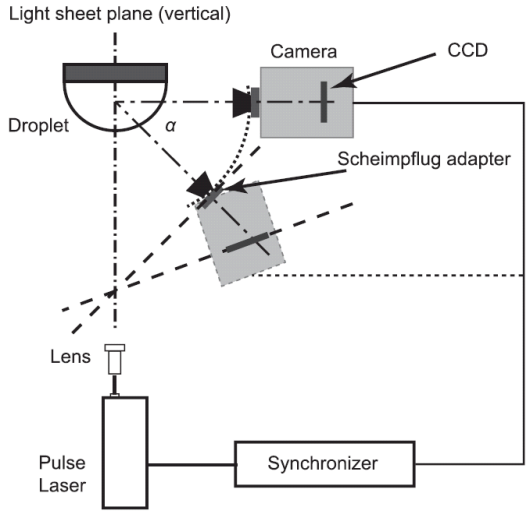

Figure 1.20 Schematics of the PIV system used by He *et al*. The image formation relies on the Scheimpflug principle. For the Schiempflug principle, the extended lines of the image plane (light sheet plane), the lens plane and the CCD plane must intersect. Reproduced from reference [128].

Unlike the previous work of Kang *et al*., the recovery method is numerical rather than algebraic. An outline of the droplet is fitted to the image from camera 1 using the Canny edge detector and the Young-Laplace equation. The droplet surface is obtained by rotating the outline profile about its symmetry axis, and the surface is meshed with triangles for the ray-tracing software to process. The images were restored prior to PIV analysis. This method appears to work well, as long as the triangular mesh is fine enough and several assumptions are fulfilled. The assumption unique to this experiment is that there is no perspective distortion in the recorded images. Perspective distortion is caused by differing magnifications in the axial and transverse directions, and the implication is that images must be recorded with a 1:1 imaging system. Without magnification, this technique, although promising for millimetric droplets, cannot be applied to micron-sized samples.

As well as droplets, a ray-tracing approach has also been applied to the study of other systems with curved boundaries such as the wakes behind Taylor bubbles in a (16 mm diameter) transparent pipe[129], the flow measurement inside a four-valve combustion engine cylinder (~100 mm diameter)[130] and, more relevant to this project, in a scale model of a continuous ink-jet[131] and a thinning polymer filament[132]. Work on the scale model of a continuous ink-jet, was published in 2012 by Castrejón-Pita *et al*.[131] The model ink-jet is 2.2 mm in diameter and flows were recorded in the range of 0.8 –

2.0 m/s. Much like in the droplet experiments of Kang *et al*., particles were illuminated with a light sheet (200 μm waist) and recorded normal to the light sheet. The mapping, based on ray tracing and Snell's law, was carried out on the velocity maps rather than the image data. The authors concluded that the extracted velocity data were accurate to around 15 %.

In 2012, Gier and Wagner investigated flows inside thinning polymer films with diameters ranging from 150 – 30 μm (figure 1.21).[132] They used a linear mapping method to correct the images which were strongly distorted due to the highly curved samples, validated by comparison to the distortion of graph paper by a cylindrical lens. The sample was volume-illuminated by either a pulsed Nd:YLF (527 nm) or a continuous wave Nd:YAG (532 nm) laser. Images of fluorescent particles were recorded with 20× magnification by a transmission microscope, with a 2.4 μm depth of focus. Velocity data were obtained by cross-correlation when the filament had a large diameter and many particles were visible and by particle tracking as the diameter shrank towards 30 μm. The results are shown in figure 1.22. There are two concerns with the measurements. Firstly, the measurement plane was assumed to be flat and aligned with the central plane of the axisymmetric polymer thread, in reality the measurement plane will be curved due to the refractions (foreshortening effect) at the cylindrical interface. Secondly, velocities are measured right up to the edge of the filament which is unrealistic for two reasons (1) the lensing effect of the rear (toward the illumination) surface of the filament means there areas at the sides of the filament in which particles are not directly illuminated (the effect is visible in figure 1.21); and (2) the problems with restoring images close to the edge of the sample, documented by previous users of the ray-tracing technique, appear to have been ignored.

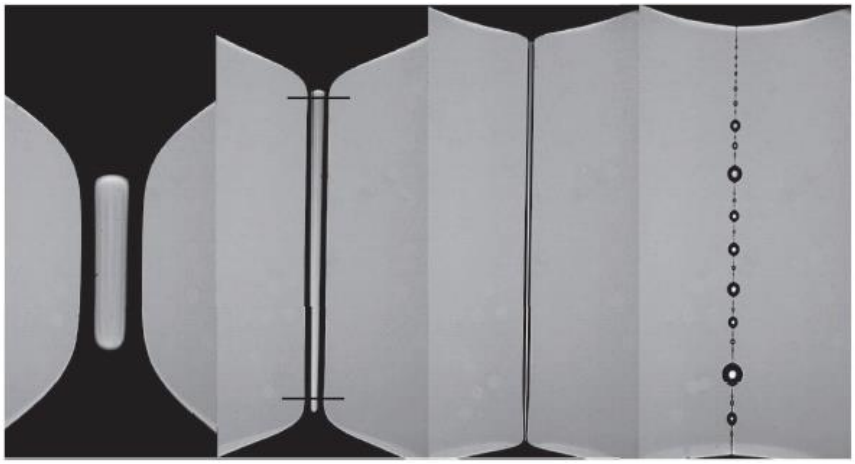

Figure 1.21 A microscope image of a thinning polymer filament at different times. Reproduced from reference [132].

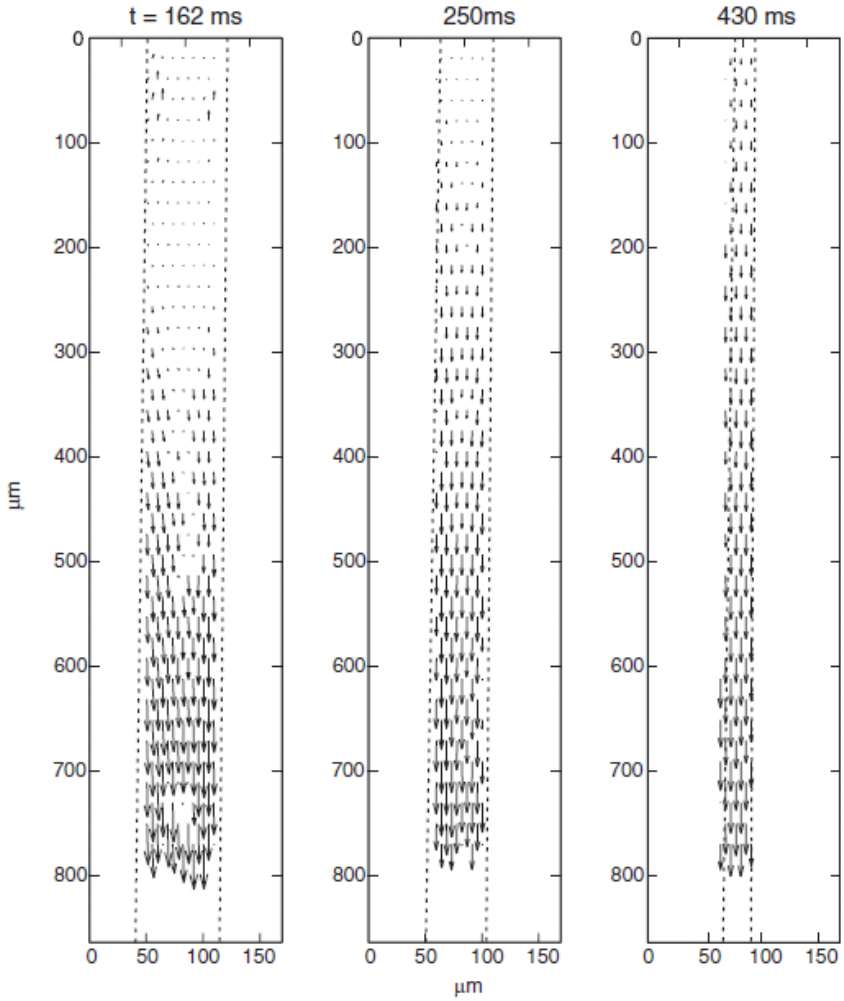

Figure 1.22 Velocity maps at three different moments during the capillary breakup of a polymer filament. Reproduced from reference [132].

The ray-tracing technique has been used by a number of different groups to successfully compensate for the optical distortion due to curved interfaces. Most of the work using the ray-tracing method has focussed on large, millimetre-scale, samples and appears to work well within certain constraints. It has also been applied to micron-scale cylindrically-curved samples by Gier and Wagner.[132]

1.3.2 Holographic Methods

We have already seen that holograms are a means to encode 3D information about a wave scattered by an object on a 2D detector; achieved by interfering the scattered light with a mutually coherent reference wave. In Chapter 2, I describe hologram recording and subsequent reconstruction. It is sufficient for the time being to appreciate that the object wave can be recovered from a developed holographic film by illuminating it with a reconstruction wave. If the reconstruction wave is the complex conjugate of the reference wave, a time-reversed version of the wave scattered from the object is formed – so that it scatters back from the film to form a real image of the sample. Aberrations due to refractive index changes in the recording system may then be compensated for by replacing optical elements present at the time of recording in the reconstructed real image wave.

As early as 1978, Heflinger *et al*. used a compensation cell to remove abberations introduced by refractive index changes between the sample and recording device.[133] Holograms of swimming plankton were recorded using a lens-assisted, off-axis system (figure 1.23a). Off-axis holograms use a small angular separation between the object and reference waves to ensure that, in subsequent reconstructions, the directly transmitted reconstructing beam does not swamp the reconstructed image. The wave arriving at the detector was recreated by illuminating the developed hologram with a replica of the complex conjugate of the reference beam. In their case of a plane reference wave, the conjugate is formed simply by reversing the direction of the reference beam (figure 1.23b). During recording, the light scattered from the plankton had travelled through a thickness of water (varying depending on the location of the

plankton), the aquarium wall, and was focussed onto the holographic film by a lens system. In order to reconstruct faithful images of the plankton, free from aberration, the lens system and a replica of the aquarium was replaced in the reconstructed field (figure 1.23b). Because of the time-reversible nature of light, replaying the hologram back through the same set of optical boundaries and media compensates fully for all refractions on the way to the detector. The replica of the aquarium was collapsible and allowed the reconstructed real 3D images of the plankton to be observed with an ordinary light microscope which could scan through the imaged volume.

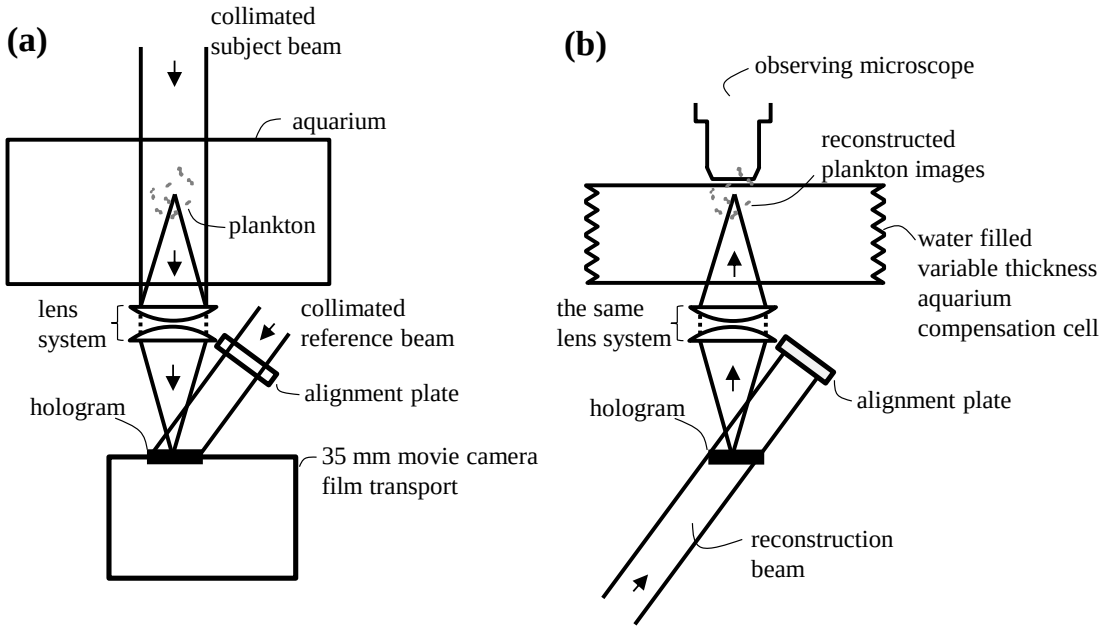

Figure 1.23 The hologram recording (a) and reconstruction system (b) used by Heflinger *et al*. Reproduced from reference [133].

The impressive early work of Heflinger *et al*. paved the way for the object conjugate reconstruction method to be used in HPIV. Notably, the approach has been used to account for imperfections in the collection optics of holographic imaging systems employed in HPIV experiments.[134,135] The ability to account for the aberrations in collection optics allows larger lenses to be used without the need to resort to prohibitively expensive large diffraction-limited optics. The technique has also been used to enable faithful particle images to be obtained from scattering particles inside thick, curved walls for example inside glass engine cylinders.[136,137] Finally, and most appropriate to the work described in this thesis, Wormald and Coupland apply the

method in a numerical environment to account for refraction at the curved air-water interface of a micro-scale droplet.[138]

Wormald and Coupland used a lens-based transmission digital holographic microscope, described previously in subsection 1.2.4.2 and sketched in figure 1.14, to record images of a 92 μm diameter ink-jet droplet ejected from a drop-on-demand print head with an exit velocity of around 5 m/s. The water droplet was seeded with 3.7 μm poly(methyl methacrylate) (PMMA) spheres, and images were recorded in transmission. Without any compensation for the refraction at the front (toward the camera) surface, particles were visible but their images were severely aberrated. Their method, explained in more detail in section 4.4, essentially uses the field recorded on the detector to deduce the field on the sample surface at the wavelength in air. The field on the sample surface is then propagated inside the sample at the appropriate wavelength for the sample medium. This of course requires some a priori knowledge of the object, namely its refractive index and the location of its surface. The surface is found by first refocusing the hologram numerically until the edges of the sample appear in focus, figure 1.24. From the refocused image of the sample, its edges and axis of symmetry can be detected. Assuming that droplets are axisymmetric, the surface is then known in 3D. Once the position of the surface has been estimated, the field on it is estimated using the Fresnel-Kirchoff diffraction formula (described in Chapter 2) (figure 1.24b). The complex value of the field on the surface is then interpolated to give a set of sources which are finely-spaced compared to the wavelength in the sample. Making the assumption that the field inside the sample is dominated by the scattering from these sources, it is estimated by propagating them at the wavelength of the light inside the medium. The method accounts for the refraction at the front surface but does not account for any internal reflections. The authors validate the method by using another piece of a priori knowledge, that is, the known shapes of images of scattering spherical micro-particles. Figure 1.25 shows reconstructed particles inside the sample at three different planes. The authors note that although particles images appear to be symmetric, at the front and middle plane of the sample, towards the back they appear astigmatised. This is attributed to the fact that the axis of the jet is not entirely parallel to the image plane of the microscope, i.e. the greatest errors in the reconstructed field arise from errors defining the sample surface. The authors suggest that the initial estimate of the sample surface could be optimised by propagating the light all the way

through the sample and comparing the wave behind the sample to the known form of the illuminating wave.

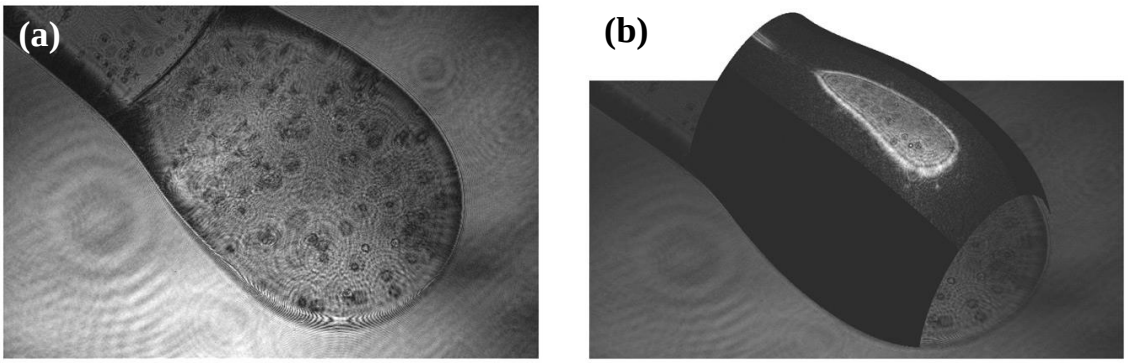

Figure 1.24 The amplitude of the reconstructed wave: (a) at the central plane of an ink-jet droplet; (b) on the front surface of the droplet. Reproduced from reference [138].

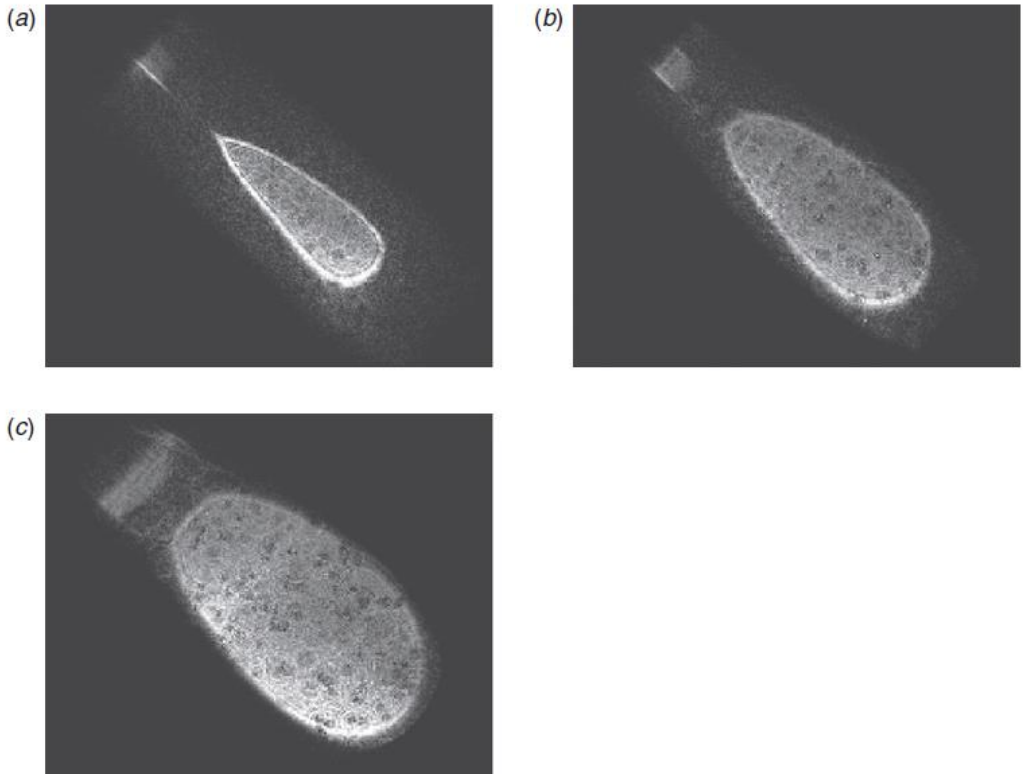

Figure 1.25 Reconstructed particles inside an inkjet droplet at: (a) the front of the droplet, (b) the middle plane of the droplet and (c) the back of the droplet. Reproduced from reference [138].

1.3.3 Summary

Both the ray-tracing and holographic methods of optical distortion compensation have been reviewed and considered for this work. Both approaches require knowledge of the shape and refractive index of the sample in order to effect reconstructions. The ray tracing approach has been used successfully in many situations, but is limited in that velocity vectors cannot be extracted close to the edge of the sample. He and Duan introduced a technique that removed this limitation but introduced a necessity for light sheet illumination and a 1:1 imaging system. The holographic approach to distortion compensation is well established in film-based holography, and early work on its digital realisation is promising; although to my knowledge there are currently no examples in the literature where the numerical technique of Wormald and Coupland has been applied to particle velocimetry. The holographic method also has the advantage of offering a means of verifying the estimate of the sample surface by using the a priori knowledge of the illuminating wave front.

1.4 Conclusions

The aim of this project is to develop an experimental tool capable of measuring flows within actual-size ink-jet streams. As there is demand to print ‘inks’ with increasingly complex behaviour, there is a need to produce experimental measurements of ink-jet flows to complement simulations and help to improve the technology. The current prevalent velocimetry technique is particle image velocimetry (PIV), favoured for its ability to produce high resolution velocity fields, non-invasively, in a single measurement. I have reviewed the literature concerning novel approaches to applying PIV to flow systems with sub-millimetre dimensions. The limitations are, broadening of the velocity distributions by Brownian motion, and the problems associated with volume illumination – i.e. particles outside of the desired measurement plane contribute to the raw images and their movements bias the extracted velocity fields. Light from

particles outside a single plane can, however, be exploited in order to measure up to three components of velocity in up to three dimensions.

I have also reviewed techniques that compensate for the distortion of images of particle fields by curved interfaces – particularly extreme in the case of an ink-jet stream with radii of curvature in the tens of microns. The techniques were based on either ray tracing through a known curved boundary or by novel holographic reconstruction.

I conclude from the existing literature that the holographic approach may offer the best solution and that it would be valuable to attempt to apply it to the measurement of velocities inside ink-jet streams.

1.5 References

1 J. Eggers, E. Villermaux, 2008, *Reports on Progress in Physics*, 71(3), 036601.

2 I. M. Hutchings, G. D. Martin (eds.), *Inkjet technology for digital fabrication*, John Wiley & Sons, 2012.

3 P.-G. De Gennes, F. Brochard-Wyart, D. Quéré, *Capillarity and Wetting Phenomena: Drops, Bubbles, Pearls, Waves*, Springer, 2004,

4 T. Young, 1805, *Phil. Trans. R. Soc. London*, 95, 65-87.

5 L. Y. Yang, unpublished work.

6 J. A. F. Plateau, 1850, *Ann. Phys. Chem.*, 156(8), 566.

7 L. Rayleigh, 1878, *Proc. R. Soc. London A*, 10, 4-13.

8 B. Derby, 2010, *Annu. Rev. Mater. Res.*, 40, 395-412.

9 Smithers Pira article on the ink jet market, http://www.smitherspira.com/news/2014/september/inkjet-market-to-grow-by-12-7-from-2014-to-2019, (accessed January 2015)

10 P. Calvert, 2001, *Chem. Mater.*, 13, 3299-3305

11 B. –J., de Gans, P. C. Duineveld, U. S. Schubert, 2004, *Adv. Mater.*, 16(2), 203-213.

12 M. Singh, H. M. Haverinen, P. Dhagat, G. E. Jabbour, 2010, *Adv. Mater.*, 22, 373-685.

13 PV Magazine article on organic electronics, http://www.pv-magazine.com/news/details/beitrag/organic-electronics-market-to-be-worth-796-billion-by-2020_100016825/#axzz3SlilJazr

14 Y. Ishii, S. Koike, Y. Arai, Y. Ando, 2000, *Jpn. J. Appl. Phys. Part 1*, 39, 1490-1493.

15 T. Xu, J. Jin, C. Gregory, J. J. Hickman, T. Boland, 2005, *Biomaterials*, 26, 93-99.

16 R. E. Saunders, B. Derby, 2014, *Int. Mater. Rev.*, 59(8), 430-448.

17 T. Boland, T. Xu, B. Damon, C. Xiaofeng, 2006, *Biotechnol. J.*, 1, 910-917.

18 A. A. Castrejon-Pita, J. R. Castrejon-Pita, I. M. Hutchings, 2012, *Phys. Rev. Lett.*, 108, 074506.

19 C. P. Kothandaraman, R. Rudramoorthy, *Basic Fluid Mechanics*, New age International, 1999.

20 T. Battal, C. D. Bain, M. Weiss, R. D. Darton, 2003, *Journal of Colloid and Interface Science*, 263, 250-260.

21 R. J. Adrian, 1984, *Appl. Opt.*, 23(11), 1690-1691.

22 C. J. D. Pickering, N. A. Halliwell, 1984, *Appl. Opt.*, 23(17), 2961-2969.

23 J. G. Santiago, S. T. Wereley, C. D. Meinhart, D. J. Beebe, R. J. Adrian, 1998, *Exp. Fluids*, 25(4), 316-319

24 R. D. Keane, R. J. Adrian, Y. Zhang, 1995, *Meas. Sci. Technol.*, 6(6),754.

25 S. J. Williams, C. Park, S. T. Wereley, 2010, *Microfluidics and Nanofluidics*, 8(6), 709-726.

26 A. Einstein, 1905, *Ann. Phys. (Leipzig)*, 17, 549. (English translation: Investigations on the Theory of Brownian Movement, Dover, New York, 1956.)

27 C. D. Meinhart, S.T. Wereley, J. G. Santiago, 1999, *Exp. Fluids*, 27(5), 414-419.

28 C. D. Meinhart, S. T. Wereley, J. G. Santiago, 2000, *Journal of Fluids Engineering*, 122(2), 285-289.

29 A. G. Koutaiaris, D. S. Mathioulakis, S. Tsangaris, 1999, *Meas. Sci. Technol.*, 10(11), 1037.

30 C. D. Meinhart, S. T. Wereley, M. H. B. Gray, 2001, *Meas. Sci. Technol.*, 11(6), 809.

31 M. G. Olsen, R. J. Adrian, 2000, *Exp. Fluids*, 29(1), S166-S174.

32 M. G. Olsen, R. J. Adrian, 2000, *Optics & Laser Technology*, 32(7), 621-627.

33 C. D. Meinhart, H. Zhang, 2000, *Journal of Microelectromechanical Systems*, 9(1), 67-75.

34 LaVision GmbH, http://www.lavision.de/en/products/flowmaster/micro-piv.php, (accessed March 2014).

35 TSI Inc., http://www.tsi.com/PIV-System-MicroPIV, (accessed March 2014).

36 Dantec Dynamics, http://www.dantecdynamics.com/microfluidics, (accessed March 2014).

37 D. Sinton, 2004, *Microfluidics and Nanofluidics*, 1(1), 2-21.

38 S. J. Lee, S. Kim, 2009, *Microfluidics and Nanofluidics*, 6(5), 577-588.

39 S. J. Williams, S. T. Wereley, 2010, *Microfluidics and Nanofluidics*, 8(6), 709-726.

40 R. Seemann, M. Brinkmann, T. Pfohl, S. Herminghaus, 2012, *Reports on Progress in Physics*, 75(1), 016601.

41 M. Minsky, 1957, U.S. Patent #3013467.

42 J. S. Park, C. K. Choi, K. D. Kihm, 2004, *Exp. Fluids*, 37(1), 105-119.

43 H. Kinoshita, S. Kaneda, T. Fujii, M. Oshima, 2007, *Lab on a Chip*, 7(3), 388-346.

44 R. Lima, S. Wada, K. I. Tsubota, T. Yamaguchi, 2006, *Meas. Sci. Technol.*, 17(4), 797.

45 R. Lima, S. Wada, M. Takeda, K. I. Tsubota, T. Yamaguchi, 2007, *Journal of Biomechanics*, 40(12), 2752-2757.

46 R. Lima, T. Ishikawa, Y. Imai, M. Takeda, S. Wada, T. Yamaguchi, 2008, *Journal of Biomechanics*, 41(10), 2188-2196.

47 R. Lima, S. Wada, S. Tanaka, M. Takeda, T. Ishikawa, K. I. Tsubota, Y. Imai, T. Yamaguchi, 2008, *Biomedical Microdevices*, 10(2), 153-167.

48 M. J. Patrick, C. Y. Chen, D. H. Frakes, O. Dur, K. Pekkan, 2011, *Exp. Fluids*, 50(4), 887-904.

49 M. Ichiyanagi, Y. Sato, K. Hishida, 2007, *Exp. Fluids*, 43(2-3), 425-435.

50 A. K. Prasad, R. J. Adrian, 1993, *Exp. Fluids*, 15(1), 49-60.

51 I. Grant, 1997, *Proceedings of the Institution of Mechanical Engineers, Part C: Journal of Mechanical Engineering Science*, 211(1), 55-76.

52 H. Klank, G. Goranović, J. P. Kutter, H. Gjelstrup, J. Michelsen, C. H. Westergaard, 2002, *J. Micromech. Microeng.*, 12(6), 862.

53 R. Lindken, J. Westerweel, B. Wieneke, 2005, *In Proc. 6th Int. Symp. on Particle Image Velocimetry PIV'05* (Pasadena, CA, USA).

54 R. Lindken, J. Westerweel, B. Wieneke, 2006, *Exp. Fluids*, 41(2), 161-171.

55 M. R, Bown, J. M. MacInnes, R. W. K. Allen, W. B. J. Zimmerman, 2006, *Meas. Sci. Technol.*, 17(8), 2175.

56 M. R, Bown, J. M. MacInnes, R. W. K. Allen, 2007, *Exp. Fluids*, 42(2), 197-205.

57 J. Giardino, J. Hertzberg, E. Bradley, 2008, *Exp. Fluids*, 45(6) 1037-1045.

58 C. H. Yu, J. H. Yoon, H. B. Kim, 2009, *J. Mech. Sci. Technol.*, 23(3), 845-855.

59 M. R. Bown, J. M. MacInnes, R. W. K. Allen, 2005, *Meas. Sci. Technol.*, 16(3), 619.

60 B. Wieneke, 2005, *Exp. Fluids*, 39(2), 267-280.

61 B. Ovryn, 2000, *Exp. Fluids*, 29(1), S175-S184.

62 M. Born and E. Wolf, *Principles of Optics,* Pergamon Press, 6th edn., 1980, pp 633.

63 M. Speidel, A. Jonáš, and E.-L. Florin, 2003, *Opt. Lett.*, 28(2), 69-71.

64 M. Wu, J. W. Roberts, M. Buckley, 2004, *Exp. Fluids*, 38(4), 461-465.

65 J. S. Park, K. D. Kihm, 2006, *Exp. Fluids*, 40(3), 491-499.

66 S. D. Peterson, H.-S. Chuang, S. T. Wereley, 2008, *Meas. Sci. Technol.*, 19(11), 115406.

67 C. E. Willert, M. Gharib, 1992, *Exp. Fluids*, 12(6), 353-358.

68 F. Pereira, M. Gharib, D. Dabiri, D. Modarress, 2000, *Exp. Fluids*, 29(1), S078-S084.

69 S. Y. Yoon, K. C. Kim, 2006, *Meas. Sci. Technol.*, 17(11), 2897.

70 L. Kajitani, D. Dabiri, 2005, *Meas. Sci. Technol.*, 16(3), 790.

71 F. Pereira, J. Lu, E. Castano-Graff, M. Gharib, 2007, *Exp. Fluids*, 42(4), 589-599.

72 J. Lu, F. Pereira, S. E. Fraser, M. Gharib, 2008, *J. Biomed. Opt.*, 13(1), 014006-014006.

73 W. H. Tien, P. Kartes, T. Yamasaki, D. Dabiri, 2008, *Exp. Fluids*, 44(6), 1015-1026.

74 D. Lin, N. C. Angarita-Jaimes, S. Chen, A. H. Greenaway, C. E. Towers, D. P. Towers, 2008, *Opt. Lett.*, 33(9), 905-907.

75 E. Hecht, *Optics*, Addison-Wesley, 2nd edn., 1987.

76 Y. Pu, H. Meng, 2000, *Exp. Fluids*, 29(2), 184-197.

77 Y. Pu, X. Song, H. Meng, 2000, *Exp. Fluids*, 29(1), S117-S128.

78 D. H. Barnhart, R. J. Adrian, G. C. Papen, 1994, *Appl. Opt.*, 33(30), 7159-7170.

79 J. Zhang, B. Tao, J. Katz, 1997, *Exp. Fluids*, 23(5), 373-381.

80 J. Sheng, E. Malkiel, 2003, *Appl. Opt.*, 42(2), 235-250.

81 H. Meng, G. Pan, Y. Pu, S. H. Woodward, 2004, *Meas. Sci. Technol.*, 15(4), 673-685.

82 J. P. Huignard, P. Günter, *Optical Processing Using Wave Mixing in Photoreactive Crystals*, Springer, 1989, pp 205-273.

83 R. J. Collier, C. B. Burckhardy, L. H. Lin, *Optical Holography*, Academic, New York, 1971

84 K. Kinoshita, 1992, *Japanese Journal of Applied Physics*, 31(1), 1677-1681.

85 D. H. Barnhart, W. D. Koek, T. Juchem, N. Hampp, J. M. Coupland, N. A. Halliwell, 2004, *Meas. Sci. Technol.*, 15(4), 639.

86 K. D. Hinsch, 2002, *Meas. Sci. Technol.*, 13(7), R61-R72

87 J. Soria, C. Atkinson, 2008, *Meas. Sci. Technol.*, 19(7), 074002

88 Y. -S. Choi, K. -W. Seo, M. -H. Sohn, S. -J. Lee, 2012, *Optics and Lasers in Engineering*, 50(1), 39-45.

89 J. P. Fugal, T. J. Schulz, R. A. Shaw, 2009, *Meas. Sci. Technol.*, 20(7), 075501.

90 H. Meng, W. L. Anderson, F. Hussain, D. D. Liu, 1993, *J. Opt. Soc. Am. A*, 10(9), 2046-2058.

91 Y. Pu, H. Meng, 2004, *J. Opt. Soc. Am. A*, 21(7), 1221-1230.

92 L. O. Heflinger, G. L. Stewart, C. R. Booth, 1978, *Appl. Opt.*, 17(6), 951-954.

93 G. Pan, H. Meng, 2003, *Appl. Opt.*, 42(5), 827-833.

94 W. Xu, M. H. Jericho, I. A. Meinertzhagen, H. J. Kreuzer, 2001, *Proceedings of the National Academy of Sciences*, 98(20), 11301-11305.

95 W. Xu, M. H. Jericho, I. A. Meinertzhagen, H. J. Kreuzer, 2002, *Appl. Opt.*, 41(25), 5367-5375.

96 W. Xu, M. H. Jericho, H. J. Kreuzer, I. A. Meinertzhagen, 2003, *Opt. Lett.*, 28(3), 164-166.

97 J. Garcia-Sucerquia, W. Xu, S. K. Jericho, P. Klages, M. F. Jericho, H. J. Kreuzer, 2006, *Appl. Opt.*, 45(5), 836-850.

98 S. K. Jericho, J. Garcia-Sucerquia, W. Xu, M. H. Jericho, H. J. Kreuzer, 2006, *Review of Scientific Instruments*, 77(4), 043706.

99 H.-W. Fink, W. Stocker, H. Schmid, 1990, *Phys. Rev. Lett.*, 65(10), 1204.

100 S.-I. Satake, T. Kunugi, K. Sato, T. Ito, J. Taniguchi, 2005, *Opt. Rev.*, 12(6), 442-444.

101 S.-I. Satake, T. Kunugi, K. Sato, T. Ito, H. Kanamori, J. Taniguchi, 2006, *Meas. Sci. Technol.*, 17(7), 1647.

102 J. Sheng, E. Malkiel, J. Katz, 2006, *Appl. Opt.*, 45(16), 3893-3901.

103 J. Sheng, E. Malkiel, J. Katz, J. Adolf, R. Belas, A. R. Place, 2007, *Proceecdings of the National Academy of Sciences*, 104(44), 17512-17517.

104 J. Sheng, E. Malkiel, J. Katz, 2008, *Exp. Fluids*, 45(6), 1023-1035.

105 S. Kim, S.-J. Lee, 2007, *J. Micromech. Microeng.*, 17(10), 2157.

106 Y.-S. Choi, S.-J. Lee, 2010, *Microfluidics and Nanofluidics*, 9(4-5), 819-829.

107 K. W. Seo, Y.-S. Choi, S.-J. Lee, 2012, *Exp. Fluids*, 53(6), 1867-1877.

108 K. W. Seo, H. J. Byeon, H. K. Huh, S.-J. Lee, 2014, *RSC Advances*, 4(7), 3512-3520.

109 D. Kapfenberger, A. Sonn-Segev, Y. Roichman, 2013, *Optics Express*, 21(10), 12228-12237.

110 Y.-S. Choi, S.-J. Lee, 2009, *Appl. Opt.*, 48(16), 2983-2990.

111 A. T. Hansen, M. Hondzo, J. Sheng, M. J. Sadowsky, 2014, *Freshwater Biology*, 59(2), 312-324.

112 J. Lobera, J. M. Coupland, 2008, *Meas. Sci. Technol.*, 19(2), 025501.

113 S. A. Wormald, J. Coupland, 2009, *Appl. Opt.*, 48(3), 6400-6407.

114 S. A. Wormald, J. M. Coupland, 2010, *Journal of Modern Optics*, 57(9), 700-708.

115 J. K. Abrantes, M. Stanislas, S. Coudert, L. F. A. Azevedo, 2013, *Appl. Opt.*, 52(1), A379-A409.

116 J. Katz, J. Sheng, 2010, *Annu. Rev. Fluid Mech.*, 42, 531-555.

117 B. J. de Witt, H. Coronado-Diaz, R. J. Hugo, *Exp. Fluids*, 2008, 45, 95-109.

118 K. H. Kang, S. J. Lee, C. M. Lee, I. S. Kang, *Meas. Sci. Technol.*, 2004, 15, 1104-1112.

119 G. Minor, P. Oshkai, N. Djilali, *Meas. Sci. Technol.*, 2007, 18, L23-L28.

120 K. H. Kang, H. C. Lim, H. W. Lee, S. J. Lee, *Physics of Fluids*, 2013, 25, 042001.

121 S. Tasumatsu, K. Nakaso, J. Fukai, *Journal of Chemical Engineering of Japan*, 2012, 45, 128-135.

122 G. Minor, N. Djilali, D. Sinton, P. Oshkai, *Fluid Dyn. Res.*, 2009, 41, 045506.

123 M. Kaneda, K. Hyakuta, Y. Takao, H. Ishizuka, J. Fukai, *Langmuir*, 2008, 24, 9102-9109.

124 L. Davoust, Y. Fouillet, R. Malk, J. Theisen, *Biomicrofluidics*, 2013, 7, 044104.

125 H. Lee, S. Yun, S. H. Ko, K. H. Kang, *Biomicrofluidics*, 2009, 3, 044113.

126 S. H. Ko, H. Lee, K. H. Kang, *Langmuir*, 2008, 24, 1094-1101.

127 M. I. Smith, V. Bertola, *Exp. Fluids*, 2011, 50, 1385-1391.

128 B. He, F. Duan, *Applied Physics Letters*, 2013, 103, 053508.

129 Y.-P. Liu, P.-Y. Wang, J. Wang, Z.-H. Du, *Cryogenics*, 2013, 55, 20-29.

130 J. Dannemann, K. Pielhop, M. Klaas, W. Schröder, *Exp. Fluids*, 2011, 50, 961-976.

131 J. R. Castrejon-Pita, S. D. Hoath, I. M. Hutchings, *Journal of Fluids Engineering*, 2012, 134, 011201.

132 S. Gier, C. Wagner, *Physics of Fluids (1994-present)*, 2012, 24, 053102.

133 L. O. Heflinger, G. L. Stewart, C. R. Booth, *Appl. Opt.*, 1978, 17, 951-954.

134 D. H. Barnhart, R.J. Adrian, G. C. Papen, *Appl. Opt.*, 1994, 33, 7159-7170.

135 D. H. Barnhart, R. J. Adrian, R. J. Meinhart, G. C. Papen, *In SPIE's 1995 International Symposium on Optical Science, Engineering, and Instrumentation*, 1995, 2545, 165-175.

136 D. H. Barnhart, V. S. S. Chan, N. A. Halliwell, J. M. Coupland, *Exp. Fluids*, 2002, 33, 770-780.

137 R. Konrath, W. Schröder, W. Limberg, *Exp. Fluids*, 2002, 33, 781-793.

138 S. A. Wormald, J. M. Coupland, *Journal of Modern Optics*, 2010, 57, 700-708.

2 Background

2.1 Light as a Wave

There are a few prerequisites about the wave nature of light that are useful to bear in mind before I move on to a discussion of the holographic method. In this section I will discuss the recording of (visible) light, its interference, coherence and diffraction.

Light is a transverse electromagnetic wave which obeys Maxwell's equations. A light wave can be described by equation (2.1), it is a solution to the wave equation in (2.2), which follows from Maxwell's equations

$$\mathbf{E}(\boldsymbol{r}, t) = \mathbf{A}\exp\{i(\varphi\,(\boldsymbol{r}) - \omega t)\} \tag{2.1}$$

$$\nabla^2\mathbf{E} - \frac{1}{c^2}\frac{\partial^2\mathbf{E}}{\partial t^2} = 0. \tag{2.2}$$

The wavefunction $\boldsymbol{E}$ is a function of the vector amplitude $\mathbf{A}$, time t and position; c is the speed of light.

Transverse waves oscillate perpendicular to the direction of propagation therefore, to describe an electromagnetic wave fully, the pre-exponential factor, $\mathbf{A}$, must be a vector. For most work the approximation that oscillations occur in a single plane – known as the scalar approximation – is valid. Individual waves are assumed to be plane-polarised or a linear combination of two orthogonally polarised components. This assumption and where it can be legitimately applied is discussed in more detail in section 2.3.2.4.

2.1.1 Intensity

Electromagnetic waves in the visible spectrum oscillate too fast, around 10^{14} Hz, for the instantaneous displacement (wave function) to be measured directly. Instead,

photosensitive media are responsive to intensity, the incident optical power, which is given by[1]

$$I = \frac{cn\epsilon_0}{2}|\mathrm{E}|^2,$$

where, n is the refractive index and ϵ_0 is the vacuum permittivity. In practice, the factor of $cn\epsilon_0/2$ is usually neglected.

2.1.2 Interference

The superposition of multiple waves is known as interference. The linearity of the wave equation means that superposition is simply a sum of the individual wave functions. Consider the case of two monochromatic waves with the same frequency and the complex amplitudes:

$$\mathrm{A}_1(\boldsymbol{r},t) = a_1\exp\{i(\varphi_1(\boldsymbol{r}) - \omega t)\}$$

and

$$\mathrm{A}_2(\boldsymbol{r},t) = a_2\exp\{i(\varphi_2(\boldsymbol{r}) - \omega t)\}.$$

They superpose to give

$$\mathrm{A}(\boldsymbol{r},t) = \mathrm{A}_1(\boldsymbol{r},t) + \mathrm{A}_2(\boldsymbol{r},t).$$

Upon exposure of a photosensitive medium (photographic film, digital sensor, etc.) to the light, the intensity of the pattern recorded is:

$$\begin{aligned} I(\boldsymbol{r}) &= |\mathrm{A}_1(\boldsymbol{r},t) + \mathrm{A}_2(\boldsymbol{r},t)|^2 = \big(a_1(\boldsymbol{r},t) + a_2(\boldsymbol{r},t)\big)^*\big(a_1(\boldsymbol{r},t) + a_2(\boldsymbol{r},t)\big) \\ &= (a_1\exp\{-i(\varphi_1(\boldsymbol{r}) - \omega t)\} + a_2\exp\{-i(\varphi_2(\boldsymbol{r}) - \omega t)\}) \\ &\quad * (a_1\exp\{i(\varphi_1(\boldsymbol{r}) - \omega t)\} + a_2\exp\{i(\varphi_2(\boldsymbol{r}) - \omega t)\}) \\ &= {a_1}^2 + {a_2}^2 + a_1a_2\exp\big\{i\big(\varphi_1(\boldsymbol{r}) - \varphi_2(\boldsymbol{r})\big)\big\} \\ &\quad + a_1a_2\exp\big\{-i\big(\varphi_1(\boldsymbol{r}) - \varphi_2(\boldsymbol{r})\big)\big\}. \end{aligned} \tag{2.3}$$

There are four terms in the result, the first two are simply the intensities of each of the waves alone, and the second two, known as the cross terms, vary depending on the phase difference of the two waves. It should also be noted that the intensity pattern is only independent of time if the interfering waves have the same frequency. For the remainder of this section, I will restrict the discussion to waves of the same frequency and will therefore drop the time-dependant ωt term.

Applying Euler's formula to equation (2.3) gives the following relationship

$$I = {a_1}^2 + {a_2}^2 + 2a_1a_2 \cos\varphi,$$

where $\varphi = \varphi_1(\boldsymbol{r}) - \varphi_2(\boldsymbol{r})$. The interference pattern does not depend on the sign of the phase difference and varies from minima (dark fringes), where φ is an odd multiple of π, to maxima (bright fringes), where φ is an even multiple of π.

2.1.3 Coherence

Coherence is ability of light to exhibit interference effects. It is the correlation between the phases of parts of the same wave either separated in space or time – known as spatial and temporal coherence respectively. Spatial coherence is the correlation between waves from different parts of the same extensive source, usually high for laser sources.

Temporal coherence is related to the bandwidth of a light source. No source emits truly monochromatic light for several reasons: emitted wave trains have a finite length, atomic vibrations cause Doppler shifts in emitted waves and thermal fluctuations cause small random changes in the energy levels in the electron transitions that emit the photons.[2] Temporal coherence is usually quoted in terms of a coherence length: the path offset that will cause a 50% reduction in interference contrast. The coherence length is usually estimated by[3]

$$\mathrm{L} = \frac{\lambda^2}{\Delta\lambda},$$

where λ is the central wavelength of the distribution and $\Delta\lambda$ the spectral linewidth.

2.1.4 Diffraction

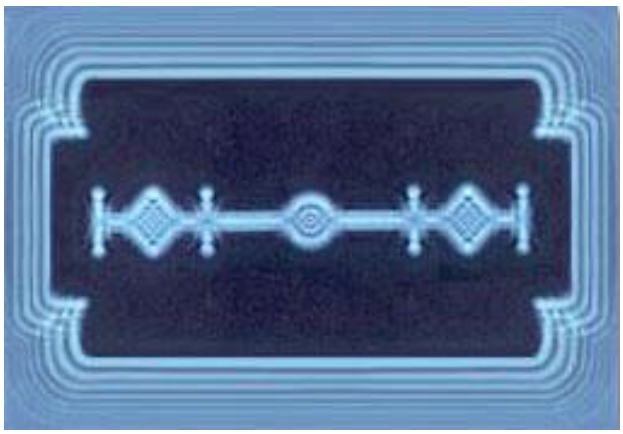

Figure 2.1 Diffraction of white light by a razor blade. Reproduced from reference [14].

The phenomenon of diffraction was first discovered by the Italian Jesuit priest Francesco Grimaldi. His findings were first published in 1665[4] and included descriptions of the bright and dark "fringes" formed when a rod was illuminated by a small light source. Figure 2.1 shows the diffraction of white light by the edge of a razor blade, where the physical scale of its edge is comparable to the wavelength of light.

Christiaan Huygens in 1678 was the first to attempt a theory describing the phenomenon.[4] In his work on the wave nature of light, *Traite de la Lumiere*, he made the well-known assertion that if every point on a wavefront is the source of a spherical wavelet, a new wavefront is formed by the envelope of these secondary wavelets. In spite of the work of Grimaldi and Huygens, the wave theory of light failed to gather much support – often attributed to Isaac Newton's advocacy of the corpuscular theory in his *Opticks.*[4]

More than a century later, in 1802, Thomas Young discovered the concept of interference. He found that, in certain situations, darkness could result from the summation of light.[5] This was irrefutable evidence that light could behave as a wave. In 1818, Augustin Fresnel combined Young's ideas of interference with Huygens' wavelets.[1] He found that if he were to allow the secondary wavelets to interfere with each other, making some arbitrary assumptions about their relative amplitudes and

phases, he was able to accurately predict the distribution of intensity in diffraction patterns.

In 1882, Gustav Kirchhoff built on Fresnel and Huygens' work, showing that the amplitudes and phases given to the sources were logical given the wave nature of light.[1] Kirchhoff's derivation was based on two assumptions of the boundary values of the light at the diffracting aperture, two assumptions that were later proved to be contradictory.[6] Sommerfeld later removed one of these assumptions by using a different choice of Green's function in his derivation of the so-called Rayleigh-Sommerfeld diffraction theory.[6] The theories of Kirchhoff and Sommerfeld, discussed in greater detail in section 2.3, are both capable of predicting the diffraction of light to a high degree of accuracy despite their differences.

2.2 Holography

Holography is one of the most interesting developments in modern optics. It has many applications in industry, science and art. Holography was invented by Denis Gabor in 1948, who had been concerning himself with improvements to the electron microscope.[7] He realised that if both defining properties of a wave front, its amplitude and phase, could be recorded, the result would be a complete representation of the field at the detector. He reasoned that phase could be encoded if there were something to compare it to – achieved by a mutually coherent reference wave. The resulting interference pattern he called a "hologram", coming from the Greek word for "whole". Not only did Gabor devise a method to obtain a complete recording of a wave, he also realised that if the reference wave was passed back through the developed film then the light would diffract to form a 3D image of the object.

Coherence is the ability of light to form interference fringes. This is a valuable characteristic for a source of illumination in holography and, in the 1940s when Gabor preformed his experiments, available light sources had very short coherence lengths which limited his progress. The source Gabor used was a mercury lamp and a colour filter, extracting a single spectral line with a coherence length of around 0.1 mm.[8]

Experiments at this time were limited to 'in-line' holograms of transparencies with opaque printed letters. The technique received limited interest at this stage and had to wait until the invention of a high coherence light source – the laser. In 1962, the first laser holograms were taken by Leith and Upatnieks.[9] Taking full advantage of the greater coherence length of a laser source, they used an off-axis geometry where the reference travelled around the object rather than through it.

In the next section I will present the possible recording and reconstruction geometries, simple mathematical descriptions of the recorded and resulting waves, the theory of the reconstruction, and how this may be used in numerical recombination algorithms.

2.2.1 Recording

Holograms are simply a means to encode the amplitude and phase of an incident wave on some sort of medium. As photosensitive media are sensitive only to amplitude but not to phase, an ordinary photograph loses information and can never be used to reconstruct the 'view' of an object. However, if a wave front of known – or at least reproducible – amplitude and phase is added to the wave due to our object, the result is an interference pattern – a modulation of the amplitude of the field at the detector related to the relative phase of the object wave front. Suppose some field, O, is scattered from an object, defined as

$$O = a_O(x, y) \exp\{i\varphi\ (x, y)\}, \tag{2.4}$$

where, a_O is the complex amplitude and φ is the phase of the object wave. The reference wave that interferes with it is defined as

$$R = a_R(x, y) \exp\{i\Phi\ (x, y)\}. \tag{2.5}$$

The total field at the detector is then $O + R$, and the recorded intensity pattern is given by

$$
\begin{aligned}
I(x,y) &= |O+R|^2 \\
&= |a_R(x,y)|^2 + |a_O(x,y)|^2 \\
&+ a_O(x,y)a_R(x,y)\exp\{i\varphi\,(x,y) - i\Phi\,(x,y)\} \\
&+ a_O(x,y)a_R(x,y)\exp\{i\Phi\,(x,y) + i\varphi\,(x,y)\}.
\end{aligned}
\tag{2.6}
$$

To make the notation less bulky, the form below will be used

$$I(x,y) = |R|^2 + |O|^2 + R^*O + RO^*, \tag{2.7}$$

where, * denotes complex conjugation. While phase information is lost in the first two terms, it is retained the last pair of terms (the cross-terms).

Typically, the intensity pattern is recorded on a linear detector, such as a photographic film or CCD. This situation is described using a slightly different notation. When the first term, $|R|^2$, is uniform across the detector it can be replaced by a constant, t_B (the transmission bias). The recorded signal, t_A(known as the transmission amplitude) is then given by[10]

$$t_A(x,y) = t_B + \gamma(|O|^2 + R^*O + RO^*), \tag{2.8}$$

where γ is the proportionality constant from the gradient of the transmission versus exposure curve.

2.2.2 Optical Reconstruction

In this section I look at how the information contained within a recorded hologram can be recovered or reconstructed. For a hologram recorded on film this can be done directly, by illuminating it with a coherent reconstruction beam, $B(x,y)$. The light transmitted by the hologram is the product of the amplitude transmittance function and the reconstructing wave

$$B(x,y)t_A(x,y) = t_BB + \gamma|O|^2B + \gamma R^*OB + \gamma RO^*B. \tag{2.9}$$

If a copy of the reference wave is used to re-illuminate the hologram, i.e. $B = R$, then the third component of equation (2.9) becomes $\gamma|R|^2O(x,y)$, which, barring a constant

multiplicative factor, is the same as the object wave. Being the same as the object wave, this component carries on propagating through space as the object wave had been when it reached the detector. The eye interprets this wave as coming from a virtual 3D image of the object.

If the hologram is illuminated by the conjugate of the reference wave, $B = R^*$, the fourth component of equation (2.9) becomes $\gamma|R|^2 O^*(x, y)$, the conjugate of the object wave. This part converges as it propagates away from the hologram to form a real image.

The second term is not constant across the detector and is a potential source of noise in any reconstruction but its influence can be minimised by making sure that much more light comes from the reference beam than the object , i.e. $|R|^2 > |O|^2$. The effect of the real and virtual image on the reconstructed hologram depends on the geometry used to record the hologram, and is discussed in the next section.

2.2.3 Recording Geometries

The two broad types of hologram recording geometry will be discussed here: in-line – the type used by Gabor to produce the very first holograms – and off-axis – the technique invented by Leith and Upatnieks which can produce less noisy reconstructed images at the expense of a much more complicated optical setup.

2.2.3.1 Gabor (In-Line) Holography

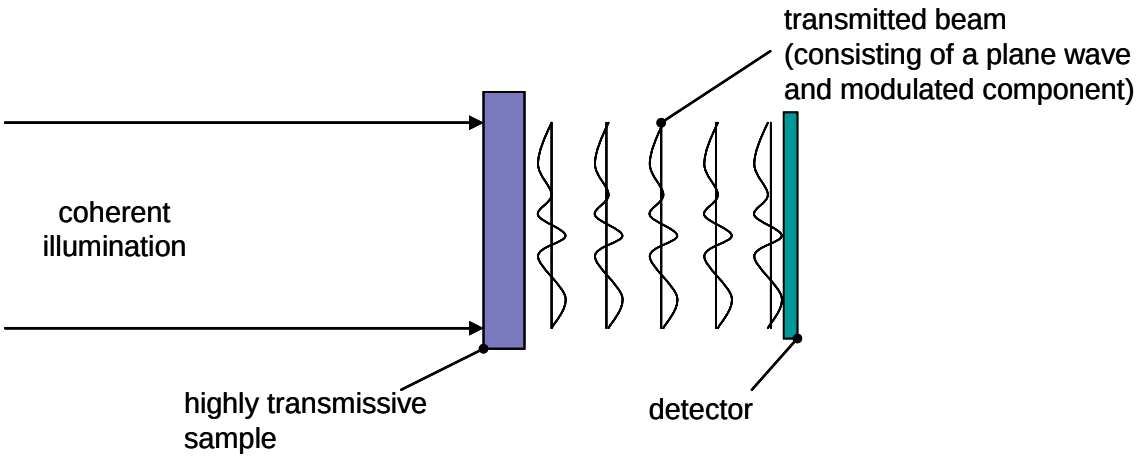

Figure 2.2 Typical in-line hologram recording.

The Gabor or in-line method of recording holograms uses a single beam as both the source of illumination and reference light (figure 2.2). The constraints with this geometry are that the object must be transparent and highly transmissive – so that most of the light that passes through remains unperturbed by the sample, thus minimising the contribution from the second term in equation (2.9).

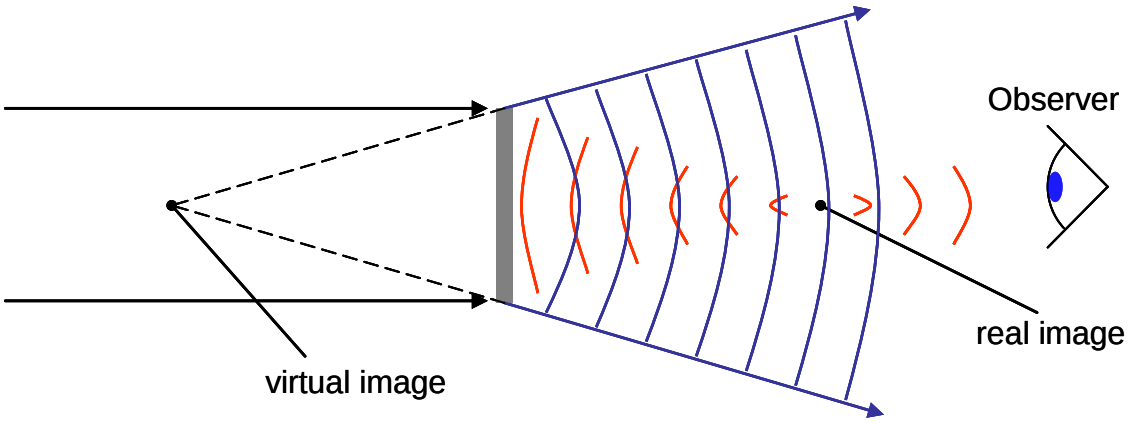

Figure 2.3 Viewing an in-line hologram of a point object.

The unfortunate side-effect of this geometry is that in order to view the reconstructed image, one must look directly into the reconstructing beam (figure 2.3). Also, when

viewing one of the images, light due to the other out-of-focus image reaches the observer and is a source of noise.

If the various reconstructed and transmitted waves could be separated from each other in space, then much clearer images could be observed. At the expense of losing some of the simplicity of the optical bench, separation can be achieved in the off-axis technique.

2.2.3.2 Off-Axis Holography

Off-axis holograms are those with geometry similar to Leith and Upatnieks' first demonstrations.[9] The beam from the laser is split into two parts: one part is directed to the object, where it is either transmitted (transparent object) or reflected towards the detector; the other part is the reference wave and follows a separate line and is finally directed toward the detector at some small angle to the normal (figure 2.4).

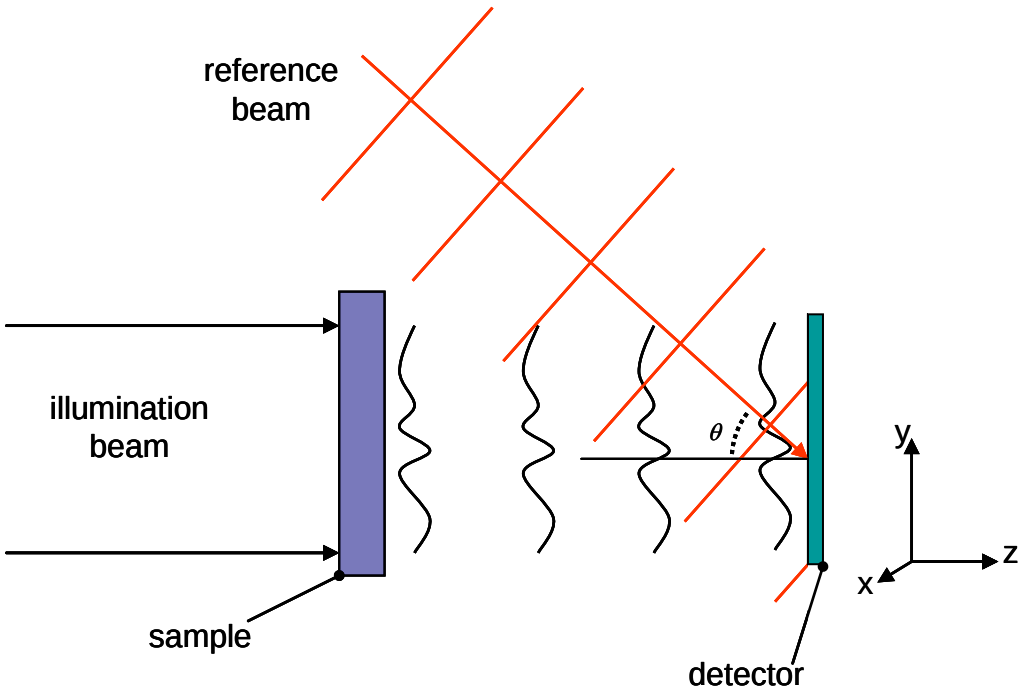

Figure 2.4 Off-axis hologram recording.

Assuming that the reference wave is a plane wave striking the detector at some angle, θ, we can express it as

$$R = a_R \exp\left(-i2\pi \frac{\sin\theta}{\lambda} y\right), \tag{2.10}$$

giving an intensity pattern on the detector

$$\begin{aligned} I(x,y) = |R|^2 + |O|^2 + a_O a_R \exp\big(iky\sin\theta + i\varphi(x,y)\big) \\ + a_O a_R \exp\big(-iky\sin\theta - i\varphi(x,y)\big), \end{aligned} \tag{2.11}$$

where $k = 2\pi/\lambda$. As before, the four terms that make up the transmittance function of the exposed film are:

$$t_1 = t_B$$

$$t_2 = \gamma |a_O(x,y)|^2$$

$$t_3 = \gamma a_R a_O(x,y) \exp\big(+iky\sin\theta + i\varphi(x,y)\big)$$

$$t_4 = \gamma a_R a_O(x,y) \exp\big(-iky\sin\theta - i\varphi(x,y)\big).$$

If the hologram is illuminated along the optical axis by a plane reconstruction wave, the first two terms are transmitted directly along the optical axis – these terms are free from any bulk modulation that acts to diffract the light away from the normal. Components t_3 and t_4, however, will be transmitted at $+\theta$ and $-\theta$ respectively. The component t_3 will be proportional to the object wave and forms a virtual image which can be viewed by eye without looking directly into the (usually laser) reconstruction beam. The component t_4 is proportional to the conjugate of the object wave and propagates as the object wave with time reversed and forms the real image.

The key feature here is that in a well-conceived off-axis holography experiment, all terms are separated in space and separately observable in an optically reconstructed hologram. This feature is also of help in digital holography, where the angular separation of the object and reference beams separates the two cross terms (t_3 and t_4) from the DC terms (t_1 and t_2) in the spatial frequency spectrum (Fourier transform of the image) provided that the angle θ is not too small.

In frequency space, the terms are:

$$G_1(f_x, f_y) = \mathcal{F}\{t_1(x,y)\} = t_B\delta(f_x, f_y)$$

$$G_2(f_x, f_y) = \mathcal{F}\{t_2(x,y)\} = \gamma a_R G_O(f_x, f_y) \star G_O(f_x, f_y)$$

$$G_3(f_x, f_y) = \mathcal{F}\{t_3(x,y)\} = \gamma R^* G_O\left(f_x, f_y - \frac{\sin\theta}{\lambda}\right)$$

$$G_4(f_x, f_y) = \mathcal{F}\{t_4(x,y)\} = \gamma R^* G_O\left(-f_x, -f_y - \frac{\sin\theta}{\lambda}\right),$$

where, $\mathcal{F}$ denotes the Fourier transform and G_O is the spectrum of the object beam. Supposing that the highest spatial frequency in G_O is W cycles/meter, the spectrum takes the form sketched in figure 2.5(a). Figure 2.5(b) is a sketch of the spectrum of hologram transmittance. The central region is made up of the delta function, G_1 and the autocorrelation of G_0 – extending up to 2W, G_2. The two outer terms are G_3, proportional to G_0 and displaced to centre at (0,$\sin(\theta/\lambda)$) and G_4, the reflection of G_3, centred (0,$-\sin(\theta/\lambda)$). In order for these terms to be separable in the spectrum of a hologram, the outer terms must not overlap with the central terms. Inspection of the diagram gives the criterion that, $\sin(\theta/\lambda) > 3\mathrm{W}$ for the terms to be distinct. If the object beam is much less intense than the reference, the term G_2 will be negligible in comparison to the side bands and the minimum angle becomes

$$\theta_{\min} = \sin^{-1}(\mathrm{W}\lambda). \qquad (2.12)$$

In digital holography, single cross terms may be isolated from the spectrum for later processing by simply setting all other areas of the frequency spectrum of the recorded intensity, t_A, to 0. The resulting reconstructions will be free from any effects due to the DC terms (G_1 and G_2) or the other interference term.

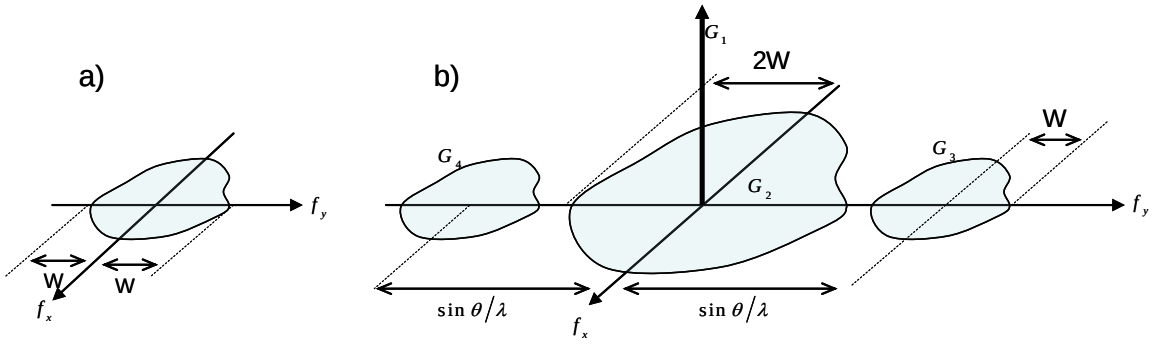

Figure 2.5 a) Spectrum of the object beam and b) spectrum of the hologram. Adapted from reference [6].

2.3 Scalar Diffraction Theory

Digital holography has several advantages over film holography. It is less labour-intensive without the need to develop the exposed film but there is no direct way to replay the information hidden inside optically. Instead, the extracted amplitudes and phases at the hologram plane have to be numerically propagated through space to recover real images of the sample. Typically, the numerical reconstruction of holograms is based on scalar diffraction theory. Scalar diffraction theory makes some simplifying assumptions about the nature of light and provides a means to calculate the relative amplitude and phase of the electric field based on the field elsewhere in space. In this section I show derivations for the general case and for the specific case of diffraction from a planar aperture – particularly relevant to holography.

2.3.1 The integral theorem of Helmholtz and Kirchhoff

The ability to calculate the electric field at any point, provided it is known on any arbitrary surface surrounding that point, is invaluable in the digital reconstruction of holograms. This section demonstrates the derivation of the integral theorem of Helmholtz and Kirchhoff which allows this calculation. The method presented below largely follows that of Goodman.[6]

The calculation of the effect of complex disturbance at an observation point in space can be accomplished by making use of Green's theorem. Green's theorem is a special case of Gauss's theorem and can be expressed as:

$$\iiint_{V} (U\nabla^2 G - G\nabla^2 U)dv = \iint_{S} \left(U\frac{\partial G}{\partial n} - G\frac{\partial U}{\partial n}\right) ds, \tag{2.13}$$

where U and G are scalar functions of position, S is a closed surface surrounding a volume V and $\partial/\partial n$ denotes a partial derivative in the outward normal direction at each point on S. Equation (2.13) is only true if U and G, their first and their second derivatives are single-valued and continuous on and within the surface S. For a good choice of the surface of integration and auxiliary function, G, the theorem can be applied to the diffraction problem. For this reason, Goodman refers to it as the 'prime foundation of scalar diffraction theory'.[6] Auxillary functions (G) are typically chosen for algebraic convenience, so that equations may be simplified easily, and are known as Green's functions.

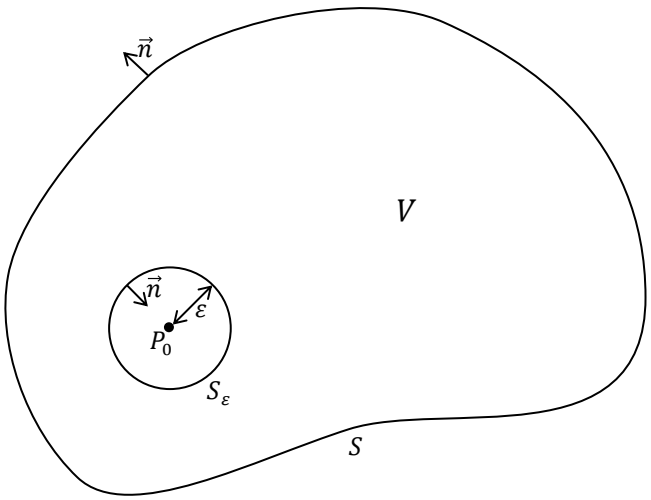

Figure 2.6 Closed surface of integration.

Using the geometry sketched in figure 2.6, the point of observation is P_0 and S is the closed surface surrounding it. Kirchhoff solved the problem by applying Green's

theorem, choosing a unit-amplitude spherical expanding wave as his ancillary function. This is known as the free space Green's function and is given by

$$G(P_1) = \frac{\exp(ikr_{01})}{r_{01}}, \tag{2.14}$$

where r_{01} is the length of the vector pointing from P_0 to P_1.

In order to apply Green's theorem, the field must be continuous within the whole volume of integration. Being rigorous, the discontinuity at P_0 ($1/r_{01}$ becoming undefined) would violate this condition. The geometry of the problem must be slightly complicated by defining a small spherical surface S_ε, of radius ε, around the point P_0. It is now possible to properly apply Green's theorem to the volume between S and S_ε. The surface of integration, S', will be a combination of the two surfaces, $S' = S + S_\varepsilon$.

The source field, U, and the Green's function, G, are both solutions to the scalar Helmholtz equation i.e.

$$(\nabla^2 + k^2)U = 0 \tag{2.15}$$

and

$$(\nabla^2 + k^2)G = 0. \tag{2.16}$$

By substituting (2.15) and (2.16) into the left hand side of the Green's equation (2.13), the terms in the volume integrand cancel, leaving

$$\iint_{S'} \left(U\frac{\partial G}{\partial n} - G\frac{\partial U}{\partial n}\right) ds = 0, \tag{2.17}$$

which can be decomposed into

$$-\iint_{S_\varepsilon} \left(U\frac{\partial G}{\partial n} - G\frac{\partial U}{\partial n}\right) ds = \iint_{S} \left(U\frac{\partial G}{\partial n} - G\frac{\partial U}{\partial n}\right) ds\,. \tag{2.18}$$

In general on the surface, the Green's function is

$$G(P_1) = \frac{\exp(ikr_{01})}{r_{01}}$$

and its normal derivative is

$$\frac{\delta G(P_1)}{\delta n} = \cos(\vec{n}, \vec{r}_{01}) \left(ik - \frac{1}{r_{01}} \right) \frac{\exp(ikr_{01})}{r_{01}}, \tag{2.19}$$

where $\cos(\vec{n}, \vec{r}_{01})$ is the cosine of the angle between the outward normal $\vec{n}$ and the vector $\vec{r}_{01}$. In the specific case where P_1 lies on S_ε, the substitutions $\cos(\vec{n}, \vec{r}_{01}) = -1$ and $r_{01} = \varepsilon$ are made

$$G(P_1) = \frac{\exp(ik\varepsilon)}{\varepsilon} \text{ and } \frac{\delta G(P_1)}{\delta n} = \left(\frac{1}{\varepsilon} - ik \right) \frac{\exp(ik\varepsilon)}{\varepsilon}.$$

By allowing ε to become arbitrarily small, and by assuming that U and its derivative are continuous over the small – but finite – area of S_ε, the integral on the left hand side of equation (2.18) is simplified as follows:

$$\begin{aligned}
\lim_{\varepsilon \to 0} \iint_{S_\varepsilon} \left(U \frac{\partial G}{\partial n} - G \frac{\partial U}{\partial n} \right) ds &= \lim_{\varepsilon \to 0} \iint_{S_\varepsilon} \left(U(P_1) \left(\frac{1}{\varepsilon} - ik \right) \frac{\exp(ik\varepsilon)}{\varepsilon} - \frac{\partial U(P_1)}{\partial n} \frac{\exp(ik\varepsilon)}{\varepsilon} \right) ds \\
&= \lim_{\varepsilon \to 0} \left(U(P_1) \left(\frac{1}{\varepsilon} - ik \right) \frac{\exp(ik\varepsilon)}{\varepsilon} - \frac{\partial U(P_1)}{\partial n} \frac{\exp(ik\varepsilon)}{\varepsilon} \right) \iint_{S_\varepsilon} ds \\
&= \lim_{\varepsilon \to 0} \left(U(P_1) \left(\frac{1}{\varepsilon} - ik \right) \frac{\exp(ik\varepsilon)}{\varepsilon} \right. \\
&\quad \left. - \frac{\partial U(P_1)}{\partial n} \frac{\exp(ik\varepsilon)}{\varepsilon} \right) \int_0^{\pi} \int_0^{2\pi} \epsilon^2 \sin\theta \, d\theta d\phi \\
&= \lim_{\varepsilon \to 0} \left(U(P_1) \left(\frac{1}{\varepsilon} - ik \right) \frac{\exp(ik\varepsilon)}{\varepsilon} - \frac{\partial U(P_1)}{\partial n} \frac{\exp(ik\varepsilon)}{\varepsilon} \right) 4\pi\epsilon^2 \\
&= 4\pi U(P_1).
\end{aligned}$$

Substituting the result into (2.18) gives

$$U(P_1) = \frac{1}{4\pi} \iint_S \left\{ \frac{\partial U}{\partial n} \left[\frac{\exp(ikr_{01})}{r_{01}} \right] - U \frac{\partial}{\partial n} \left[\frac{\exp(ikr_{01})}{r_{01}} \right] \right\} ds. \tag{2.20}$$

Equation (2.20), the integral theorem of Helmholtz and Kirchhoff, is the solution to the homogenous scalar wave equation at any point P_1 in terms of the values of the scalar field and its first derivative on any surface surrounding P_1.

2.3.2 Diffraction by a Planar Screen

In the previous section we followed a derivation of an integral allowing the solution to the wave equation at a certain point in space to be found, provided that we know the value of the wave equation and its first derivative on any arbitrary closed surface around that point.

The most basic aim in digital holography is to predict the diffraction from a recorded plane, so we will continue to follow the development of Kirchhoff's diffraction theory as it is simplified for the case of a plane diffracting aperture.

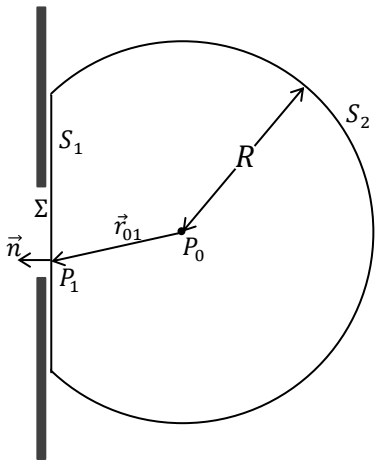

Figure 2.7 Geometry for Kirchhoff formulation of diffraction by a planar aperture. Reproduced with permission from reference [6].

The problem is illustrated in figure 2.7, a monochromatic plane wave illuminates a screen from the left and the diffracted field is observed at P_0 on the right hand side of the aperture Σ.

The closed surface, rather than being arbitrary, is chosen carefully this time. It is made up of two parts, part of the plane directly behind the aperture, S_1, and a spherical cap, S_2, centred on the observation point with a radius of R. Applying equation (2.20) to this composite surface yields

$$U(P_0) = \frac{1}{4\pi}\iint_{S_1}\left(\frac{\partial U}{\partial n}G - U\frac{\partial G}{\partial n}\right)ds + \frac{1}{4\pi}\iint_{S_2}\left(\frac{\partial U}{\partial n}G - U\frac{\partial G}{\partial n}\right)ds. \tag{2.21}$$

From equation (2.14) on the surface S_2,

$$G = \frac{\exp(ikR)}{R}$$

and, for an arbitrarily large R, from equation (1.8)

$$\frac{\delta G}{\delta n} = \left(ik - \frac{1}{R}\right)\frac{\exp(ikR)}{R} = ikG. \tag{2.22}$$

The second integral in (2.21) thus becomes

$$\iint_{S_2}\left[G\left(\frac{\partial U}{\partial n} - ikU\right)\right]ds. \tag{2.23}$$

Equation (2.23) is recast in terms of the solid angle Ω: the range of angles θ and ϕ that define the surface S_2. The product of G and R is constant over the spherical cap and can be taken outside of the integral

$$\iint_{\Omega}\left[G\left(\frac{\partial U}{\partial n} - ikU\right)\right]R^2 d\omega = GR\iint_{\Omega}R\left(\frac{\partial U}{\partial n} - ikU\right)d\omega. \tag{2.24}$$

The integral in equation (2.24) will vanish as $R \to \infty$ if the following condition, known as the *Sommerfeld radiation condition*[11], is satisfied

$$\lim_{R\to\infty} R\left(\frac{\partial U}{\partial n} - ikU\right) = 0. \tag{2.25}$$

The above equation is true if the field vanishes at distances approaching infinity – only necessarily true if waves radiate out of the space and there are no sources outside of the space (at infinity) radiating inwardly. In the geometry chosen for this problem waves only travel outwardly through S_2 and the Sommerfeld radiation condition can be invoked. The integral over S_2 in (2.21) therefore contributes exactly zero to the result.

2.3.2.1 Kirchhoff's Boundary Conditions

Having removed the integral over S_2, we can express the field at the observation point P_0 in terms of the field and its first derivative on a plane directly behind the screen:

$$U(P_0) = \frac{1}{4\pi} \iint_{S_1} \left(\frac{\partial U}{\partial n} G - U \frac{\partial G}{\partial n} \right) ds. \tag{2.26}$$

As described in figure 2.7, the screen is opaque apart from the aperture Σ. It seems logical that the integral would be dominated by points located on Σ, where one would expect the integrand to be largest. Kirchhoff expressed this idea in the form of two assumptions[6]:

1. Across the aperture Σ, the field U and its normal derivative $\partial U/\partial n$ are exactly the same as they would be without the screen.
2. Over the part of S_1 which is directly behind the opaque part of the screen, U and $\partial U/\partial n$ are identically zero.

Making these two assumptions, equation (2.27) can be simplified greatly so that it no longer depends on the field over the whole very large surface S_1:

$$U(P_0) = \frac{1}{4\pi} \iint_{\Sigma} \left(\frac{\partial U}{\partial n} G - U \frac{\partial G}{\partial n} \right) ds. \tag{2.27}$$

It is worth noting that neither of these assumptions is really true. Placing the screen in the illuminating field will always have some effect on the field at Σ as along the rim of the aperture some boundary conditions must be met that would not be necessary without the screen. However, Kirchhoff's diffraction formula is still able to predict very accurate diffraction patterns for apertures with dimensions that are large compared to the wavelength of light. The internal inconsistencies are treated in the following section.

2.3.2.2 Alternative choice of Green's Function

The problem with Kirchhoff's boundary conditions is that both U and $\partial U/\partial n$ are zero behind the opaque part of the screen. According to Goodman,[6] if a field and its normal derivative both vanish on any finite surface element then the field must vanish in all space. The implication is that, if U and $\partial U/\partial n$ are both zero on any part of the plane S_1 then, the field must be zero everywhere behind the screen. This clearly opposes what is known to happen when an aperture is illuminated.

To recap, equation (2.26) allows the field at some observation point can to be written in terms of the incident field and its normal derivative across the screen. The equation is valid if the scalar theory holds (later, in section 2.3.2.4), if U and G are both solutions to the homogeneous scalar wave equation and if the Sommerfeld radiation condition is satisfied.

If the equation could be modified such that either G or $\partial G/\partial n$ vanish over the whole surface S_2, then it would not be necessarily to impose the boundary condition that both U and $\partial U/\partial n$ must be simultaneously zero on any part of that surface. Sommerfeld proved that the equation could be modified in such a way by the following choice of a different Green's function.

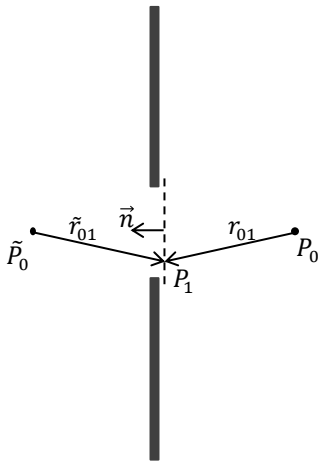

Figure 2.8 Sommerfeld formulation of diffraction from a plane screen. Reproduced with permission from reference [6].

Sommerfeld proposed a Green's function that was not only the field generated by a point source placed at P_0, but the field generated by point sources placed at both P_0 and $\widetilde{P_o}$, the mirror image of P_0 on the opposite side of the screen (see figure 2.8). The sources are of the same wavelength and strength but oscillate with a π phase difference. Such a Green's function would be written

$$G_{-}(P_1) = \frac{\exp(ikr_{01})}{r_{01}} - \frac{\exp(ik\tilde{r}_{01})}{\tilde{r}_{01}}. \tag{2.28}$$

The above function vanishes on the plane directly between the two sources – where both exponentials have the same value but opposite signs. Substituting equation (2.28) into equation (2.26), the observed field can be written as

$$U(P_0) = -\frac{1}{4\pi}\iint_{\Sigma}\left(U\frac{\partial G_{-}}{\partial n}\right)ds. \tag{2.29}$$

By eliminating the term dependant on $\partial U/\partial n$ on S_1, the Kirchhoff boundary conditions need only be applied only to the field U and not to its normal derivative, therefore removing the internal inconsistency. Equation (2.29) is known as the *first Rayleigh-Sommerfeld solution*.

Expanding equation (2.29) by substituting in the algebraic form of the normal derivative of Sommerfeld's first Green's function yields

$$\frac{\delta G_{-}(P_1)}{\delta n} = \cos(\vec{n},\vec{r}_{01})\left(ik - \frac{1}{r_{01}}\right)\frac{\exp(ikr_{01})}{r_{01}} - \cos(\vec{n},\vec{\tilde{r}}_{01})\left(ik - \frac{1}{\tilde{r}_{01}}\right)\frac{\exp(ik\tilde{r}_{01})}{\tilde{r}_{01}}.$$

The following are true for P_1 on S_1

$$r_{01} = \tilde{r}_{01}$$

$$\cos(\vec{n},\vec{r}_{01}) = \cos(\vec{n},\vec{\tilde{r}}_{01})$$

and it is possible to write:

$$\frac{\delta G_{-}(P_1)}{\delta n} = 2\cos(\vec{n}, \vec{r}_{01})\left(ik - \frac{1}{r_{01}}\right)\frac{\exp(ikr_{01})}{r_{01}}.$$

Assuming that $k \gg 1/r_{01}$ (i.e. $r_{01} \gg \lambda$), the term $1/r_{01}$ disappears, leaving

$$\frac{\delta G_{-}(P_1)}{\delta n} = 2ik\cos(\vec{n}, \vec{r}_{01})\frac{\exp(ikr_{01})}{r_{01}}.$$

Notice that the result is simply twice the normal derivative of the free-space Green's function (equation (2.14)) used by Kirchhoff to arrive at his equation, i.e.

$$\frac{\delta G_{-}(P_1)}{\delta n} = 2\frac{\delta G(P_1)}{\delta n}.$$

This relationship allows the first Rayleigh-Sommerfeld solution to be written in terms of the free-space Green's function

$$U_I(P_0) = -\frac{1}{2\pi}\iint_{\Sigma}\left(U\frac{\partial G}{\partial n}\right)ds. \tag{2.30}$$

Another valid Green's function could be constructed by allowing the two point sources to oscillate in phase, and could be written

$$G_{+}(P_1) = \frac{\exp(ikr_{01})}{r_{01}} + \frac{\exp(ik\tilde{r}_{01})}{\tilde{r}_{01}}. \tag{2.31}$$

This time, rather than the Green's function itself disappearing over the whole of S_1, its normal derivative disappears. Recall from earlier that

$$\frac{\delta}{\delta n}\left(\frac{\exp(ikr_{01})}{r_{01}}\right) = \cos(\vec{n}, \vec{r}_{01})\left(ik - \frac{1}{r_{01}}\right)\frac{\exp(ikr_{01})}{r_{01}}$$

and on S_1,

$$r_{01} = \tilde{r}_{01}$$

$$\cos(\vec{n}, \vec{r}_{01}) = \cos(\vec{n}, \vec{\tilde{r}}_{01})$$

therefore,

$$\frac{\delta G_+(P_1)}{\delta n} = \cos(\vec{n},\vec{r}_{01})\left(ik - \frac{1}{r_{01}}\right)\frac{\exp(ikr_{01})}{r_{01}} - \cos(\vec{n},\vec{r}_{01})\left(ik - \frac{1}{r_{01}}\right)\frac{\exp(ikr_{01})}{r_{01}} = 0. \quad (2.32)$$

By substituting result this into equation (2.26), and imposing a Kirchhoff boundary condition only on the normal derivative of the field, the *second Rayleigh-Sommerfeld solution* is obtained

$$U(P_0) = \frac{1}{4\pi}\iint_{\Sigma}\left(\frac{\partial U}{\partial n}G_+\right)ds. \quad (2.33)$$

Since on the aperture, Σ, $G_+ = 2G$ it is possible to write the second Rayleigh-Sommerfeld solution in terms of the free-space Green's function used by Kirchhoff

$$U_{II}(P_0) = -\frac{1}{2\pi}\iint_{\Sigma}\left(\frac{\partial U}{\partial n}G\right)ds. \quad (2.34)$$

2.3.2.3 The Rayleigh-Sommerfeld diffraction formula

The diffraction formula I will make most use of in this work is the Rayleigh-Sommerfeld diffraction formula. It is constructed by substituting the Green's function G_- (equation (2.28)) into Kirchhoff's diffraction integral (equation (2.26))

$$U(P_0) = \frac{1}{i\lambda}\iint_{\Sigma} U(P_1)\frac{\exp(ikr_{01})}{r_{01}}\cos\theta\, ds, \quad (2.35)$$

where, λ is the wavelength of the monochromatic radiation, $k = 2\pi/\lambda$ and $\cos\theta$ is the cosine of the angle between the outward normal of the aperture Σ and the vector pointing from P_0 to P_1. In order to arrive at this equation, one must:

1. Assumed that the field is – or at least can be treated as – a monochromatic scalar wave (section 2.3.2.4) which is a solution to the scalar Helmholtz equation.
2. Assumed that the Sommerfeld radiation condition is satisfied.

3. Applied Kirchhoff's boundary conditions – only to the field U and not to its normal derivative so there is no internal inconsistency.
4. Assumed that $r_{01} \gg \lambda$.

The Rayleigh-Sommerfeld diffraction formula can be put into the context of the Huygens-Fresnel principle by viewing the field at the observation point P_0 as being calculated by the superposition of spherical wavelets ($\exp(ikr_{01})/r_{01}$) emanating from every point on the wave front U at the aperture Σ.

The factor $1/i\lambda$ indicates that the wavelets have a phase leading that of the original wave front by 90° and an amplitude scaled by the reciprocal of the wavelength. These modifications to the relative amplitude and phases of the secondary wavelets are the same as those arbitrarily imposed by Fresnel in order to make his analysis work for a propagating plane wave.[6]

The factor, $\cos\theta$, known as an obliquity factor, modifies the directivity of the secondary sources and has no simple connection to the Huygens-Fresnel principle. It is important to note, that diffraction effects arise from interactions between the incident wave and the material on the rim of the aperture and the Huygens-Fresnel principle should be viewed as a useful construct from which to predict outcomes of diffraction, rather than being the real physical mechanism.[12]

2.3.2.4 The Scalar Wave Approximation

We have followed the construction of equations that predict the diffraction of light, always on the basis that we can assume the optical fields concerned are scalar. In reality, light can only be fully described by an oscillating function with a vector amplitude – polarisation. Assuming that the amplitude of light waves is scalar can, at best, only perfectly describe the behaviour of a single plane-polarised component of a wave.

If diffraction is observed several wavelengths from an aperture which is much greater than a wavelength in size and, if diffraction occurs in a medium which fits certain criteria, the scalar approximation is adequate. In the microwave region of the spectrum

predictions made using the scalar approximation have been proven to match reality closely.[6,13]

The criteria specify that the medium must have optical properties that are the same for all polarisations of light (isotropic), the refractive index must also be uniform with respect to position (homogeneous), for the wavelength range of the propagating wave the refractive index must not depend on wavelength (nondispersive) and it must have a magnetic permeability equal to the vacuum permeability (nonmagnetic). In the work described in this thesis, scalar diffraction theory is used to model propagation of monochromatic light in air, glass and water; in these situations the criteria are satisfied.

2.4 References

1 E. Hecht, *Optics*, Addison-Wesley, 2nd edn., 1987.

2 O. Svelto, *Principles of Lasers*, Springer, 5th edn., 2010.

3 J. Pawley, *Handbook of Biological Confocal Microscopy*, Springer, 3rd edn., 2010.

4 O. Darrigol, *A History of Optics from Greek Antiquity to the Nineteenth Century*, Oxford University Press, 2012.

5 T. Young, *Phil. Trans. Roy. Soc.*, 1802, 92, 26

6 J. W. Goodman, *Introduction to Fourier Optics*, Roberts & Company, Colorado, 3rd edn., 2005.

7 D. Gabor, Nature, 1948, 161, 777-778.

8 D. Gabor, *Nobel Prize Lecture*, 1972.

9 E. N. Leith, J. Upatnieks, *J. Opt. Soc. Am.*,1962, 52(10), 1123-1128.

10 C. S. Vikram, *Particle Field Holography*, Cambridge University Press, 1992.

11 A. Sommerfeld, *Jahresber. Deut. Math. Ver.*, 21(309), 1912.

12 M. Born and E. Wolf, *Principles of Optics*, Pergamon Press, 6th edn., 1980.

13 S. Silver, *J. Opt. Soc. Am.*, 52(131), 1962

14 Michael W. Davidson's Optical Microscopy Primer, http://micro.magnet.fsu.edu/primer/lightandcolor/diffractionintro.html, (accessed September 2014)

3 Design of the Holographic Microscope

The method for velocimetry inside micro-scale curved samples, described in this thesis, consists of several stages:

- record a pair of holograms a short time apart,
- refocus holograms numerically to the plane of the sample and detect the edge,
- use the information about the shape of the edge in a plane to find the surface in 3D,
- calculate the values of the electric field on the surface and use this information to propagate the light inside,
- apply particle velocimetry algorithms to estimate the flow inside the sample.

The criteria for the first stage were to design a simple holographic microscope, capable of recording images of an ink-jet stream. This is achieved with a forward-scatter, lensless off-axis digital holographic microscope. It is important that the original holograms are as free from noise as possible as because of the amount of post-processing required to propagate the light back through the curved air-liquid interface of the jet. The ink-jet streams specifically targeted by this work are continuous ink-jets with an unperturbed diameter of ~100 μm. Close to breakup, the swells in such a stream reach diameters of up to ~250 μm. Although the experiments in this thesis focus on the 100 μm jet, the aim is to develop a system capable of use on any curved sample of a similar scale, for example micro-capillaries or drop-on-demand ink jets. The remainder of this chapter describes and justifies the design of the holographic microscope assembled and used in this work.

3.1 The Behaviour of Light in a Cylindrical Sample

In holographic PIV, particles in a flow are illuminated by coherent light and it is the light that is scattered by these particles that makes up the signal. The first stage in the development of a holographic microscope was to investigate the bulk behaviour of light

inside a curved sample, to assess the proportion of seeding particles illuminated in the simplest case of a cylindrical jet. Figure 3.1 shows ray-tracing of a plane wave through a 100 μm diameter circular cross-section with the same refractive index as water ($n = 1.33$).

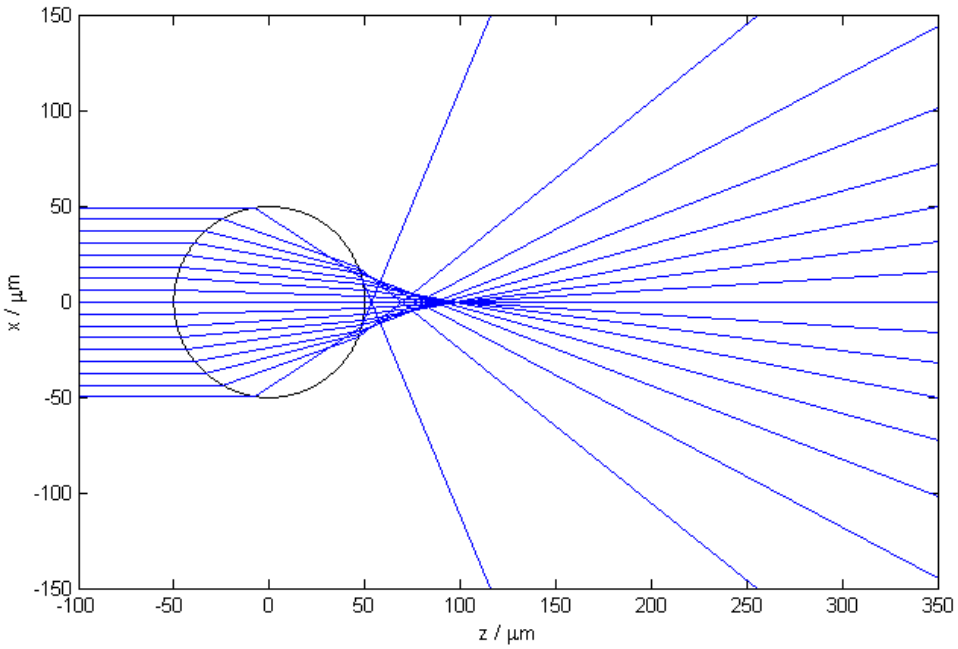

Figure 3.1 Ray tracing through a disk with refractive index 1.33, illuminated by a plane wave from the left. Calculated using my own MATLAB code.

As shown, due to refraction at the back surface, not all of the inside of a cylindrical sample can be illuminated (figure 3.1); any vectors subsequently extracted from the dark area must be rejected as erroneous. The result, however, does not mean that there is insufficient data as enough of the interior is illuminated to allow construction of a complete map by invoking an axisymmetric approximation.

The ray tracing highlighted another key issue with imaging inside curved streams. The lensing effect of a curved stream focuses collimated light close to the front surface which subsequently diverges with a high numerical aperture. If the sample is illuminated with a diverging wave, however, the transmitted light is focussed farther away from the front surface and does not diverge with such a high numerical aperture, consequently more transmitted light can reach the collection optics/detector. Figure

3.2(a) and (b) show ray tracing through a cylindrical cross-section, with collimated and divergent illumination respectively; in both cases, the range of light collected is limited by the same collection system. Although the divergent rays do not illuminate more of the inside of the sample, 60 % more light over the cross-sectional area reaches the detector for the case shown. Diverging illumination was used in the new microscope for this reason.

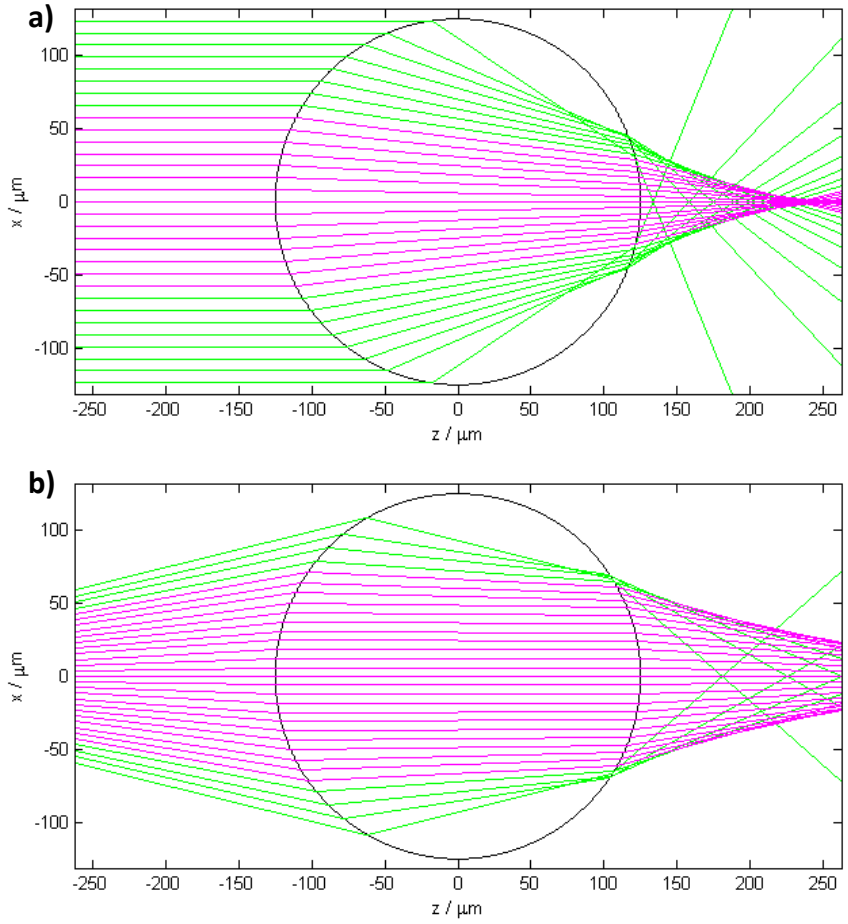

Figure 3.2 Ray tracing through a circular cross section of refractive index 1.33, showing the rays collected by a 15.2 mm detector placed at $\boldsymbol{z} = 27$ mm, for (a) collimated illumination and (b) diverging illumination. The diverging rays emanate from a point $\boldsymbol{z} = -500$ µm. Rays were traced using custom MATLAB code.

3.2 The Basic Microscope

There are several types of holographic microscope: the microscope can be designed to record in-line or off-axis holograms, in either a lensed or a lensless arrangement. The lensless arrangement has the greater benefits in this work; the expanding-wave illumination provides the maximum illuminated volume in a curved sample and the simpler optical system makes the microscope more robust.

A generic in-line lensless microscope is shown in figure 3.3a – the arrangement is known as lensless as there are no optics between the sample and the detector. The drawback of this system is that in-line holograms are intrinsically noisy due to the overlap of multiple diffracted orders with the real image. Since the holograms will be post-processed in order to propagate the reconstructed scattered wave back through the curved surface of the sample, it is sensible to record holograms with the least possible noise. For this reason I opted for off-axis recording and adapted the simple lensless holographic microscope design to include a separate reference beam, figure 3.3b. The resulting system is similar to a lensless Fourier transform holographic setup.[1]

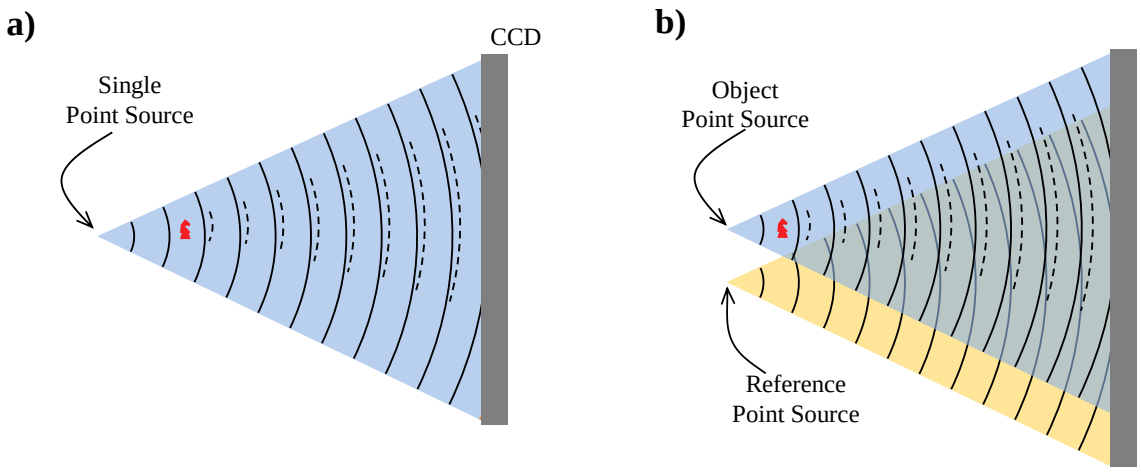

Figure 3.3 a) A point-source in-line holographic microscope. b) A point source off-axis holographic microscope.

3.2.1 An Aside on Measurement Direction

Although a forward-scatter measurement direction was implemented in this work, in early designs I considered both back-scatter and side-scatter approaches. The back-scatter approach was rejected because of the necessity of illuminating from the same direction as the camera, introducing at least two optical interfaces between the sample and the recording medium. Any imperfection in these interfaces would affect the quality of the subsequently recorded data. Although a side-scatter arrangement would allow the particles to be imaged without any background light, increasing contrast and making detection easier, two problems are introduced. Firstly, recording a side-scatter hologram does not give the shadowgraph image of the jet that forward-scatter would, introducing a requirement for a second camera to record the shape of the sample. The shape of the sample must be known so that the reconstructed wave can be propagated back through it. The second, and fatal, problem is due to the inefficient scattering at 90°. To compensate for this, the illumination beam must be much more intense. Much of the light from this more intense illumination beam (with very high peak power due to its pulsed nature) will be reflected by the surface, saturating part of the camera's sensor and presenting a risk of damage to it.

For the reasons above, a forward-scatter arrangement for the holographic microscope was implemented in this work.

3.2.2 Lensed or Lensless Design

The numerical methods used to recover the field inside the sample do not restrict the type of holographic microscope used; as long as quality of the data is sufficient to provide a good estimate of the electric field around the sample. Both lensed and lensless systems were considered. A lensless design was eventually chosen as it requires a single objective lens. The single objective is shared by the both the illumination and reference beams, giving three advantages: (1) the system is more compact, (2) it is easier to align as the curvature of the reference and object waves are intrinsically matched and (3) it is

easier to maintain, having fewer optics and therefore fewer surfaces to keep clean, especially in an environment where occasional splashes of fluid are expected. There is also a consideration of cost, at the time of writing, a matching objective lens for our system is listed at £1460.[2]

The lensless arrangement, however, does require slightly more numerical work in order to propagate the field on the detector to the sample tens of millimeters away; whereas a hologram from a lensed system could be recorded so that it is effectively in the plane of the sample. This added processing step was not a source of great concern given that a fast computer with sufficient RAM to handle the large 3D datasets, inevitable in the reconstruction of the internal fields of ink-jet samples, was required anyway.

3.3 Design Considerations

The basic design, described previously could be achieved using the optical setup shown in figure 3.4. The single beamsplitter (BS) splits the laser beam into two parts; the object beam and the reference beam. The object beam is normally incident on the exit pupil at the back of the objective (OBJ) and forms the object point source at the working distance of the objective, while the reference beam is directed by mirrors (M1 and M2) into the exit pupil of the objective at a small angle to normal. The result is two spatially-separated point-sources; the spacing between them can be controlled by changing the angle of the reference beam using the mirrors. The distance between the camera and the point sources can be easily changed using a translation stage. The prism acts as a fixed delay between the illumination and reference arms, to compensate for the longer path of the reference arm. With the prism, the optical path length of beams is closely matched and good contrast in the interference fringes is achieved.

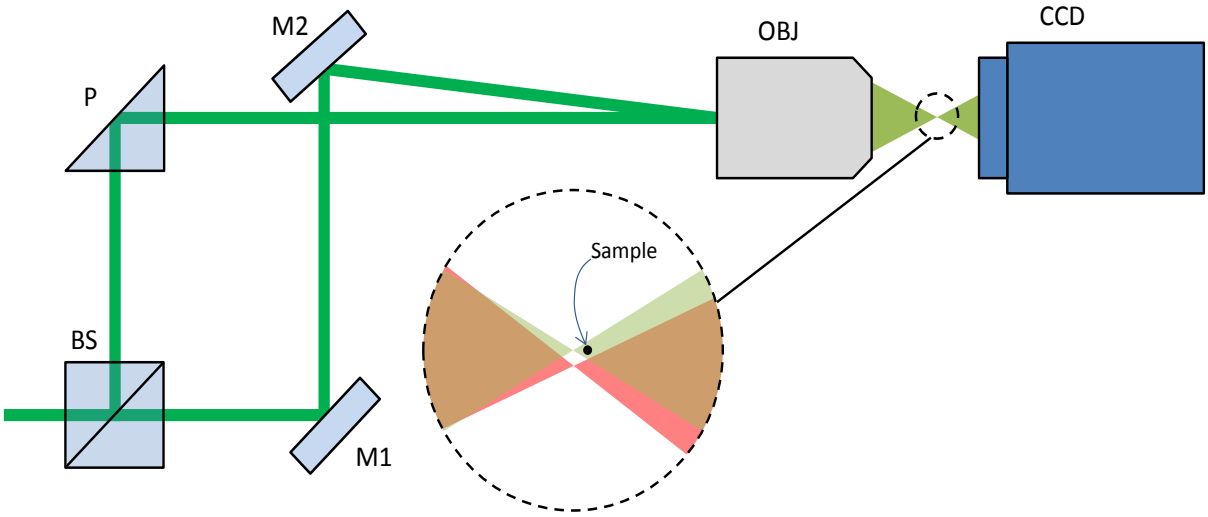

Figure 3.4 Schematic of the basic optical rig.

The two key design considerations for this microscope are: (1) there must be room for the largest sample to fit in the object beam without eclipsing the reference beam and (2) interference between the object and reference beams must be recorded without aliasing. Three parameters can be altered to achieve the desired results: (1) the distance between the two point sources, (2) the distance between the plane of the point sources and the detector, and (3) the distance between the sample and the plane of the point sources. Subsections 3.3.1 through 3.3.6 address the design considerations and derive limits for the three parameters s, D and d (defined in figure 3.5). Where key equations are given, example numerical figures, based on the hardware (light source, objective lens and camera) of the current working microscope, are provided to give the reader an idea of scale. The properties of the example hardware are given in table 3.1.

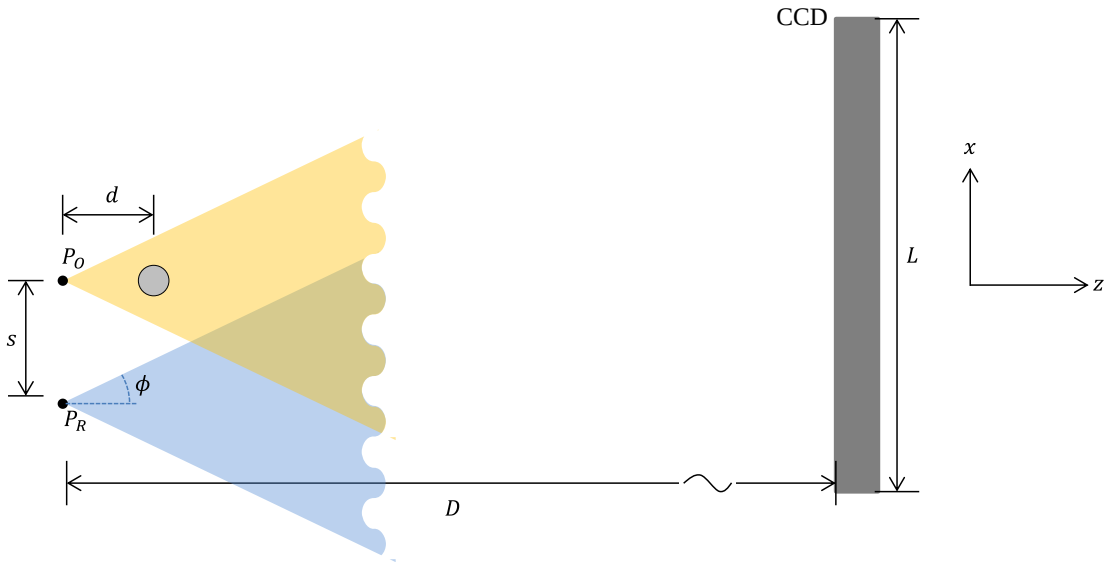

Figure 3.5 The geometry around the sample region. Relative distances have been exaggerated for clarity.

Table 3.1 Physical properties of an example holographic microscope.

Property	Symbol	Value
Detector dimension	L	15.2 mm
Pixel pitch	Δ	7.4 μm
Objective numerical aperture	NA	0.42
Illumination wavelength	λ	532 nm

3.3.1 The Recording Distance (D)

For effective use of the camera, its sensor must be filled with the interference pattern between the two beams; this is controlled by the recording distance, D (figure 3.5). An expression for the minimum distance, $D_{\min}$, where the sensor is completely filled can be derived using simple trigonometry, and is written:

$$D_{\min} = \frac{(L + 2s)\sqrt{2}}{2\tan\phi}, \tag{3.1}$$

where, L is the full width of the sensor and ϕ is the half angle of the divergence of the object wave (the inverse sine of the numerical aperture (NA) of the objective lens). Assuming that s, the distance between the sources, is approximately 1 mm, for the example system summarised in table 3.1, $D_{\min} \approx 27$ mm. $D_{\min}$ is the closest that the camera can be to the point sources while still filling the sensor. Increasing D increases the maximum field of view, but reduces the effective numerical aperture of the hologram thereby reducing resolution in the recovered particle images.

3.3.2 The Field of View and Sample Distance

The field of view of this microscope is approximately the area of intersection between a plane parallel to the detector at a distance d away from the object point source (P_O) and a square based pyramid with its apexes at P_O and the four corners of the detector. By comparison of similar triangles, the ratio of the field of view to the sample distance, d, can be written in terms of the recording distance D and the detector size L:

$$\frac{2r}{d} = \frac{L}{D} \tag{3.2}$$

where, r is the half width of the square field of view. This ratio is useful in reducing the number of unknowns in the following equations that consider the ideal spectrum of the hologram. In the case of the example system the ratio is 0.56.

3.3.3 Consideration of the Hologram Spectrum

As discussed in Chapter 2, a hologram can be written symbolically as:

$$I(x,y) = |R+O|^2 = |R|^2 + |O|^2 + R^*O + RO^*. \tag{3.3}$$

where, O is the object wave and R the reference wave. In an ideal off-axis hologram, the various reconstructed waves are separated in space, meaning that the real image can be viewed without influence from the other reconstructed waves. Similarly, in the Fourier spectrum of an ideal off-axis hologram the spectra of the individual parts are separate; allowing the necessary term to be extracted without any influence from the others. The spectrum of an ideal hologram is shown in figure 3.6. The spatial frequency domain extends from $-f_{\max}$ to $+f_{\max}$ in both the f_x and f_y directions, where, $f_{\max} = 1/2\Delta$; Δ being the pixel pitch of the recording device. The central band is composed of the spectra of the self-interference terms ($|R|^2$ and $|O|^2$) and the other two bands are the spectra of the cross-terms (R^*O and RO^*). The best use of the information storage capacity of the hologram is to ensure that the cross terms are as large as possible, within the limits that they should not overlap with the self-interference terms and do not contain any spatial frequencies larger than $f_{\max}$. To a good approximation, the bandwidths of the self-interference and cross-term bands are equal, i.e. $\omega_{\text{self}} \approx \omega_{\text{cross}}$. This is contrary to the familiar case in digital holography where holograms are recorded with a plane wave serving as a reference; in these cases, $\omega_{\text{self}} \approx 2\omega_{\text{cross}}$. They are approximately equal, in the holographic microscope described here because the reference source is approximately in the same plane as the object. By inspection of figure 3.6, and simple geometry, it is possible to estimate a limiting value for ω_{self}:

$$\omega_{\text{self}} = \frac{f_{\max}}{1+\sqrt{2}}. \tag{3.4}$$

For the example system, with a pixel size Δ = 7.4 μm, ω_{self}= 2.8×10^4 m^{-1}. In order to relate the bandwidth of the self-interference term to the size and position of the sample, it is useful to revisit equation (3.3), taking into account that the object wave is in fact made up of the sum of waves scattered from every point on the sample. This analysis is given in the next subsection.

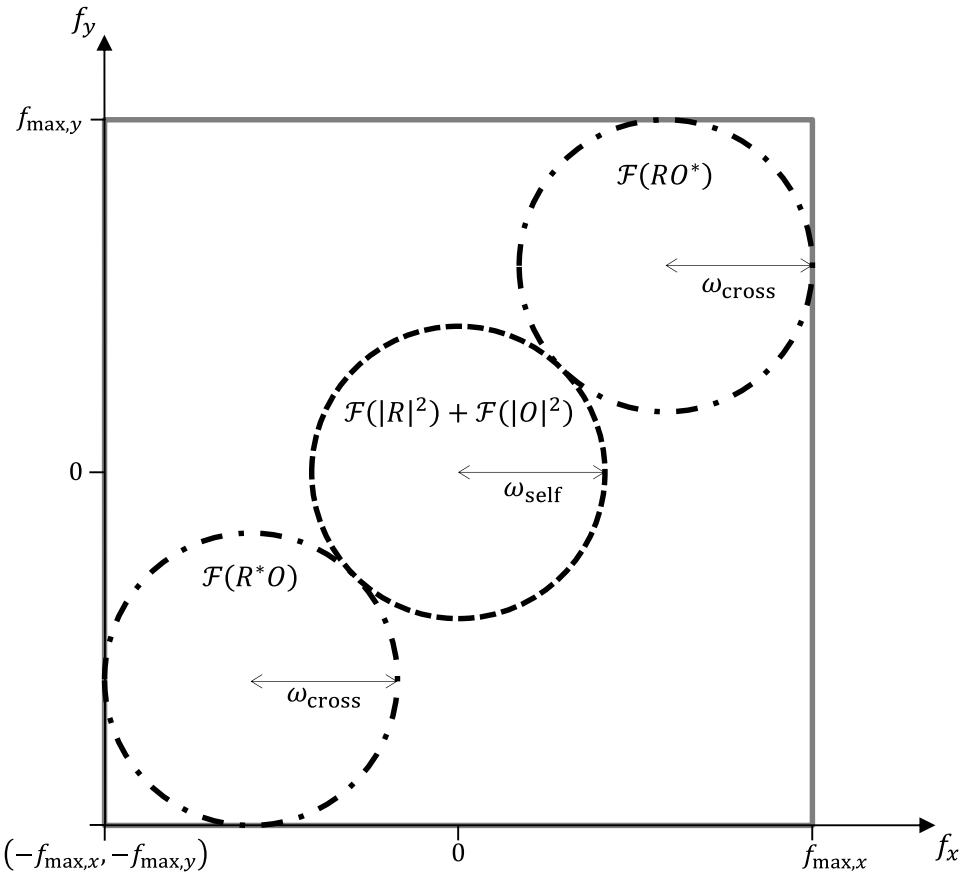

Figure 3.6 The ideal hologram spectrum for the microscope discussed.

3.3.4 Frequencies Present in the Hologram

The size of the sample affects the frequencies of the interferences in the hologram. If any interferences vary faster than the maximum resolvable spatial frequency, $f_{\max}$, the hologram will be aliased and contain spurious frequency information. In this subsection, the derivation of an equation that predicts the maximum diameter of the field of view based on the maximum bandwidths allowable in the spatial frequency domain will be discussed.

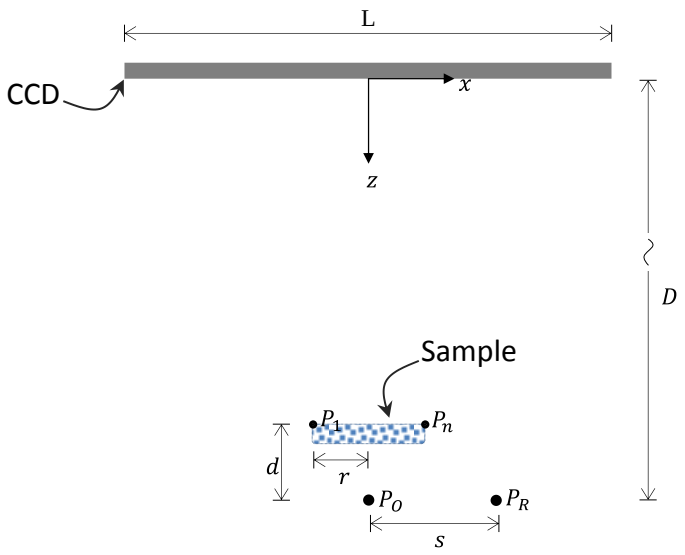

Figure 3.7 Schematic of the quantities required to calculate the spatial frequencies present in the hologram.

Consider the geometry shown in figure 3.7. A sample with half-width, r, is placed a perpendicular distance $(D - d)$ away from the centre of a finitely-sampled planar detector. The light scattered from the sample interferes with a spherical reference wave emanating from P_R. The point P_R is a distance of D away from the detector along the z-axis and a distance of s away from the centre of the detector along the x-axis. The object wave consists of the sum of waves scattered from every point on the sample. The hologram is formed by the interference of the object wave with the reference and, by using a similar notation to equation (3.3), the recorded intensity could be written:

$$I(x,y) = \left| R + \sum_{j=1}^{n} O_j \right|^2 , \tag{3.5}$$

where each wave O_j emanates from a different point on the object. Just like in equation (3.3), the modulus squared of the sum can be expanded, giving two types of terms: the unmodulated self-interference terms:

$$|R|^2 + \sum_{j=1}^{n} \sum_{k=1}^{n} O_j O_k^* \tag{3.6}$$

and the cross-terms:

$$\sum_{j=1}^{n} RO_j^* + \sum_{j=1}^{n} R^* O_j. \tag{3.7}$$

Equation (3.4) gives the ideal relationship between the maximum resolvable spatial frequency $f_{\max}$ and the maximum spatial frequency in the self-interference band ω_{self}. By analysing the components of the self-interference term, it is possible to approximate an expression for ω_{self} in terms of the sample size. The fastest-varying part of the self-interference term is the interference between the two sources on the extremes of the sample (P_1 and P_n). The interference terms can be written:

$$\begin{aligned} O_1 O_n^* &= e^{i\frac{2\pi}{\lambda}|\boldsymbol{P_1}-x|} e^{-i\frac{2\pi}{\lambda}|\boldsymbol{P_n}-x|} \\ O_1^* O_n &= e^{-i\frac{2\pi}{\lambda}|\boldsymbol{P_1}-x|} e^{i\frac{2\pi}{\lambda}|\boldsymbol{P_n}-x|}. \end{aligned} \tag{3.8}$$

The two interference terms above only differ in the sign of the phase, it is therefore sufficient to consider only one of them. By substituting the positions from figure 3.7, the interference can be written:

$$O_1 O_n^* = \exp\left\{ i \frac{2\pi}{\lambda} \left(\sqrt{(x+r)^2 + (D-d)^2} - \sqrt{(x-r)^2 + (D-d)^2} \right) \right\}. \tag{3.9}$$

The frequency of $O_1 O_n^*$ is proportional to the rate of change of the variable part of the exponent with respect to x and can be written:

$$\begin{aligned} &\frac{1}{\lambda} \frac{\partial}{\partial x} \left(\sqrt{(x+r)^2 + (D-d)^2} - \sqrt{(x-r)^2 + (D-d)^2} \right) \\ &= \frac{1}{\lambda} \left[\frac{x+r}{\sqrt{(x+r)^2 + (D-d)^2}} - \frac{x-r}{\sqrt{(x-r)^2 + (D-d)^2}} \right]. \end{aligned} \tag{3.10}$$

Figure 3.8 is a plot of frequency versus position on the detector, for reasonable values of r, d and D, showing that the frequency of $O_1 O_n^*$ reaches a maximum at x=0, i.e. the centre of the detector. The maximum frequency of the self-interference band, ω_{self}, is therefore:

$$\omega_{\text{self}} = \frac{1}{\lambda} \left[\frac{2r}{\sqrt{r^2 + (D-d)^2}} \right]. \tag{3.11}$$

Making a paraxial approximation, justified because r is small compared to $(D - d)$, equation (3.11) can be simplified to:

$$\omega_{\text{self}} = \frac{2r}{\lambda(D-d)}. \tag{3.12}$$

By combining equations (3.2), (3.4) and (3.12) an expression for the maximum imagable value of r in terms of the wavelength of illumination, detector size, pixel pitch and recording distance can be written:

$$2r_{\max} = \frac{\lambda DL\left(\sqrt{2}-1\right)}{\sqrt{2}\lambda D - \lambda D + 2L\Delta} \tag{3.13}$$

where $2r_{\max}$ is the full width of the field of view. For the example system, the maximum field of view, $2r_{\max}$, is 385 μm with a corresponding maximum sample distance, $d_{\max}$, of 686 μm.

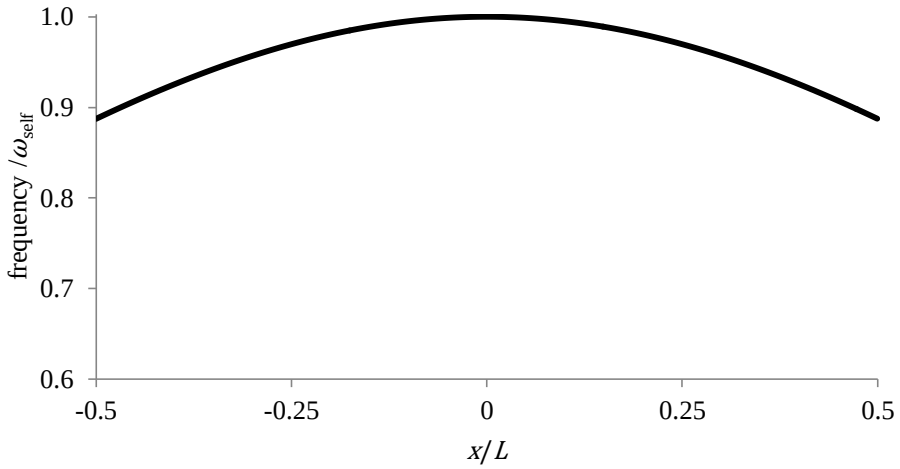

Figure 3.8 The frequency of the most rapidly-varying part of the self-interference with position across the detector.

3.3.5 The Source Separation (s)

The cross terms are made up of the sum of the interferences between waves emanating from every point on the sample and the reference wave. The position of the reference source relative to the sample changes the position of the spectra of the cross terms within the spatial frequency domain. It is important that the maximum frequency of the cross term is less than $f_{\max}$ or the recorded hologram is aliased and will contain spurious frequency information.

Using a similar method to the previous subsection, an expression for the ideal source separation, s, is derived by considering the most rapidly varying interference in the cross terms. The most rapidly varying interference is between the reference source (P_R) and the wave scattered by the point on the sample furthest away from it (P_1) (figure 3.7). Again, the interferences between these points can be written:

$$\begin{aligned} RO_1^* &= e^{i\frac{2\pi}{\lambda}|\boldsymbol{P_R}-x|}e^{-i\frac{2\pi}{\lambda}|\boldsymbol{P_1}-x|} \\ R^*O_1 &= e^{-i\frac{2\pi}{\lambda}|\boldsymbol{P_R}-x|}e^{i\frac{2\pi}{\lambda}|\boldsymbol{P_1}-x|} \end{aligned} \tag{3.14}$$

Substituting in the parameters from figure 3.7, one of the terms can be written:

$$R^*O_1 = \exp\left\{i\frac{2\pi}{\lambda}\left(\sqrt{(x+r)^2+(D-d)^2}-\sqrt{(x-s)^2+D^2}\right)\right\}, \tag{3.15}$$

and its frequency is:

$$\frac{1}{\lambda}\left[\frac{x+r}{\sqrt{(x+r)^2+(D-d)^2}}-\frac{x-s}{\sqrt{(x-s)^2+D^2}}\right]. \tag{3.16}$$

A plot of the frequency of R^*O_1 against position on the detector (figure 3.9) shows that, for a realistic alignment, frequency is highest at close to the right-hand edge of the detector. An expression approximating the maximum frequency of the cross term, $f_{\mathrm{cross-max}}$, can therefore be written by substituting x=L/2 into equation (3.8):

$$f_{\text{cross-max}} = \frac{1}{\lambda}\left[\frac{\frac{L}{2}+r}{\sqrt{\left(\frac{L}{2}+r\right)^2+(D-d)^2}} - \frac{\frac{L}{2}-s}{\sqrt{\left(\frac{L}{2}-s\right)^2+D^2}}\right]. \tag{3.17}$$

By setting $f_{\text{cross-max}} = f_{\text{max}}$, the equation can be solved to find s given that all the other constants are known. In the case of the example system, the sources should be separated by approximately 669 μm. Considering the geometry of the system, as long as s is greater than $2r$, the sample will not encroach on the reference beam and the microscope is viable; although I have not found a case, realistic or otherwise, where an unviable s has been predicted.

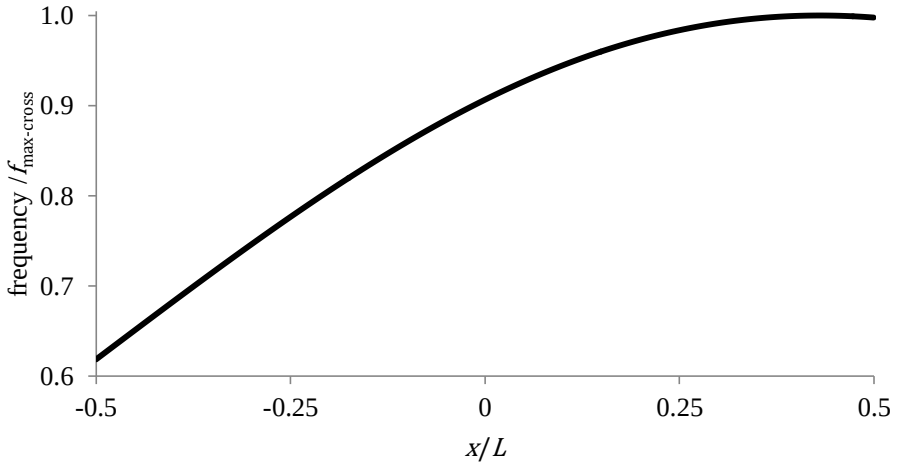

Figure 3.9 The frequency of the fastest-varying part of the cross term against position on the detector.

3.3.6 The Effective Numerical Aperture of the Hologram (Ω)

The property that defines how well objects can be resolved in the reconstructed images is the effective numerical aperture (Ω) of the hologram. It is approximately the sine of the half angle subtended between the sample and the edges of the detector. It can be written:

$$\Omega = \sin\left[\tan^{-1}\left(\frac{L}{2(D-d)}\right)\right], \tag{3.18}$$

where L is the full width of the detector. The maximum Ω is when the sample is as close as possible to the detector, i.e. $D = D_{\min}$ and $d = d_{\max}$. For the example system, $\Omega = 0.28$. The effective numerical aperture is related to the transverse and axial resolutions by equations (1.1) and (1.2) respectively (on page 33). Although the effective numerical aperture is better maximised, it is largely dictated by other considerations.

3.3.7 Conclusions on the Design Considerations

The equations provided in sub-sections 3.3.1 through 3.3.6 allow important capabilities of the microscope, such as maximum sample size and effective numerical aperture as well as alignment parameters to be estimated for a given set of hardware. Although a number of approximations have been applied, the resultant equations show that the planned microscope is feasible in principle for commonly available components, as well as providing a useful guide for the optimum alignment. The next section will focus upon the hardware and design of the current working version of the microscope.

3.4 The Final Design of the Microscope

The main purpose of the microscope is to record holograms for use in holographic PIV analysis. This means that it must not only be created with a focus on recording good quality holograms, it must also be capable of capturing two holograms in quick succession with short exposure times. The brief for the system was to measure flows in micron-scale ink jets flowing at speeds of around 5 m/s; it is the speed of the flow that places the strictest requirements on the hardware used – specifically the camera and light source. Exposure times must be less than around 25 ns in order to freeze particle images to less than a quarter of a wavelength – so that they appear as points rather than streaks. The inter-frame time (Dt) must be in the order of hundreds of nanoseconds so that the particles only move a few microns between exposures.

For the purposes of this work a commercial PIV system was purchased and the specialised light source and camera supplied with it used for the experiments. The system chosen was the LaVision Flowmaster μPIV system. The light source is a dual-head pulsed Nd:YAG laser (Litron NANO-S-35-15 PIV). The dual-head design has two separate lasers, one providing the illumination for the first frame and one providing the illumination for the second frame. Two separate lasers allow the inter-frame time to be varied continuously with no lower limit. The lasers are capable of delivering 4 ns pulses with a wavelength of 532 nm. The camera supplied is a 4 Megapixel interline-transfer CCD (ImagerProX 4M). The square sensor has pixels with a 7.4 μm pitch and is capable of recording two frames with a minimum separation of 120 ns. The timing and synchronisation of the laser pulses and the camera was achieved using hardware supplied as part of the LaVision Flowmaster PIV system along with their DaVis software package (DaVis 8.0). The hardware and software were able to respond to external trigger signals, allowing the recording to be synchronised to the ink-jets. The DaVis package was also used to capture the images from the camera. The images were saved in a lossless format for later processing. During alignment, images were recorded and their Fourier spectra were reviewed to ensure that the ideal alignment described in the previous section was achieved, that is, as much information as possible was being recorded and the images were free from aliasing.

The lens used was a long working distance 0.42 NA 20× objective (Edmund Optics 20× M Plan Apo LWD). The long working distance (25 mm) makes the design less congested, allowing greater distances between the lens and the camera. Although higher NA long working distance lenses are available, the 0.42 NA option was cost-effective as well as allowing for samples up to 385 μm in diameter to be imaged with an effective NA of 0.28. The transverse and axial resolutions of the microscope are approximately 1.9 μm and 6.7 μm respectively. Potentially the axial resolution could be better than predicted by taking advantage of the access to the complex amplitude of the real particle images as mentioned in section 1.2.4.

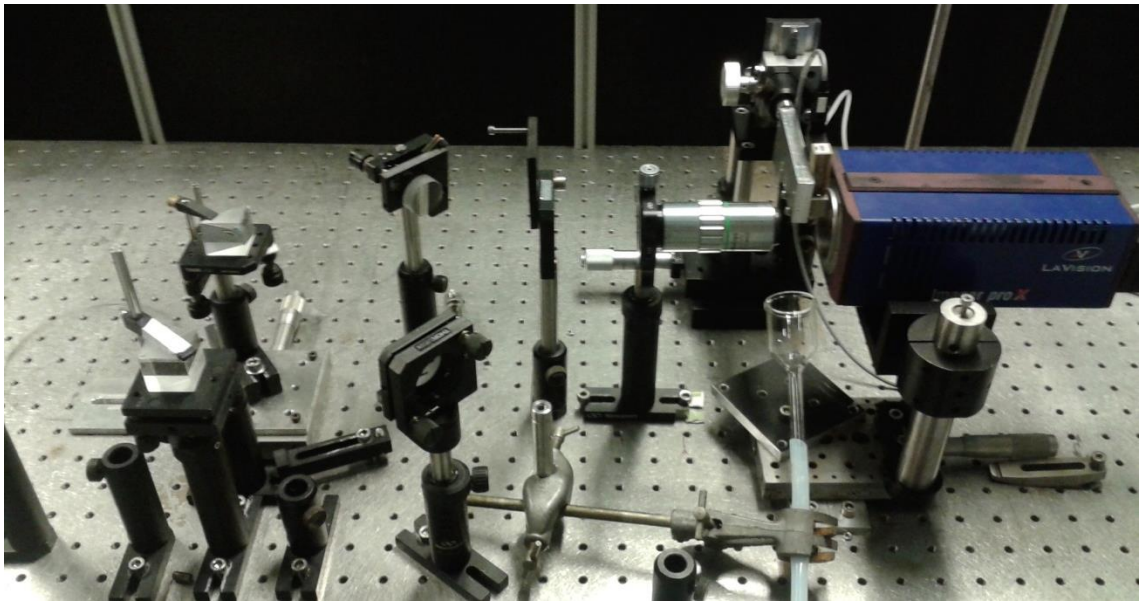

Figure 3.10 The finalised optical rig.

The finalised rig is shown in figure 3.10. The beam from the laser is first spatially filtered by focussing it through a 25 μm pinhole with a +125 mm lens (CVI). The central spot of the resulting Airy pattern is collimated by a +154 mm lens (CVI) to give a beam with a diameter of 8 mm and passed through an iris which blocks the other maxima of the Airy pattern. The beam is then split with a 1" 50:50 non-polarising beamsplitter cube to form the reference and object beams. The reference beam is directed through the objective lens at a small angle, adjustable using the two mirrors M1 and M2 (Newport) mounted on kinematic mounts (Thorlabs). The object arm is directed onto the back of the objective lens by the 25 mm right-angled prism P1. The prism acts as a fixed delay to compensate for the fact that the reference beam path is slightly longer than the object beam path. The object beam passes through the objective exactly normal to the entrance pupil so that it suffers no astigmatism. The camera is mounted on a translation stage (Newport) controlled by a micrometer with a long (40 mm) travel allowing its position to be accurately set over a long range. The camera is positioned so that the centre of the CCD chip is exactly in line with the object point source and is care is taken to make sure that it is as close as possible to parallel with the nose of the objective lens. The camera is connected to a PC with 12 GB RAM, to facilitate the holographic reconstructions which, because of their volumetric nature involve manipulation of very large arrays.

The +125 mm and +154 mm lenses are planoconvex singlets with a broadband visible antireflective coating and a surface flatness of $\lambda/4$. The mirrors M1 and M2 have a high surface flatness ($\lambda/20$) and a high surface quality (scratch-dig of 10-5).

The next chapter will describe how the holograms recorded with this microscope are numerically reconstructed, first to produce a shadowgraph image of the sample and then to reconstruct the field inside the sample free from any distortions due to the curved air-medium interface.

3.5 References

1 H. J. Caulfield, *Handbook of Optical Holography*, Academic Press Inc. London, 1979.

2 Edmund Optics, http://www.edmundoptics.co.uk/microscopy/infinity-corrected-objectives/eo-infinity-corrected-long-working-distance-objectives/2941?&pModal=false&site=UK&countryid=231, (accessed May 2014).

4 Numerical Methods

This chapter describes how the electric field within samples is estimated, in order to obtain undistorted images of seeding particles for use in particle velocimetry analysis. There are three stages to the numerical reconstruction: first the hologram is processed to recover the field in the plane of the detector, then the field at the detector is propagated to the plane of the sample, finally the field on the surface of the sample is calculated and propagated inside the sample.

4.1 Recovering the Field at the Detector

A hologram, the time-averaged intensity on the detector of the interference between some field scattered by an object and a reference beam, can be written, using the usual notation (see Chapter 2)

$$\text{Object Hologram: } |O|^2 + |R|^2 + O^*R + R^*O, \tag{4.1}$$

where, O is the complex field due to the object wave, R is the reference field and $*$ denotes the complex conjugate. Only the last two terms, the cross terms, retain information about the relative phases of the reference and object beams. For every set of holograms that are recorded of samples, a matching reference hologram – one taken without a sample in place – is recorded

$$\text{Reference Hologram: } |P|^2 + |R|^2 + P^*R + R^*P, \tag{4.2}$$

where, P is the incident field on the detector due to the illumination beam without the object present. The empty object beam is assumed to be the field due to a spherically expanding point source.

In an off-axis hologram, the angular separation of the object and reference beams creates a bulk modulation of the cross terms. This bulk modulation has the effect of shifting the cross terms to side bands in the spatial frequency domain (figure 3.6).

As described in the previous chapter, the separation is chosen correctly during alignment so that the cross terms do not overlap with the self-interference terms in Fourier space. If the terms do not overlap, a cross term, R^*O for example, can be extracted alone from the object hologram. If this term is multiplied in image space by the cross term P^*R extracted from the reference hologram, the result is the complex field $|R|^2P^*O$. This step will be known as demodulation.

Once demodulated, the holograms must be multiplied by a numerical replica of the empty object wave – to cancel the phase due to the P^* term. If we assume that P is the field on the detector due to a perfect point source, it is given by

$$P = \frac{e^{-ikl}}{|l|} \tag{4.3}$$

where, $k = 2\pi/\lambda$ and l is the distance from each point (x, y, z) on the detector to the source located at (x_0, y_0, z_0), figure 4.1. For a perfect spherically expanding wave, $l = \sqrt{(x-x_0)^2 + (y-y_0)^2 + (z-z_0)^2}$. Following multiplication by P, the result is an array which is $|R|^2|P|^2O$ which contains only phase information relating to the object wave. The multiplicative factors are of no concern as they will only affect the relative intensity of the wave at the detector. The next section shows how the complex field $|R|^2|P|^2O$ can be propagated from the plane of the detector to the region of the sample in a numerical environment.

4.2 Propagation of the Field Back to the Sample

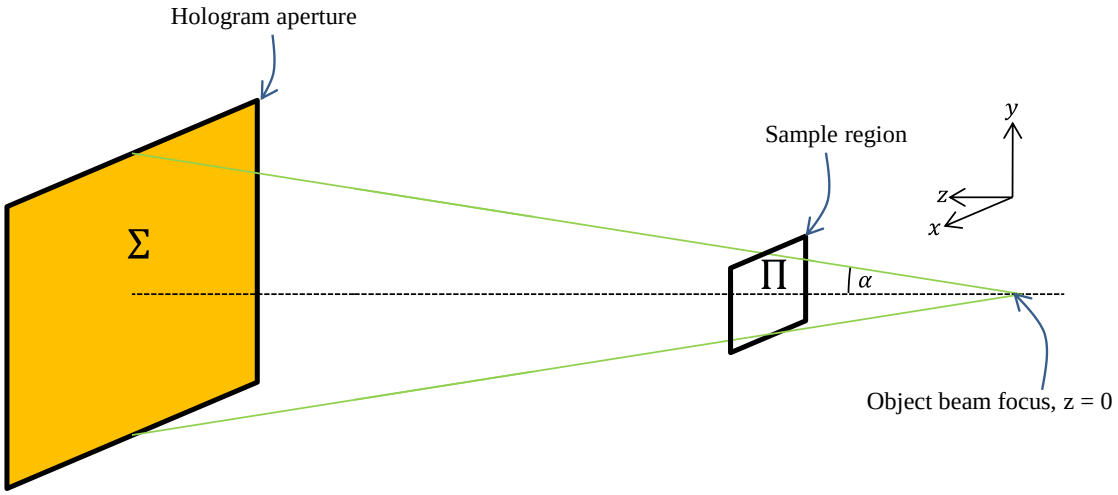

Figure 4.1 The geometry of the propagation from the CCD to a plane close to the sample. The relative size of the sample and its distance from the detector are exaggerated for clarity. The angle $\boldsymbol{\alpha}$ is the half angle of the cone of light collected by the detector ($\boldsymbol{\Omega = \sin\alpha}$), **Σ** is the hologram aperture and **Π** is a plane close to the sample and parallel to **Σ**.

The next step is to propagate the field in the plane of the detector the relatively long distance to some plane near the sample. The geometry of the propagation is shown in figure 4.1. The propagation is based on scalar diffraction theory, making use of the Rayleigh-Sommerfeld equation, encountered in Chapter 2

$$U_1(x_1, y_1, z_1) = \frac{1}{i\lambda}\int_{\Sigma} U_0(x, y)\frac{e^{ik\rho}}{\rho}\cos\theta\, dxdy \tag{4.4}$$

where, U_0 is the field in the hologram plane, $U_1(x_1, y_1, z_1)$ is the field at some other point in space, ρ is the distance between a point (x, y) on the hologram plane and a point (x_1, y_1, z_1) and $\cos\theta$ is an obliquity factor – assumed in this case to be equal to 1. In practice, I found that neglecting the obliquity factor gives an average error in amplitude at the aperture Π of 0.6 % and an average error in phase of 0.8 mRad. Equation (4.4) is a mathematically precise form of Huygens's principle.

My initial attempts at propagation involved a direct solution of the Rayleigh-Sommerfeld equation. If N^2 is the number of samples over the hologram aperture Σ, each point on the aperture Π requires the calculation of N^2 square roots, as many

exponentials, a point-wise multiplication of two N^2 arrays and a summing operation. The time required to propagate from the hologram plane to the sample plane is in this manner is proportional to $N^2 \times M^2$ where M^2 is the total number of samples over the aperture Π. N^2 is typically around 572×10^3 samples and M^2 337×10^3 samples for a cylindrical jet and around 563×10^3 samples for a swell.

Solving the integral in this way is very slow and in an attempt to speed up calculations, an implementation that took advantage of the symmetry of propagating between two square planes that share a common centre was developed. The new implementation reduced the number of calculations by a factor of 4 but the program still took around 8 hours per propagation. The lengthy computation time is compounded by the fact that a single instantaneous measurement consists of two individual holograms. A processing time of around 16 hours for each image pair was not compatible with our vision of the system as a practically applicable tool.

A second approach was to attempt to solve (4.4) as a convolution – taking advantage of the efficient fast Fourier transform algorithm. Equation (4.4) may be viewed as a superposition integral, i.e. the field U_1 can be determined by the superposition of spherical wavelets emanating from points on the source plane U_0. The equation therefore may be solved by a convolution of some impulse response g with the sources in the hologram plane. The impulse response is

$$g(x,y) = \frac{1}{i\lambda}\frac{\exp\left(ik\sqrt{x^2+y^2+D^2}\right)}{\sqrt{x^2+y^2+D^2}} \tag{4.5}$$

where D is the distance between the two planes. The convolution cannot be directly applied as the pixel sizes in the resultant field always match those in the source field. Locking of the pixel sizes causes two issues, firstly, with the original pixel size on the detector being 7.4 μm we would only end up with around 14 samples across the width of a 100 μm jet. The second issue is related to the proper sampling of the term P. In order to have an unambiguous numerical definition of a wave, the Nyquist-Shannon sampling theorem must be satisfied – two samples must be recorded per minimum spatial period or in other words minimum sampling frequency must be at least double the maximum spatial frequency.

The maximum spatial frequency in the digital replica of the term P in the plane of the detector, Ω/λ (up to 5.1×10^5 m^{-1} in the current microscope) is much higher than the sampling rate of the detector (1.4×10^5 m^{-1}). A demodulated hologram simply multiplied element-wise by a replica of P is greatly under sampled. Under sampling has no effect if the propagation is by solution of the Rayleigh-Sommerfeld integral, as each element in the $|R|^2|P|^2O$ array is treated as a point source with a particular phase and intensity. However, aliasing effects mean that propagation by convolution with a phase map will not yield sensible results.

Aliasing effects may be avoided by interpolating the demodulated hologram before it is multiplied by the term P. If we wish to faithfully represent all possible spatial frequencies of monochromatic radiation of wavelength λ, a sampling rate of greater than $2/\lambda$ is required to satisfy the Nyquist–Shannon theorem. If the demodulated hologram, a square area the size of the camera's sensor (231 mm^2) were sampled at such a rate, resulting complex arrays would require over 24 GB of RAM each at single precision. However, interpolation to a sampling rate as high as $2/\lambda$ is unnecessary. Given that holograms are recorded at a finite numerical aperture (Ω), any spatial frequencies present in the data greater than Ω/λ are essentially noise. Interpolation to a sampling rate of $2\Omega/\lambda$ yields a more manageable up-sampled array of around 4.3 GB (for the largest possible aperture, Ω = 0.42). In practice, the sampling rate has to be slightly higher than the theoretical $2\Omega/\lambda$ limit.

Multiplication of the demodulated hologram with the term P in image space is a convolution in the frequency domain – meaning that the resulting field has a bandwidth equal to the sum of the bandwidths of the demodulated hologram and the term P. As calculated in Chapter 3, the maximum bandwidth of a cross term ω_{cross} is approximately $1/2\Delta\left(1+\sqrt{2}\right)$, Δ being the pixel spacing on the detector. In the case of the microscope used in this work, the maximum bandwidth of a cross term is 2.8×10^4 m^{-1}. Increasing the sampling rate of the interpolated array by ω_{cross} results in an array of around 4.6 GB, comfortably manipulated and operated on using a PC with 12 GB RAM.

The convolution theorem states that the Fourier transform of a convolution is the point-wise product of Fourier transforms. The convolution required for propagation can then

be written $\mathcal{F}\{U(\mathscr{P}_1)\} = \mathcal{F}\{U(\mathscr{P}_0)\}\,\mathcal{F}\{g(x,y)\}$, where $\mathcal{F}$ denotes the Fourier transform and $\mathscr{P}_0$ and $\mathscr{P}_1$ represent points on the hologram plane and sample plane, respectively. Helpfully, the Fourier transform of $g(x,y)$ has an analytic solution, given by Goodman,[1]

$$G(f_x, f_y) = \exp\left(ikD\sqrt{1 - (\lambda f_x)^2 + (\lambda f_y)^2}\right). \tag{4.6}$$

By taking advantage of equation (4.6), the significant operations necessary for propagation can be reduced to one Fourier transform and one inverse Fourier transform. A single propagation from the detector to the sample plane takes less than 40 seconds (Intel Core i7-3770 3.4 GHz) with this method, including the interpolation at the detector plane. Once the field is recombined at the sample plane, a small part of the large array – corresponding to the desired field of view, typically around 150 × 380 μm^2 – is cropped out and saved for further processing. The method used in these propagations involves no paraxial approximation.

4.3 Propagation Parameters

In order to implement the propagations described in the previous section, the distance between the focus of the objective and the camera (D) must be known, in order to generate the numerical replica of the point source, P. From simulations of reconstructions, I have found that a small multiplicative error of N % in the length D leads to an error of N % in the scaling of the reconstructed field perpendicular to the optical axis and an error of $2N$ % along the optical axis. The sensor is located some way inside the camera housing, making it impractical to measure D to a high enough degree of accuracy. Instead, D is found by accurately measuring the separation between the two point sources using a razor blade mounted on a pair of micrometer-controlled translation stages (Thorlabs). The edge of the blade is placed so that it just blocks the reference beam at its focus, then translated along the focal plane of the objective until it just blocks the object beam at its focus. The difference between the micrometer readings gives the separation of the focuses, s, to ± 0.5 μm.

Close to the centre of the CCD, the spatial frequency of the fringes, f_{centre}, is well estimated by

$$f_{\text{centre}} = \frac{s}{\lambda D}. \tag{4.7}$$

A calibration hologram recorded of the interference between the object and reference beams is masked so that it has a value of zero everywhere apart from a small area in the centre, it is subsequently Fourier transformed using an FFT. The peak in the spectrum (~4.66×10^4 m^{-1}) can be located to an accuracy of ± 33 m^{-1}. Using equation (4.7), D can be found to an expected accuracy of 0.10 %. For a 100 μm sample, this equates to a maximum distortion along the optical axis of around $\lambda/3$, and half that in the lateral direction.

4.4 Estimating the Field inside the Sample

This section describes how the field inside the sample is estimated. First, the location of the surface of the sample is found, and then the field outside the sample is propagated through it. The theory behind the propagation through the surface is described, and how the propagation is implemented in a numerical environment is explained. The section concludes with an overview of preliminary results of the recombined field within a cylindrical liquid ink-jet stream.

4.4.1 Locating the Surface of the Sample

In order to estimate the field inside the sample, the field in the surrounding medium must be propagated through the sample's front (toward the camera) surface. The first step must be to estimate a reasonable position and form of the sample's front surface.

The hologram is first refocused using the propagation kernel (equation (4.6)) from plane of the detector to $z = 0$ (the laser focus). It is then propagated, back towards the camera until the edges appear sharp. The refocusing is performed manually, aided by a trace of

the gradient of the intensity across the central few rows of pixels. The image is propagated backwards and forwards with decreasing step size until a peak in the gradient – between the bright background illumination around the sample and the comparatively dark area inside the sample – is located. The plane where the edges are said to be in focus is located to ±0.5 μm. The manual focussing procedure is followed for a single exposure from each dataset and the plane of the sample is assumed to be the same for all exposures in that set. All exposures are propagated to this plane and the complex recombined wave for each is saved.

The edge of the sample could be detected directly from these images and, using an axisymmetric approximation, the shell could be deduced by sweeping the edge through space around its axis of rotational symmetry. This method was used in early tests; however, it behaved poorly in situations where the sample was not exactly vertical. A better method is to detect the tilt of the sample from the vertical before a surface is estimated.

A binary image of the footprint of the sample in every exposure is found by applying an intensity threshold half-way between the intensity of the background and the minimum inside the sample. Intensity peaks again inside the sample so the binary image has a hole in the middle – but it is trivial to fill this in. Using a moment of area method, the long axis of the sample is found and the binary image is rotated so that its long axis lies parallel to the vertical axis. The rotated binary image is then summed horizontally to give a profile of diameter with height; this is halved to give the radial profile. The profile is then rotated about the axis of symmetry of the sample to give the surface. When the surface is used as a filter, its coordinates are rotated back to match the real sample – rather than rotating the volumetric complex field data which would be time-consuming and lead to inaccuracies.

4.4.2 Propagation at the Boundary – Theory

The theory behind numerically propagating light through a curved interface is described in this section. The method I use is based on the work of Wormald and Coupland[2]; the description below largely follows theirs.

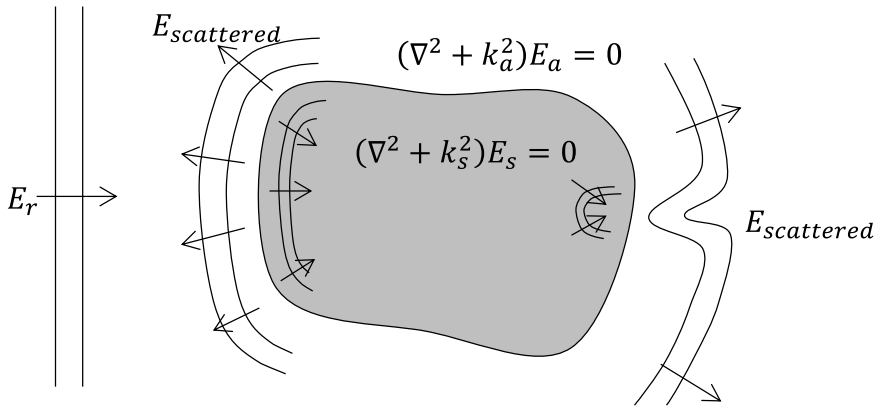

Figure 4.2 Scattering from a curved, transparent object in air. Reproduced from reference [2].

The scattering geometry of a region of a scattering sample in air is shown in figure 4.2. The scattering fields are E_a and E_s; they are the scattering fields in the surrounding air and inside the sample respectively. We begin assuming that they are scalar fields and as such must obey the scalar Helmholtz equation:

$$(\nabla^2+k_a^2)E_a = 0 \tag{4.8}$$

$$(\nabla^2+k_s^2)E_s = 0, \tag{4.9}$$

where, $k_a = 1/\lambda_a$ and $k_s = 1/\lambda_s$ are the wave numbers in air and in the sample medium and ∇^2 is the Laplacian operator. We also know that the fields outside the sample, and the fields inside the sample are coupled by certain boundary conditions; these are that the complex amplitude of the field and its normal derivative are constant at the boundary, i.e.:

$$E_a(\vec{r}_{\text{surf}}) - E_s(\vec{r}_{\text{surf}}) = 0 \tag{4.10}$$

$$\frac{\partial}{\partial \boldsymbol{n}}\left(E_a(\vec{r}_{\text{surf}}) - E_s(\vec{r}_{\text{surf}})\right) = 0, \tag{4.11}$$

where, $\vec{r}_{\text{surf}}$ is the boundary of the sample. The field outside the sample is the sum of the scattered field, $E_{\text{scattered}}(\vec{r})$, and the field $E_r(\vec{r})$ which is the illumination field if the object were missing. The field outside, $E_a(\vec{r})$, can be written

$$E_a(\vec{r}) = E_{\text{scattered}}(\vec{r}) + E_r(\vec{r})\,. \tag{4.12}$$

The measured quantity in the holograms is this sum, over a finitely sampled range of $\vec{r}$ describing the surface of the detector. Wormald and Coupland note at this point that, by using the Fresnel-Kirchoff diffraction formula[1] and a boundary element method, equations (4.8)–(4.12) could be solved to find $E_{\text{scattered}}(\vec{r})$ and $E_s(\vec{r})$, but recommend a more direct solution.[2]

They begin by assuming that, for smooth objects, the scattered field can be written in terms of the following surface integrals

$$E_s(\vec{r}) = \int_{\Sigma_+} S_+\left(\vec{r}_{\Sigma_+}\right) \frac{\exp\left(ik_s\left|\vec{r} - \vec{r}_{\Sigma_+}\right|\right)}{\left|\vec{r} - \vec{r}_{\Sigma_+}\right|}\, ds \tag{4.13}$$

$$E_{\text{scattered}}(\vec{r}) = \int_{\Sigma_-} S_-\left(\vec{r}_{\Sigma_-}\right) \frac{\exp\left(ik_a\left|\vec{r} - \vec{r}_{\Sigma_-}\right|\right)}{\left|\vec{r} - \vec{r}_{\Sigma_-}\right|}\, ds, \tag{4.14}$$

where, $\Sigma_+$and Σ_- are surfaces just outside and inside of the boundary and S_+ and S_- are source strengths per unit area. The interpretation of equations (4.13) and (4.14) is sketched in figure 4.3. The internal field, $E_s(\vec{r})$, can be formed from a set of sources just outside the boundary of the sample radiating inwardly; similarly a set of sources just inside the boundary radiate outwardly to form the scattered field, $E_{\text{scattered}}(\vec{r})$.

Numerically, the integrals could be replaced with sets of uniformly spaced sources placed over the outside and inside faces. It would then be relatively easy to solve the equations numerically and the fields could be calculated accounting for internal reflections.

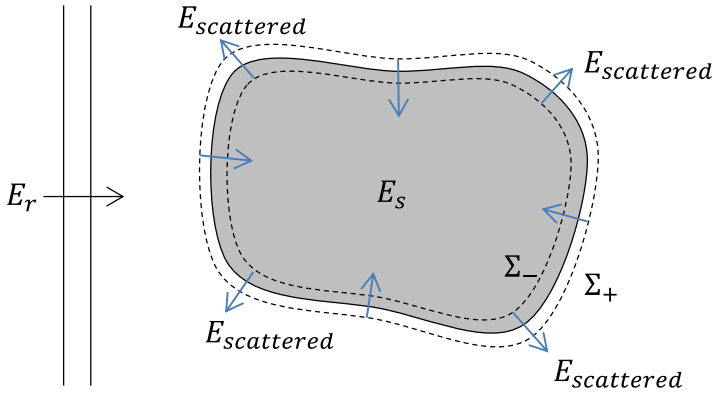

Figure 4.3 The boundary surfaces in equations (4.13) and (4.14). Reproduced from reference [2].

The problem is then simplified by making two assumptions. The first is that it is adequate to estimate the internal field by integrating over a finite portion of the sample surface, i.e. Σ_+ becomes only the front (towards the camera) face of the sample. The second assumption is that the field inside the sample is dominated by the local sources, justified if the internal reflections are secondary and do not contribute much to the field. These assumptions allow us to write:

$$S_+(\vec{r}_{\Sigma_+}) \approx \frac{1}{i\lambda_s} E_m(\vec{r}_{\Sigma_+}), \tag{4.15}$$

where, E_m is the measured field on the sample surface – obtained from propagating the field back to the sample from the detector. With this simple definition of $S_+(\vec{r})$, it is possible to solve equation (4.13) to approximate $E_s(\vec{r})$, the field inside the sample. The next section will describe the fast numerical implementation developed to solve the integral.

4.4.2.1 A Note on the Assumptions

The assumptions made above allow us to define a set of sources outside the sample that radiate inwardly in terms of the measured field on the sample surface (equation (4.15)). This in turn allows the field inside the sample to be estimated without the need to solve a complicated inverse problem. It is worth briefly discussing the implications of the

assumptions. The assumptions are that all of the fields are scalar, the surface of the sample is known, its refractive index is known and that the effects of internal reflections do not affect our ability to reliably detect particle displacements.

The scalar approximation effectively ignores the polarisation of light, however, the polarisation changes on reflection and refraction and may cause errors if ignored in this work where fields are propagated through boundaries between media. Holograms were recorded with the light polarised both parallel and perpendicular to the axis of symmetry of a cylindrical sample and no difference could be observed in the reconstructed images.

Sub-section 4.4.1 shows how sample surfaces are located. If the method of locating the surfaces is correct, it should be possible to propagate the field through the front (toward the camera) surface into the sample, then propagate this light through the rear surface into the air behind and recover the illuminating point source. If the recovered illumination source appears in the same position as in reality then the illuminating wave has been recovered reliably implying that the position of the surface has been estimated well.

It seems reasonable to assume that internal reflections may be ignored. The proportion of light reflected at an interface between two media can be predicted by the Fresnel equations. The fraction of incident power reflected depends on the refractive indices of each medium and the angle of incidence. The angles of incidence at the front, water-air, interface of the jet can be found as an output of the ray-tracing code mentioned in section 3.1. Using the Fresnel equations (assuming unpolarised light), the average percentage reflection of light reaching the front surface is 2.5 % in amplitude. The maximum percentage reflection of any ray was 5.6 % in amplitude. In order for any internally-reflected light to reach the detector and contribute to the hologram, further internal reflections and hence further losses occur. The worst case is light very close to the optical axis which requires only two internal reflections to reach the detector. In this case, the percentage reflection is 2 % at both interfaces and the light reaching the detector has approximately 0.04 % of the amplitude of the directly transmitted light.

4.4.3 Propagation at the Boundary – Implementation

The first step is to assign values to the surface found earlier. This is a filtering operation on a 3D array of image-space data. The 3D array is built up by a concatenation of 2D slices of the reconstructed field, extending from a few microns in front of the sample back to its mid-plane. The planes are separated by less than $\lambda_s/3$, the exact spacing varies depending on the experiment as the arrays sizes are constrained for efficient FFT operations – i.e. dimensions do not have large prime factors.

The 3D field data is then filtered to extract the surface values, but because any array of field data is always finitely sampled in all dimensions, very few values ever actually lie on the surface itself. It is better then, to avoid sparse and discontinuous surface data, to multiply by a mask, M_{surf}, calculated thus:

$$M_{\mathrm{surf}}(\boldsymbol{P}) = e^{-(|\boldsymbol{P}_{\mathrm{surf}}-\boldsymbol{P}|)/\sigma} \tag{4.16}$$

where, $\boldsymbol{P}_{\mathrm{surf}}$ points to values on the surface, $\boldsymbol{P}$ points to the pixels inside the mask array and σ is the width of the distribution. The mask is designed so that when it is multiplied by the field array, points exactly on the surface are weighted 1 and σ is set such that the weighting falls off quickly to effectively zero a few of pixels from the surface. Once the 3D field data has been multiplied by the mask, the non-zero elements are assumed to be the surface sources and are ready for propagation inside the sample.

Two methods of propagation have already mentioned here; propagation by solution of the Rayleigh-Sommerfeld integral (equation (4.4)) and as a filtering operation – in 2D multiplication by the transfer function (equation (4.6)) in frequency space. We would prefer to avoid solving the Rayleigh-Sommerfeld integral directly, as given the large number of surface sources, even to populate the just central plane of the sample would be a very intensive calculation.

Propagation can be viewed as the convolution of some set of source points with an impulse response. In this case, the impulse response is a spherically expanding wave of constant wavenumber k. The Fourier transform of such a function is dominated by values on a thin spherical shell with a radius k, known as the Ewald sphere (the dashed line in figure 4.4). Given that any hologram is recorded over a finite numerical aperture,

not all points on the Ewald sphere correspond to any measured spatial frequencies. In an effort to reduce the effect of propagating of spurious wavenumbers, the Ewald sphere should be constrained to a numerical aperture-limited cap. The NA-limited cap is the bold line in figure 4.4.

In the program, the filter is applied in a similar way to how the surface values were extracted. A weighting mask is created where values of wavenumber exactly equal to k are weighted 1, with the weighting factor disappearing quickly away from the shell. The mask is then cropped so that it is limited in the f_x and f_y directions. Once the mask has been created, it is multiplied by the Fourier transform of the source data then inverse Fourier transformed to effect the convolution.

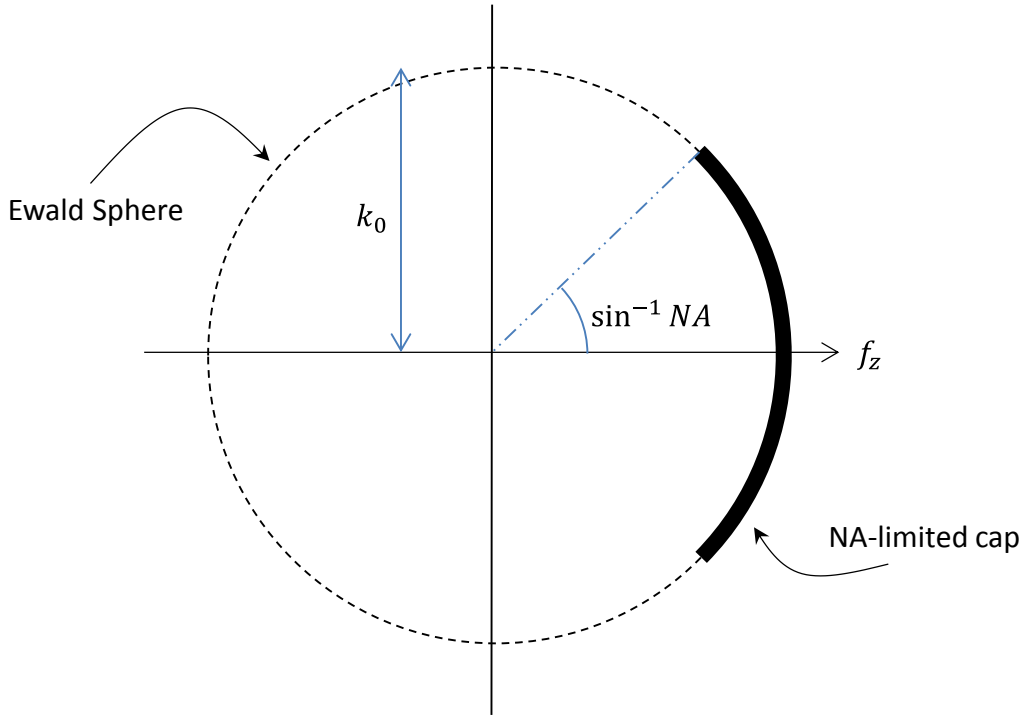

Figure 4.4 The Ewald Sphere.

It was noticed that the result was strongly affected by wrap-around artefacts. The discrete Fourier transform makes the implicit assumption that the data is periodic and thus is effectively tiled infinitely (this is a consequence of it being composed entirely of periodic functions). When the Fourier transform is used as a computational short-cut to perform a convolution this has the effect of convoluting not only with the data, but also with the implicitly assumed repeated data adjacent. In this case, the field of view is the

space covered by the 3D array and light which propagates beyond one side of the array re-enters at the opposite side. So that the wrap-around artefacts do not corrupt the desired information (the region occupied by sample), the source array is zero padded to double its size in image space prior to the convolution. The middle plane of the zero padded reconstruction was extracted and then propagated in the usual plane-wise manner through the sample volume, populating it with an estimate of the complex field inside. The full calculation of the internal field in a stretch of jet 380 μm long with a diameter of 99 μm takes around 40 seconds (Intel Core i7-3770 3.4 GHz).

4.4.4 Examples

I will show here the some of the arrays generated by the propagation code, for a qualitative overview of the process. Figure 4.5 shows the raw object and reference holograms and figure 4.6 shows the absolute value of their two dimensional Fourier transforms. In both of the spectra, the terms can be easily seen and are clearly separated. It is worth noting that the cross terms in the reference hologram (figure 4.6b) are diamond-shaped. If it were the spectrum of two interfering plane waves, the term would look like a symmetric dot as the fringe spacing would be constant across a flat detector. The interference pattern between the two point sources in the reference hologram recorded on my microscope has flat uniform fringes toward the centre of the image, becoming curved and farther apart toward the edges. This is consistent with numerical simulations of the interference pattern between two ideal point sources situated similarly.

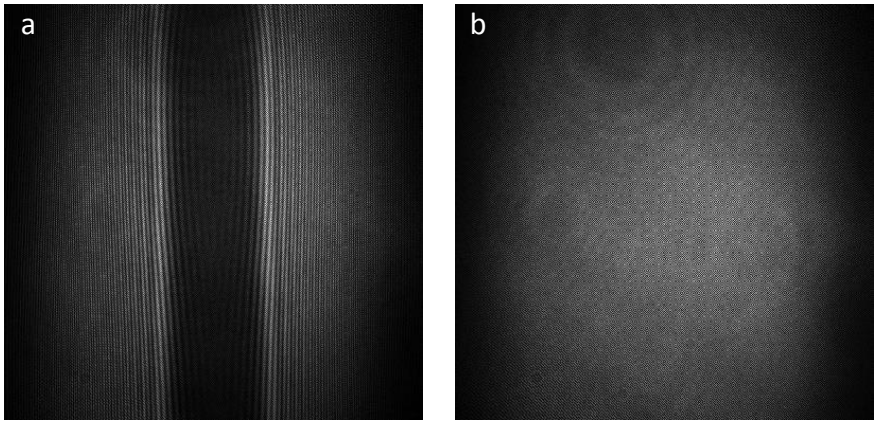

Figure 4.5 Holograms with (a) and without (b) the sample in place. The sample is a 99 μm diameter jet seeded with 1 μm polystyrene spheres.

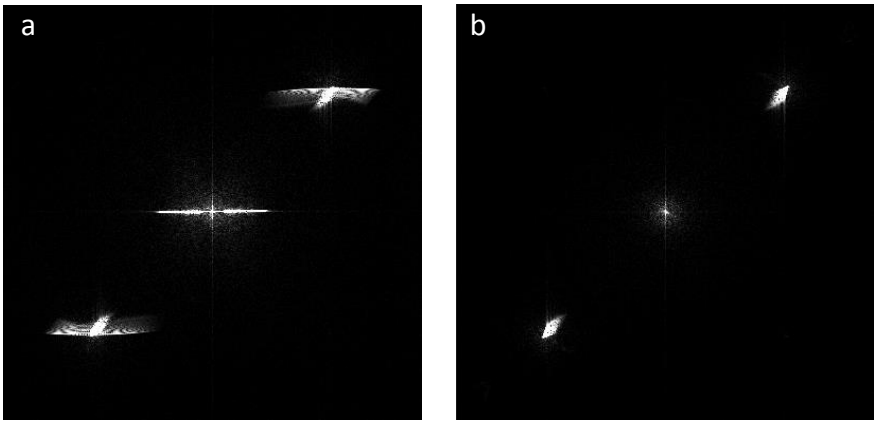

Figure 4.6 The Fourier transforms of the holograms shown in figure 4.5.

Figure 4.7 shows a recombination in the plane of the sample, with the amplitude of the complex field shown in figure 4.7a and the wrapped phase in figure 4.7b. Some seeding particles are visible in the recombined image.

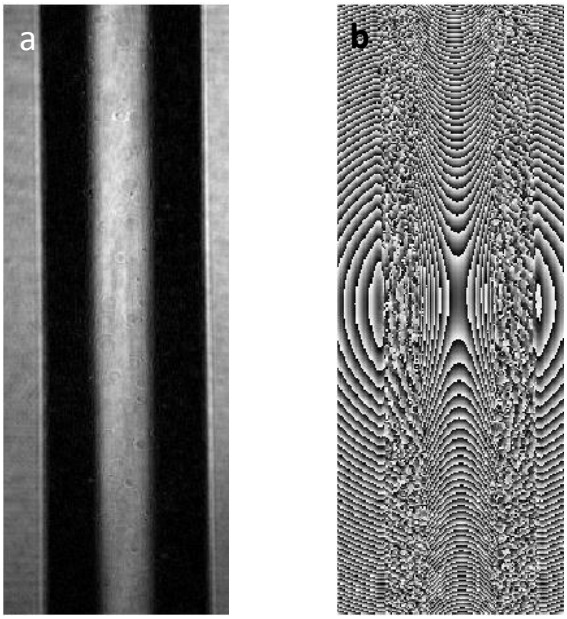

Figure 4.7 Recombinations of the plane of the sample, used to find the edges of the sample. (a) shows the absolute value of the recombined field and (b) shows the phase of the field.

Figure 4.8 shows the amplitude of the field calculated inside the same sample. A number of out of focus particles can be seen as well as in-focus particles, which are visible as black dots on the brighter background. From the *y*-*z* and *x*-*z* sections, the elongation of particle reconstructions in the direction of propagation can be seen.

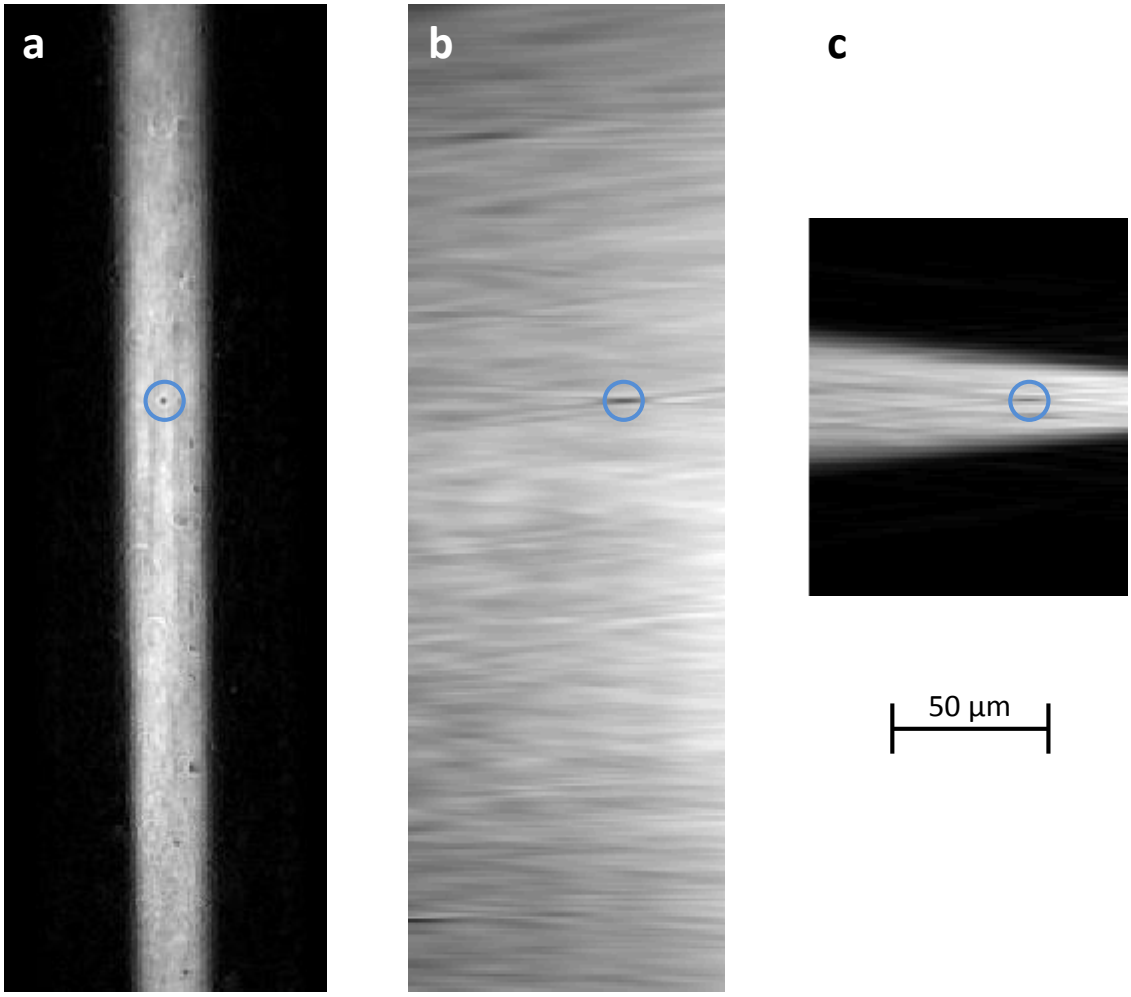

Figure 4.8 The recovered field inside the sample. (a), (b) and (c) are sections in the x-y plane, the y-z plane and the x-z plane respectively. The same particle is highlighted with a blue circle in all three planes. The sample is 99 µm in diameter and the scale bar applies to all three sub-figures.

4.5 Validation

In this section I show that the holographic reconstructions yield physical results. Firstly, I ensure that the field calculated on the surface of the sample is not distorted by validating the reconstruction method in air. Secondly, I validate the method of finding the sample surface by propagating all the way through the sample in order to recover the original illuminating wavefront.

4.5.1 Scaling of the Holographic Reconstructions

Simulated holograms and their reconstructions showed that the scaling of the reconstructed space depends strongly on the distance between the illumination source and the CCD. In order to confirm that the methods proposed are capable of accurately reconstructing the sample volume, without any scaling errors, holograms of the edge of a razor blade were recorded at different positions within the sample volume (figure 4.9). Reconstructed holograms were refocused using the convolution method until a maximum in the gradient between the background intensity and the edge of the razor blade was found.

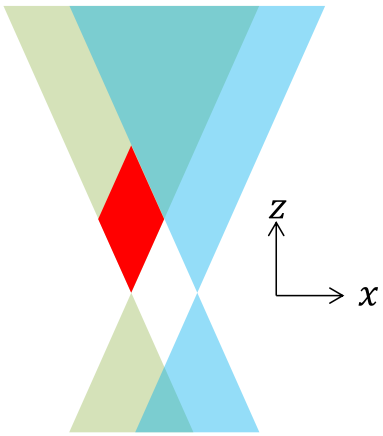

Figure 4.9 The sample region in the holographic microscope. The object beam is coloured pale green and the reference beam pale blue. The red diamond highlights the sample region (550 μm wide and 1188 µm long). The camera is located above the sample region at positive $\boldsymbol{z}$.

A razor blade was mounted on a pair of orthogonal translation stages with sufficient travel to cover the whole measurement region in x and z, and 1 μm resolution. The edge razor blade was first centred on the object focus ($x = 0, z = 0$) and translated in the positive z direction. Holograms of the blade were recorded every 100 μm, from z = 180 μm to z = 1180 μm. Then, the blade was moved to z = 580 μm, and the position in x was varied between x = -180 μm and x = 220 μm in steps of 50 μm. The results are shown in figure 4.10 and figure 4.11.

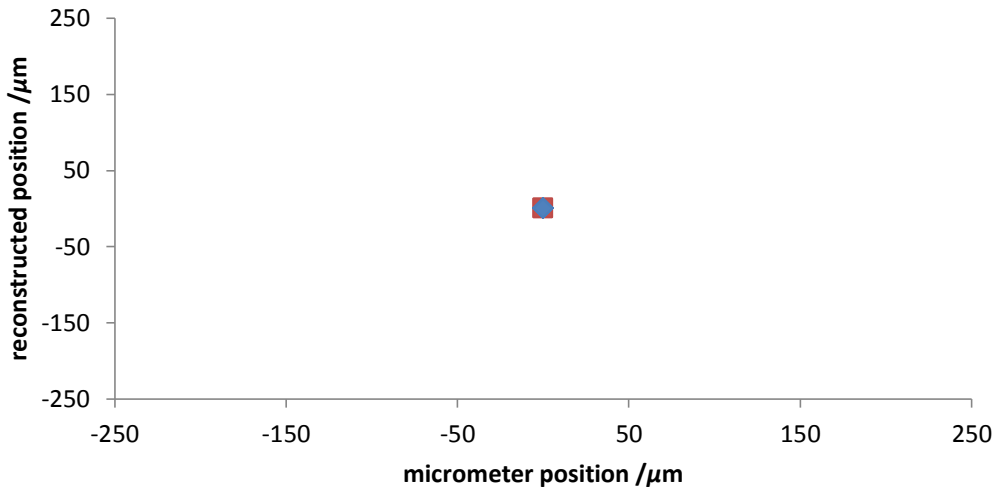

Figure 4.10 The relationship between actual position of the blade edge and the reconstructed position in the ***x***-direction

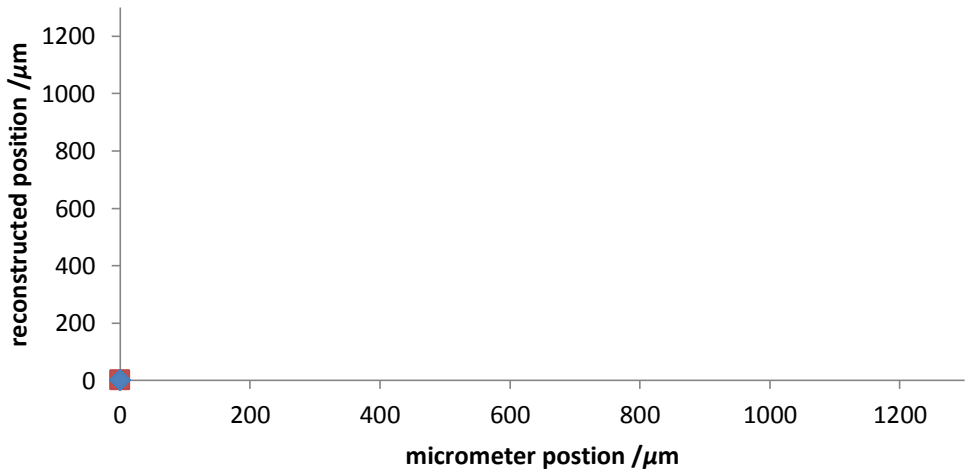

Figure 4.11 The relationship between actual position of the blade edge and the reconstructed position in the ***z***-direction.

In both x and z, the recombined cooridnates are linear with a scaling factor of approximately unity compared to the real world coordinates (0.9965 ± 0.0097 in x and 0.9958 ± 0.0087 in z). The errors arise from the uncertainty in positioning the razor blade in the experiments (precision of the translation stages) and the resolution of the reconstructed images, dictated by the effective numerical aperture of recording. These findings suggest that the method of propagating the recorded field on the detector to the sample plane (Section 4.2) and the method of estimating the source to CCD distance, D, (Section 4.3) are valid.

4.5.2 Recovery of the Illuminating Wave

If the surface has been located properly, then the original illuminating wave can be recovered by propagating the scattered wave into the front (toward the camera) surface of the sample and then out of the back of the sample. The sample is illuminated by a diverging wave emanating from a known point. It is possible take advantage of this to give a convenient check on how successful the placement of the sample surface is. By propagating this wave through space and finding where it comes to a focus, it is possible to assess if the surface of the sample has been located well.

The sample used was a cylindrical stretch of an unseeded water jet with a 99 μm diameter, flowing at 6 m/s. The jet was placed 784 μm away from object source in an alignment with a source to CCD distance of 27.511 mm. Holograms are refocused using the convolution method to form a stack of planes. The planes are 160 μm in x, 435 μm in y and each plane was separated by 0.13 μm in z, less than half a wavelength in water. The pixel size in x and y was 0.73 μm. Figure 4.12 shows a slice through 3D array of the field data around the sample – assuming a constant refractive index ($n = 1$). The values inside the sample and behind it (to the left) are not meaningful as the refraction at the front surface has not been accounted for – it is similar to a slice through a stack of focussed images taken with an ordinary light microscope.

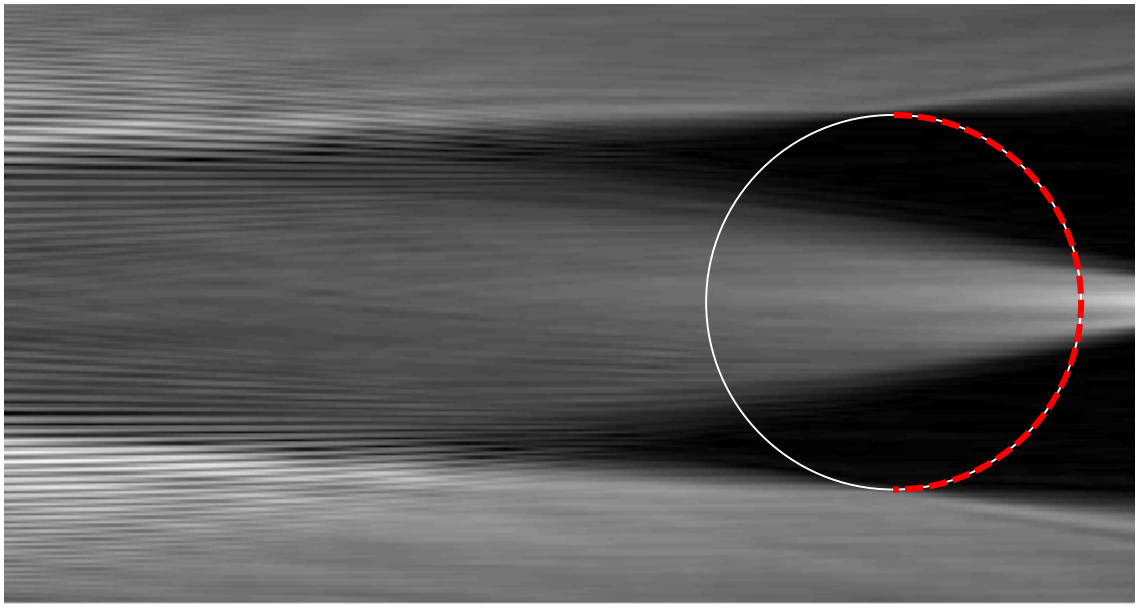

Figure 4.12 An ***x*-*z*** slice through the reconstructed field in air. The white circle shows the boundary of the 99 μm diameter sample. The broken red line shows the front surface of the sample.

The broken red line in figure 4.12 shows the estimated location of the front surface of the sample. Values on this surface – assumed to be just outside the sample are extracted using the filtering operation, described previously, to form a set of sources which will radiate inwardly. Figure 4.13 shows the form of the surface with the absolute value of the inwardly-radiating sources superimposed.

Figure 4.13 The front surface of the cylindrical jet. The grey scale is the absolute value of electric field on the surface.

The inwardly-radiating sources are then propagated inside the sample using the 3D convolution method described previously, using the wavelength of the light in water in the kernel. An x-z slice through the result is shown in figure 4.14. Qualitatively, the result of the propagation through the front surface is that the light appears to diverge less strongly – as expected from the earlier ray-tracing analysis.

Figure 4.14 An $\boldsymbol{x}$-$\boldsymbol{z}$ slice through the reconstructed field inside the sample. The grey scale shows the absolute value of the electric field inside.

The field at the back of the reconstructed volume of the sample is filtered to produce a set of outwardly-radiating sources just inside the rear surface. These sources then are propagated into the surrounding space (using the wavelength of the light in air). The recovered wave is then propagated to a small ($60 \times 60 \times 120\ \mu\text{m}^3$) volume around its focus. The distribution of intensity within this volume is shown in figure 4.15. The peak in intensity is located at ($0.15 \pm 0.73\ \mu$m, $1.61 \pm 0.73\ \mu$m, $-3.61 \pm 0.13\ \mu$m) in (x, y, z), where the expected location of the focus is (0,0,0). The negative sign on the location in z indicates that the recombined focus is 3.61 μm farther away from the sample than its ideal location. The most obvious feature is that the focus is extended more in the x direction than in the y direction. This is due to the fact that 99.9 % of the intensity in the recovered plane directly behind the sample was confined to a stripe 43 μm wide and 379 μm high. There is therefore a significantly lower numerical aperture, and therefore a broader focus in the x than in the y direction. Table 4.1 compares the spread of the intensity to an ideal case. The ideal case is simulated by using the amplitude of the wave recovered behind the sample but replacing its phase with the phase due to an ideal point

source placed at (0,0,0), and propagating it to the same small volume around the focus. The results show that the experimental focus is slightly broader than the real focus.

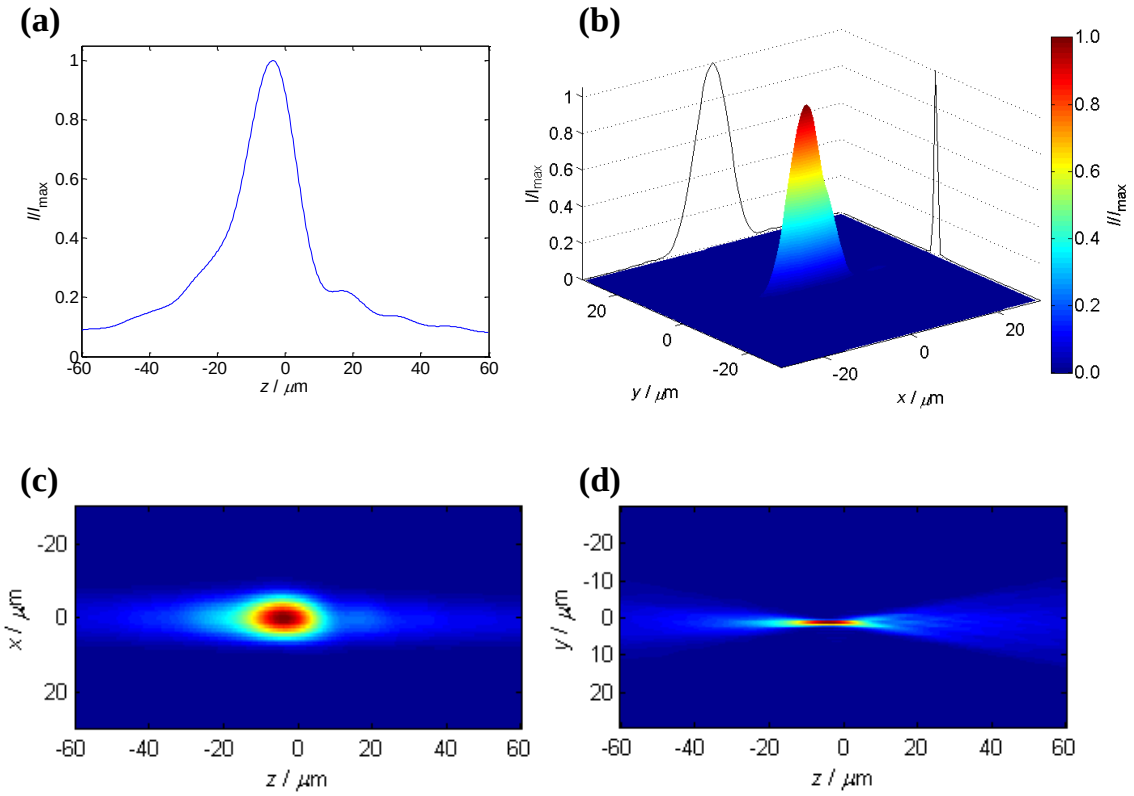

Figure 4.15 The distribution of intensity around the recovered focus. (a) The change in intensity with z in the centre of the focus. (b) The distribution of intensity in x and y. (c) and (d) $\boldsymbol{z,x}$ and $\boldsymbol{z,y}$ intensity maps respectively.

Table 4.1 Comparison of the shape of the real and ideal reconstructed focuses, by means of their full width at half maximum (FWHM).

	Real width /μm	Ideal width /μm	Difference
FWHM (x)	9.20	9.03	2 %
FWHM (y)	1.25	1.20	4 %
FWHM (z)	19.90	18.42	8 %

It is hard to say whether an absolute error in the position of the focus of 3.61 ± 0.13 μm means that the surface has been found satisfactorily. We therefore investigate the effect

that a small change in either the radius of curvature or the position of the surface has on the focal point of the reconstructed wave. We do this by simplifying the problem, using geometric optics and approximating the cross section of a cylindrical sample as a thin lens. The simplified problem is sketched in figure 4.16.

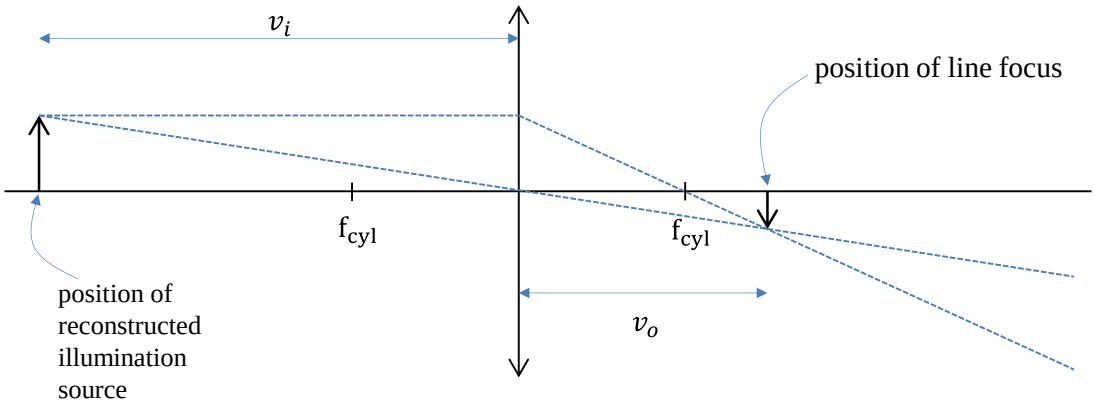

Figure 4.16 A simplified view of the behaviour of passing light through a cylindrical cross-section.

We consider that during recording, the sample acts as a positive cylindrical lens, imaging the point source of illumination to a line focus in front of itself. During reconstruction, we are attempting to recreate the lensing effect of the sample exactly, so that the line focus is imaged back on to the position of the illuminating point source. To give us an idea how sensitive the position of the reconstructed focus is to changes in the sample position and radius of curvature, we will derive some simple algebraic relationships. There are four parameters involved, the location of the original illuminating focus, the location of the line focus of the sample, the position of the centre of the sample and its radius. The radius of the sample can be related to its focal length by

$$f_{cyl} = \frac{nR}{2(n-1)}, \tag{4.17}$$

where n is the refractive index and R the radius of curvature. Another well-known geometric optics equation is[3]

$$\frac{1}{f_{cyl}} = \frac{1}{v_i} + \frac{1}{v_o}, \tag{4.18}$$

where v_i is the distance between a lens and the image and v_o the distance between a lens and the object. In this case, v_o is the distance between the line focus of the sample and its centre and v_i is the distance between the sample and the illuminating point source.

First, assuming that the surface of the sample is correctly positioned, we investigate how the distance between the sample and the illuminating source (v_i) changes for a fixed position (v_o). The error in the recombined focus position (ε_{v_i}) can be written in terms of a small error in the sample radius (ε_{R}) as follows

$$\varepsilon_{v_i} = \left[\frac{2(n-1)}{n(\mathrm{R}+\varepsilon_r)} - \frac{1}{v_o}\right]^{-1} - v_{i(\mathrm{actual})}\,. \tag{4.19}$$

Equation (4.19) is plotted in figure 4.17 for a small range of ε_r, using a realistic sample radius, position and refractive index. The reconstructed source position appears to be very sensitive to the radius of curvature of the sample; the slope of the curve close to $\varepsilon_{\mathrm{R}} = 0$ is 123, implying that a ±1 % error in the sample radius (±0.5 μm) would cause an error in the position of the focus of around ±61.5 μm.

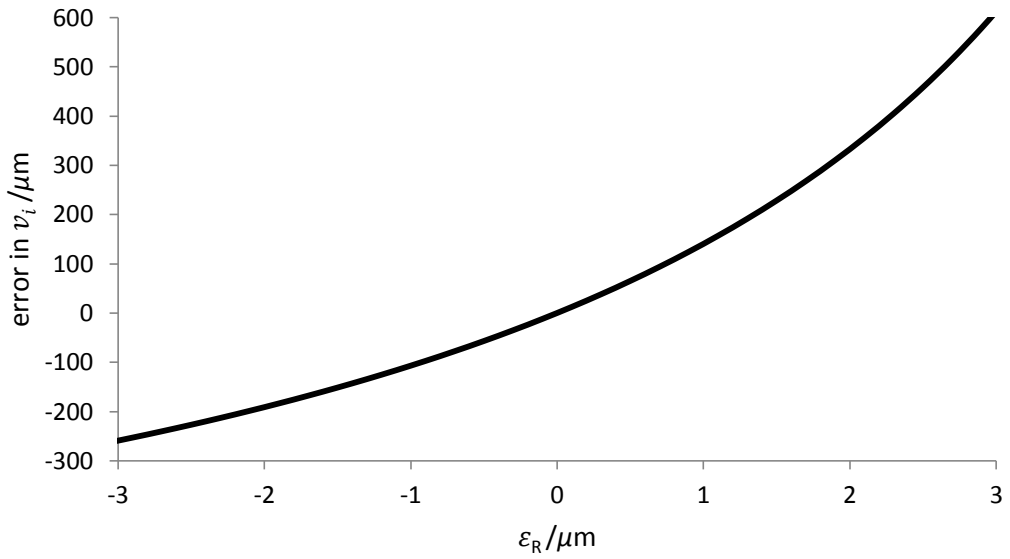

Figure 4.17 The relationship between a small error in sample radius and the resultant error in the position of the recombined focus. The constants used were: refractive index of 1.33, sample position of 800 μm from the focus and a radius of 100 μm.

The error in reconstructed distance for a small error in the position of the sample relative to its line focus (ε_{v_o}) can be written:

$$\varepsilon_{v_i} = \left[\frac{2(n-1)}{n\mathrm{R}} - \frac{1}{v_o + \varepsilon_{v_o}}\right]^{-1} - \left(v_{i(\text{actual})} - \varepsilon_{v_o}\right). \tag{4.20}$$

Figure 4.18 shows equation (4.20) plotted for a small range of ε_{v_i}, with realistic values for the constants. Although the reconstructed source position is less sensitive to the error in the sample position, the curve has a gradient of 45 at $\varepsilon_{v_o} = 0$.

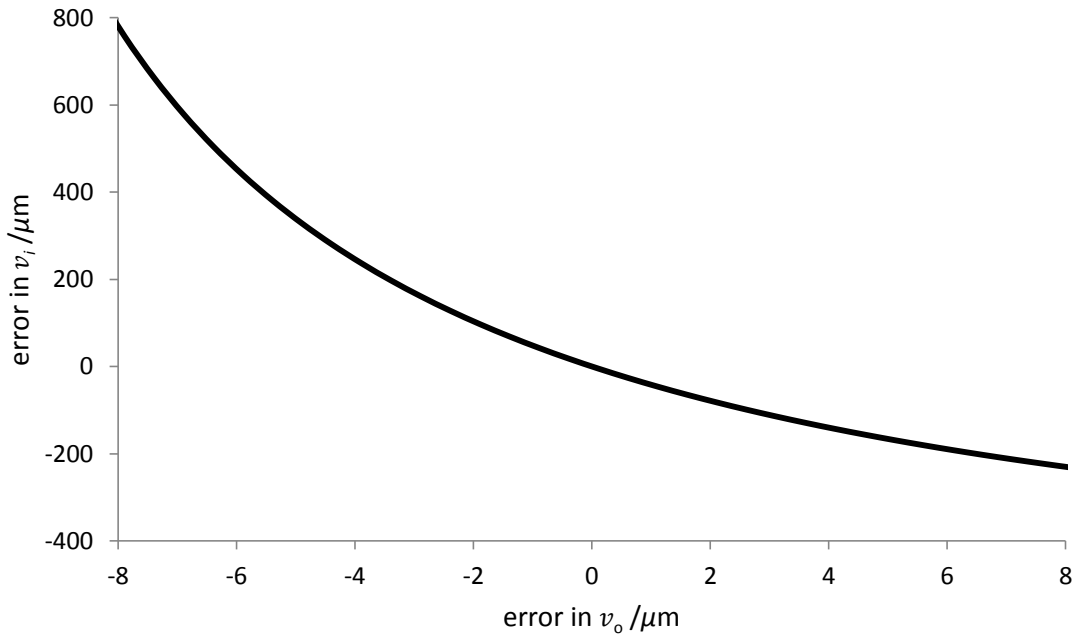

Figure 4.18 The effect of a small error in sample position on the error in the position of the recombined focus.

Considering the problem from a ray-optics point of view, suggests that, given the sensitivity of the position of the recombined focus to both the radius of the sample and its position, the surface of the sample has been estimated to a good degree of accuracy.

4.6 Conclusions

In this chapter I have shown how the field inside the sample is estimated prior to particle detection and velocimetry analysis. I have shown that estimating the field inside the sample is a multi-step process which requires some *a priori* information. A description of how relevant parameters required for the reconstruction are estimated and I have included the results of validation experiments to show that reconstructions yield physical results.

4.7 References

1 J. W. Goodman, *Introduction to Fourier Optics*, Roberts & Company, Colorado, 3rd edn., 2005.

2 S. A. Wormald, J. M. Coupland, 2010, *Journal of Modern Optics*, 57(9), 700-708.

3 E. Hecht, *Optics*, Addison-Wesley, 2nd edn., 1987.

5 Experimental

5.1 Introduction

This chapter describes how jets are generated, the procedures used to perform the experiments and the methods used to analyse the results to produce measurements of the internal velocity.

5.2 The Jet Apparatus

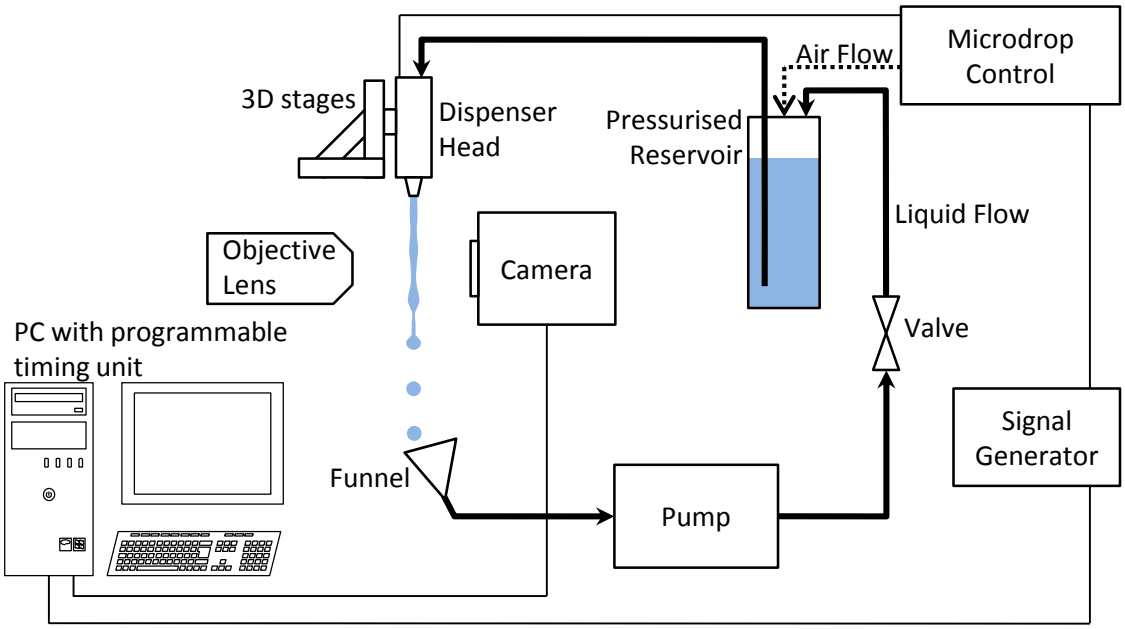

Figure 5.1 Schematic of the fluid flow and control system for generating the liquid jets.

The experimental apparatus for generating the continuous ink-jet stream is shown in figure 5.1. Fluid feeds from a 200 ml pressurised reservoir into a dispenser head (MJ-K-301, Microdrop Technologies GmbH), and a jet issues from a circular trumpet-shaped nozzle, with an internal diameter at the exit of 100 μm, into the surrounding air with a

temperature of 22 °C. The fluid is collected by a sump below the jet and the fluid is pumped back into the reservoir. The flow rate is maintained by ensuring that the fluid volume in the reservoir is constant, achieved by a pressure controller (MJ-E-130, Microdrop Technologies GmbH) and a gear pump with fine speed control, to re-introduce fluid into the reservoir at an appropriate rate. A reservoir pressure of 36 kPa gives a speed of 6.3 m/s.

The jet is positioned horizontally using a pair of crossed linear translation stages (Thorlabs) with a precision of 1 μm, and vertically using a rack and pinion system (Newport) with a precision of 100 μm and a travel of 50 mm. The dispenser head contains a valve designed to turn the jet on and off. A TTL signal is applied to the valve with a frequency of 8-10 kHz. A high TTL signal causes the valve to open fully but it only partially closes when the TTL signal is low because the response time of the valve is slower than the rate of change of the signal. The result is a periodic perturbation to the jet, which not only gives a stable and reproducible breakup length but also provides a trigger signal locked to the periodicity of the jet which can be used to provide phase-averaged datasets. The jetted fluid was ultrapure water (Milli-Q A-10, Millipore; resistivity >18 MΩ), seeded with 1 μm polystyrene spheres. Before any experimental run, the apparatus is completely disassembled and all the parts are soaked overnight in a 2 % detergent solution (Decon 90, Decon Laboratories Ltd.). The parts of flow system are thoroughly rinsed individually then reassembled. The assembled flow system is then rinsed with ultrapure water several times.

5.3 Method

Once the flow system is cleaned and assembled, holograms are recorded with the holographic microscope described in Chapter 3. A single instantaneous measurement comprises a pair of holograms recorded a short time apart, to facilitate cross-correlation analysis. The programmable timing unit supplied with the commercial PIV system (LaVision Flowmaster) allows the illumination and recording to be synchronised to the signal used to perturb the jet. A delay box allows the recording time to be delayed relative to the perturbation signal if desired.

As described in section 1.2.4.1, holographic PIV calls for a relatively low seeding density to avoid corrupting the data with speckle noise; therefore, multiple pairs of holograms are recorded for each area/time of interest and combined to give a phase-averaged velocity map with higher resolution and better statistics. Holograms of jets are recorded in sets of 40 pairs of exposures, giving a good balance between computational time and number of recorded particles.

Once a run of experiments has been completed, the raw holograms are processed using the numerical methods described in Chapter 4, resulting in an estimate of the amplitude and phase of the field inside the samples. These records of the field inside the sample are saved for later analysis to extract the velocities of the seeding particles.

5.4 Velocimetry Analysis

Once the field inside the sample has been estimated, the next step involves determining the movement of particles between the first and second exposures. This in itself is a multi-step process. First the background light must be subtracted from the field data so that particles may be detected easily, secondly particles must be detected and finally, the shift of particles between the first and second exposures must be registered. Given that the time interval between the individual frames of a pair of exposures is an input in the camera control software, the velocity of a particle is easily calculated from its displacement. The following three sub-sections describe the three stages in obtaining particle velocities.

5.4.1 Background Subtraction

A background subtraction method was developed to aid in particle detection. Given that there is a significant computational time in recombining a single hologram to give images of particles inside a sample, the more particles that can be reliably detected, the fewer instantaneous measurements are required to build up an averaged velocity map

with good resolution. We first consider the appearance of a plane inside a recombined sample (figure 5.2).

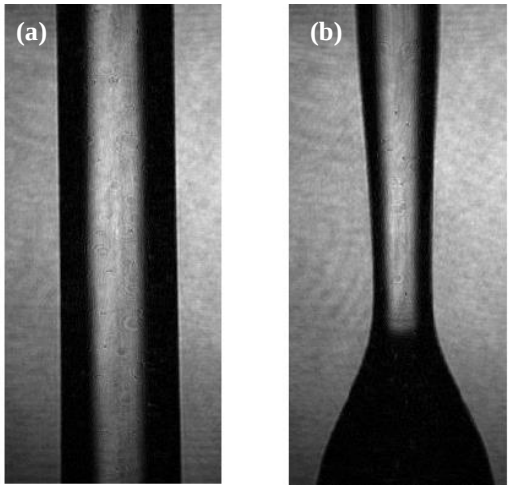

Figure 5.2 The areas of a cylindrical (a) and necking (b) jet where background light is present inside the sample.

Planes contain at least one contiguous area with high intensity light and the remaining area of the sample appears dark in comparison. This region of high intensity corresponds to the laser light that not only illuminated the sample but also was refracted by the sample towards the camera. Particles in this region appear as dark spots on a bright background. Close to the sides of the sample, particles are not illuminated at all as all of the light is refracted towards the centre.

The behaviour of light in samples with a constant radius has already been discussed (section 3.1), and the distribution of illumination light estimated by ray tracing analysis has been given in figure 3.1. Over the circular cross-section, particles can exist in one of three environments (figure 5.3): (A) close to the sample edges where the particles are not directly illuminated by the laser and therefore do not scatter an appreciable amount of light, (B) closer to the centre where particles are directly illuminated and scatter light in the direction of the detector, however, the unscattered illumination light does not contribute to the holograms due to refraction at the front surface of the sample, and (C) in a central portion (the bright streak in figure 5.2) where particles scatter light and any unscattered light contributes to the recorded hologram.

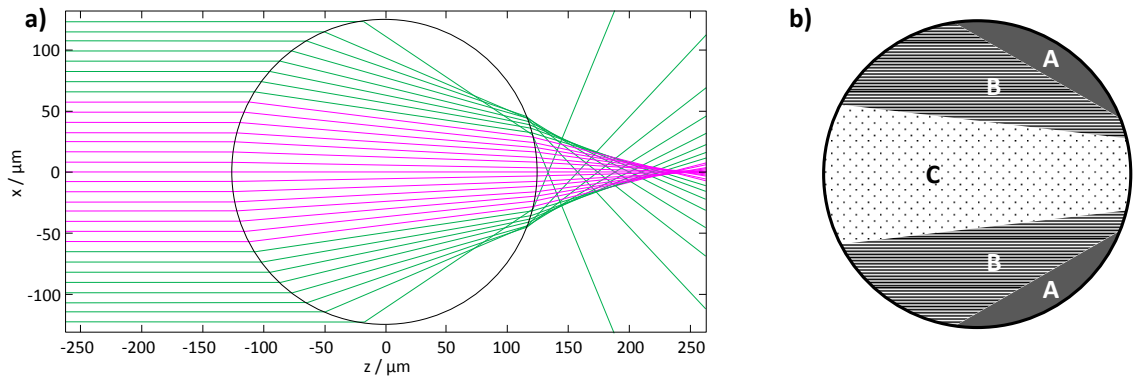

Figure 5.3 Ray tracing through a circular cross section (a), the magenta rays are rays which go on to strike the detector and the green rays do not strike the detector. (b) A sketch highlighting the three possible particle environments inside a circular cross section.

One possible approach to particle detection could be to constrain the search to the bright regions and find local minima. This approach would work for a cylindrical sample, resulting in no loss of unique velocity data, as so long as one full strip from front to back of the jet is interrogated, the axisymmetric approximation will yield a velocity map with no gaps in either the radial or stream-wise direction. In the case of a sample with a varying cross section (figure 5.4), a significant portion of the image is dark, and an approach sensitive only to particles in the bright regions would result in gaps in the final velocity data.

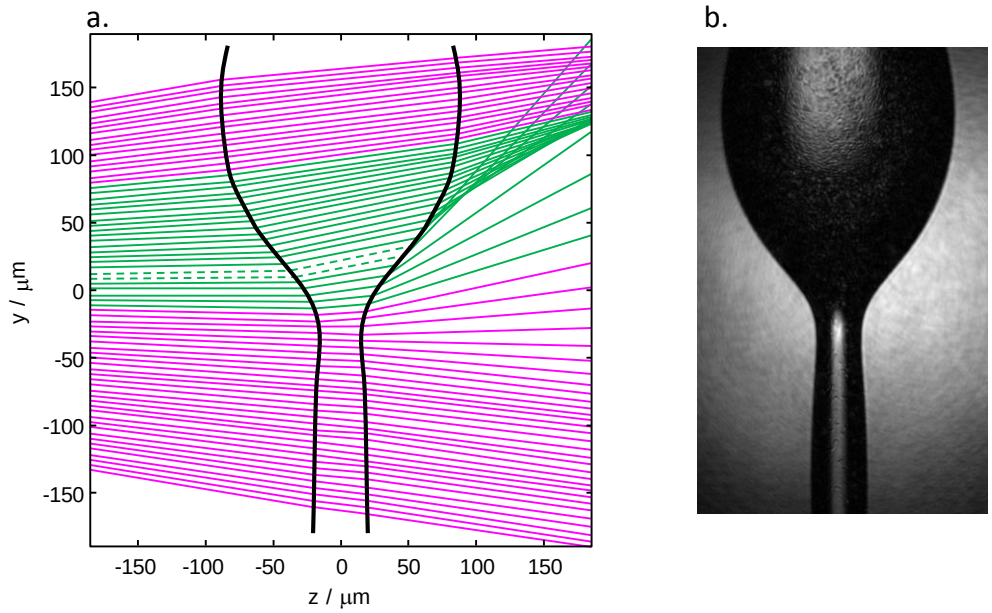

Figure 5.4 a) Ray tracing analysis of a radial section of a swell and a neck – based on refraction of light emanating from a realistically placed source (-1 mm in z) through an experimentally measured jet profile. The solid lines are rays which pass through the sample, coloured in magenta if the ray would strike the detector and green if it would not. The dashed lines are rays which totally internally reflect. b) An image of the sample from which the surface was measured – focused approximately on the plane $\boldsymbol{z = 0}$.

With the intention of detecting particles in both conditions, three background subtraction methods were considered for use on the recombined fields inside samples: (1) local average subtraction (intensity only), (2) subtraction of an averaged background and (3) a spatial filtering operation. Local average subtraction is commonly used in μPIV analysis to enhance the contrast of particles from their surroundings.[1] A simple local average subtraction method was written in MATLAB to work on the 3D field data but it was found to be inappropriate, as a local average subtraction only works well if the background is smoothly varying, and introduced artefacts close to the edges of the bright regions.

The average background subtraction is another common method[1] and requires averaging many particle fields to give a uniform average background. This method was found to be expensive computationally and overly sensitive to pulse-to-pulse intensity variations in the laser illumination.

The final method, a spatial filtering operation, was found to work most effectively and, as such, was applied within this work. Spatial filtering removes spatial frequencies in

the data corresponding to the background light. The operation itself is performed only on a single plane, and from the single filtered plane the rest of the region can be generated (using the propagation methods already discussed). The concept behind the spatial filtering operation is that the light scattered from particles (desired) will diverge as the plane is propagated back towards the illumination source, whereas the background light (undesired) will converge to a focus. The focus provides a convenient point to remove the background light without greatly affecting the light scattered from particles as it is more-or-less evenly spread over that plane. Optical spatial filtering as a method to remove the background light between particles has been used since the early days of PIV.[2] The spatial filtering method provides a means by which all particles stand out as intense spots on a dark background, while retaining phase information. Examples of how particles appear before and after background subtraction are shown in figure 5.5 and figure 5.6. Particles in both the areas where the illumination light is recovered (figure 5.5) and where it is not (figure 5.6) appear as bright spots on a dark background – making particle detection simpler as well as reducing artefacts in correlations, caused by local variations in the background light. The correlation analysis is discussed in the next section.

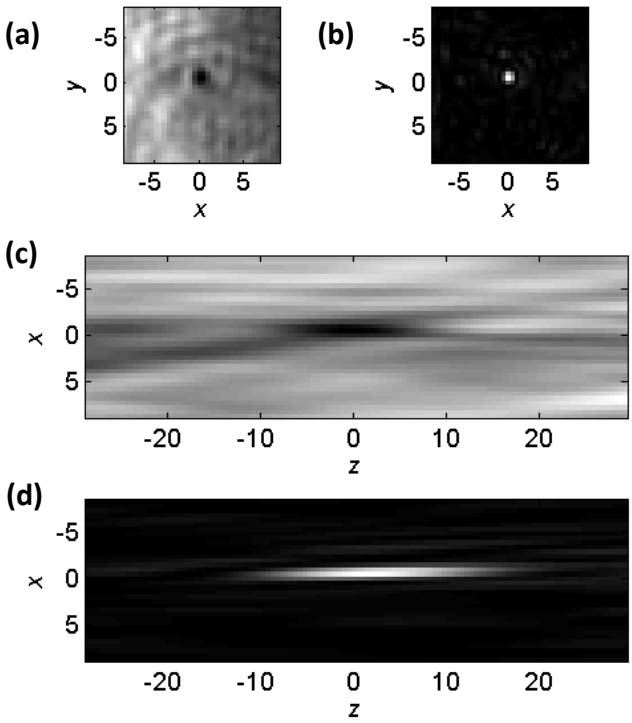

Figure 5.5 Sections through a particle intensity profile before background subtraction ((a) and (c)) and after background subtraction ((b) and (d)). The particle lies in the bright part of the reconstruction. The scale on all images is in micrometres.

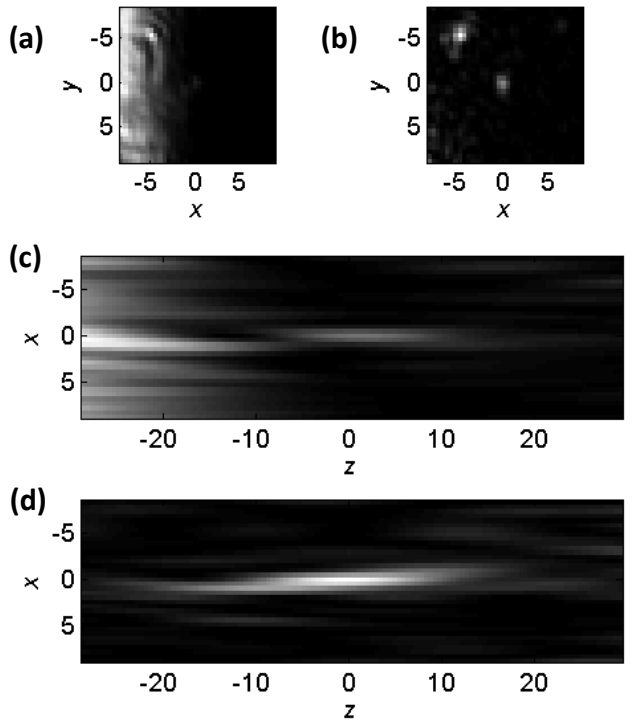

Figure 5.6 Sections through a particle intensity profile before background subtraction ((a) and (c)) and after background subtraction ((b) and (d)). The particle lies in the dark part of the raw image. The scale on all images is in micrometres.

5.4.2 Correlation Analysis

Wormald and Coupland compared the performance of three different means of measuring particle displacements: nearest neighbour analysis, correlation of intensity and correlation of complex amplitude.[3] They found that correlation of complex amplitude achieved more reliable results and this is the method of analysis I used in this work.

Cross-correlation analysis is a familiar tool in PIV, commonly used to measure the displacement of groups of particles recorded in separate images. One is typically interested in local velocities in particle velocimetry, so images are broken up into small correlation windows. The cross-correlation, $\mathrm{R}_{\mathrm{U1-U2}}(\boldsymbol{r})$, of two complex functions $\mathrm{U}_1(\boldsymbol{r})$ and $\mathrm{U}_2(\boldsymbol{r})$ can be written:

$$\mathrm{R}_{\mathrm{U1-U2}}(\boldsymbol{r}) = \int_{-\infty}^{+\infty} \mathrm{U}^*{}_1(\boldsymbol{r})\mathrm{U}_2(\boldsymbol{r}-\boldsymbol{k})d^3\boldsymbol{k}$$

where $*$ denotes the complex conjugate. In a numerical environment, U_1 and U_2 are finite and finitely sampled arrays of complex field data – each contains the same particle in a different position. The result of the cross-correlation is another complex array with a maximum in its absolute value corresponding to the shift between the two images.

Complex cross-correlation analysis was performed using self-written MATLAB code. Working on the background-subtracted data, first particles are detected in the first exposure, appearing as sharp dips in the imaginary part of the complex field. The particle detection routine simply searches for local minima in the imaginary part of signal. Detected particle coordinates are filtered to ensure that no particle is found twice and correlation windows are centred on the detected particle coordinates. Correlation windows are volumes of 16 × 16 × 32 voxels (7.8 × 7.8 × 15.6 $\mu\mathrm{m}^3$). The cross-correlation itself is implemented taking advantage of the fact that it is a special case of a convolution[4] using fast Fourier transforms (FFT). The results of cross-correlations are arrays of the same size with a peak at the integer pixel shift – sub-sample resolution is achieved by locating the centre of the peak with a quadratic fit. An example of two correlation windows and their cross correlation is shown in figure 5.7. The results

gained from applying correlation analysis to reconstructed images of particle fields in a continuous inkjet and the results are shown in the next chapter.

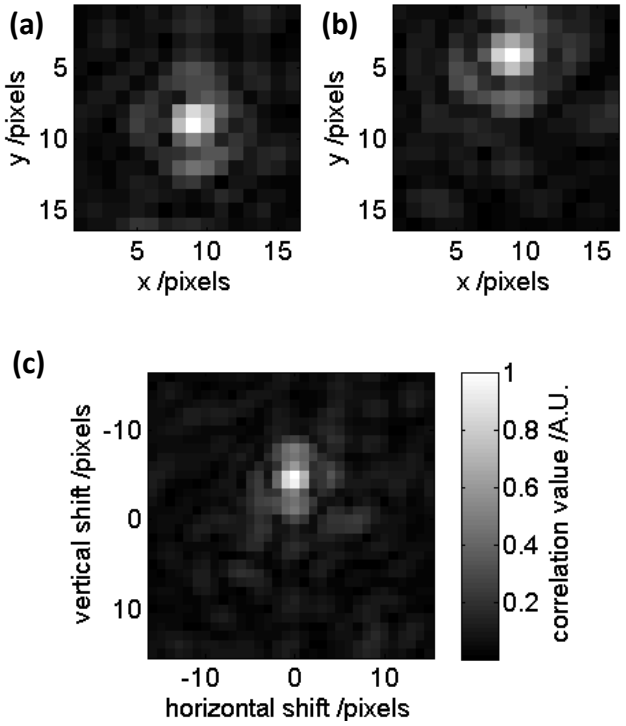

Figure 5.7 Correlation windows from the first (a) and second (b) exposures and the result of their cross-correlation (c).

5.5 Conclusion

In this chapter, I have described the fluidic system used to create the jets which were measured using the microscope described in Chapter 3. I have also described the experimental procedure and the method used to analyse 3D reconstructions to measure the internal velocity in the ink jet streams. The following chapter presents and discusses the velocity data obtained from jets of water.

5.6 References

1 M. Raffel, C. Willert and J. Kompenhans, *Particle Image Velocimetry. A practical guide*, Springer-Verlag, Berlin, 2nd edn., 1998.

2 C. S. Yao, R. J. Adrian, 1984, *Appl. Opt.*, 23(11), 1687-1689.

3 S. A. Wormald, J. Coupland, 2009, *Appl. Opt.*, 48(3), 6400-6407.

4 J. W. Goodman, *Introduction to Fourier Optics*, Roberts & Company, Colorado, 3rd edn., 2005.

6 Velocity Profiling During Break Up of a Continuous Ink Jet

This chapter presents the velocimetry results obtained inside a continuous ink jet stream. First, measurements inside a cylindrical stretch of the jet are used to validate the technique before results are presented showing that velocity can be measured inside parts of the jet which swell and neck. The final set of results explores how close to the point of breakup of the jet it is possible to measure.

6.1 Validation

This section describes how the raw output of the correlation analysis is used to produce velocity maps and assess the validity of the results.

6.1.1 Vector Processing

The correlation analysis gives a set of particle shifts (their displacements between exposures) along with the Cartesian coordinates of each particle's location in the first exposure. Each dataset of 40 exposures contains information relating to 2000 – 3000 individual particles. Assuming that the flow in the jet is axisymmetric, the Cartesian coordinates of the particles are converted into polar coordinates (figure 6.1). The y-coordinate remains unchanged whilst the x- and z- coordinates are converted into an absolute distance from the axis of symmetry of the sample, forming the radial coordinate r. The velocity vectors also require some preliminary processing from raw displacements $(\Delta_x, \Delta_y, \Delta_z)$ into velocities (u_x, u_y, u_z), simply by multiplying by the inter-frame time. The velocity vectors must also be converted into a polar form, i.e. the components of velocity parallel and perpendicular to the axis if symmetry (u_y, u_r). The

axisymmetric approximation implies that the components of velocity u_y and u_r are independent of the polar angle and that $u_\alpha = 0$.

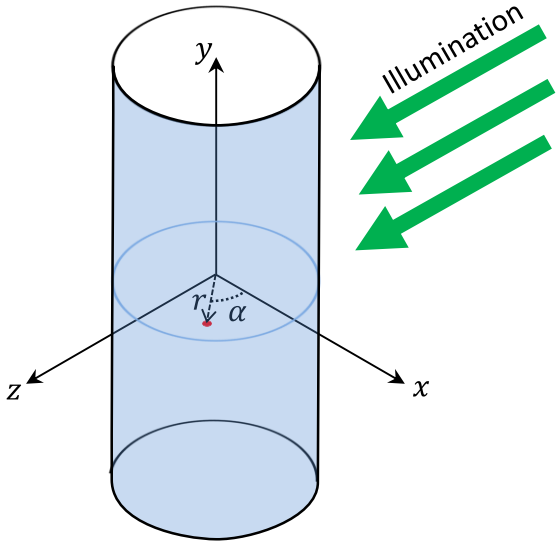

Figure 6.1 The Cartesian and polar coordinate systems inside the sample.

The vertical speed, u_y, remains unchanged by the coordinate transformation and, for the time being, we consider only that component. The radial component of velocity will be considered later in this chapter. Once the data is in cylindrical polar form, containing of the order of 10^3 records of vertical speed scattered over a space, the particles are grouped into regular bins in both the radial (r) and axial (y) directions bins respectively. In the case of a cylindrical stretch of jet, 20 radial bins over the range 0 μm < r < 50 μm and 10 axial bins over the range -150 μm < y < 150 μm were selected. Where the jet begins to swell and neck, the radial velocity is more constant and the axial velocity changes more rapidly, here the number of axial bins can be increased at the expense of fewer radial bins. Any vector in disagreement with the others in the bin is rejected and any bin containing less than 3 vectors is discounted. At this point only the vertical speed is of interest so the angle of the vector is not taken into account in the filtering, a vector is said to be in disagreement when its absolute vertical speed differs from the mean by more than 50 % of the mean speed in the bin. The purpose of the filtering operation is to

prevent the few clearly erroneous vectors from skewing the result. The filtered vectors are then averaged to give an average speed at the centre of each bin.

As the flow inside the continuous ink jet is axisymmetric,[1] any deviation from this in the data will highlight an error introduced by the processing. A check for such a deviation was performed by separating the azimuthal coordinate into two sets, the front (towards the camera) and back (towards the illumination) halves of the jet. Figure 6.2 shows the change in speed with radial coordinate. For each bin in the radial direction a histogram is given, with the colour scale showing the distribution of the vertical speed of velocity vectors within that bin. There are two notable features in the histogram, the first is that the distribution is bimodal and the second is that the vertical speed is not independent of radial position – we will discuss the second feature later in this chapter. The first feature is an experimental artefact, in the following paragraphs I describe how I identified the cause and corrected it.

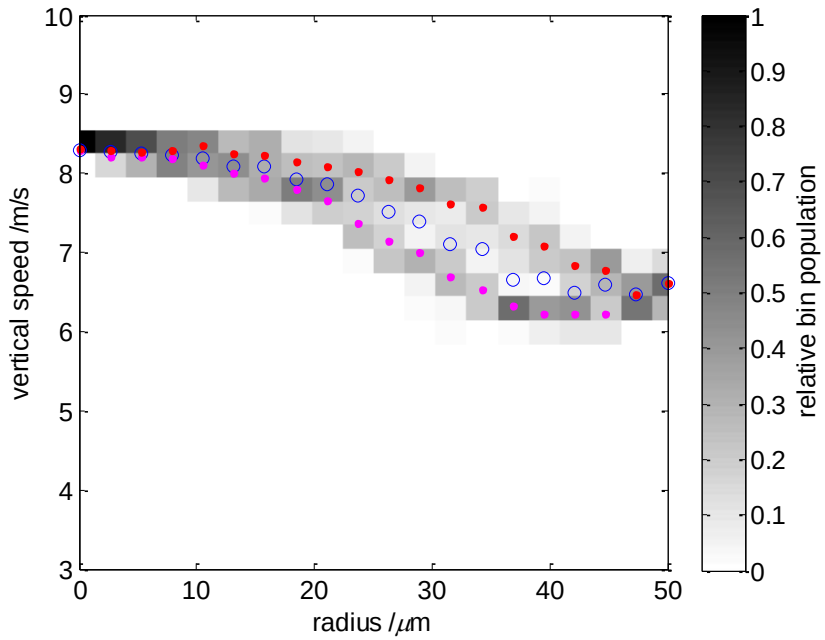

Figure 6.2 Preliminary radial profile of a jet flowing at 7 m/s, measured 700 μm downstream from the nozzle. Each column shows a histogram of the vertical speed of the jet. The blue circles show the mean velocity obtained from averaging over the full angular range at each radial bin, the red markers show the result obtained from averaging vectors from only the front half of the jet and the pink markers are the result of averaging over only the back half of the jet.

The histograms show that, for a given radial coordinate, about half of particles travel at one speed and about half at another, for most radial coordinates. The superimposed solid markers on figure 6.2 show the mean velocity at each radial coordinate averaged over different angular ranges – specifically the front (towards the camera) and back (towards the illumination) halves of the jet. Where distributions are bimodal, one peak corresponds to the front half of the jet and one to the back. This problem, observed in most preliminary datasets, arises from a small (less than the axial resolution of the microscope) error in positioning the front surface of the sample. If the holograms are reprocessed from scratch, shifting the sample by 5 μm along the optical axis, the histogram shown in figure 6.3 is obtained.

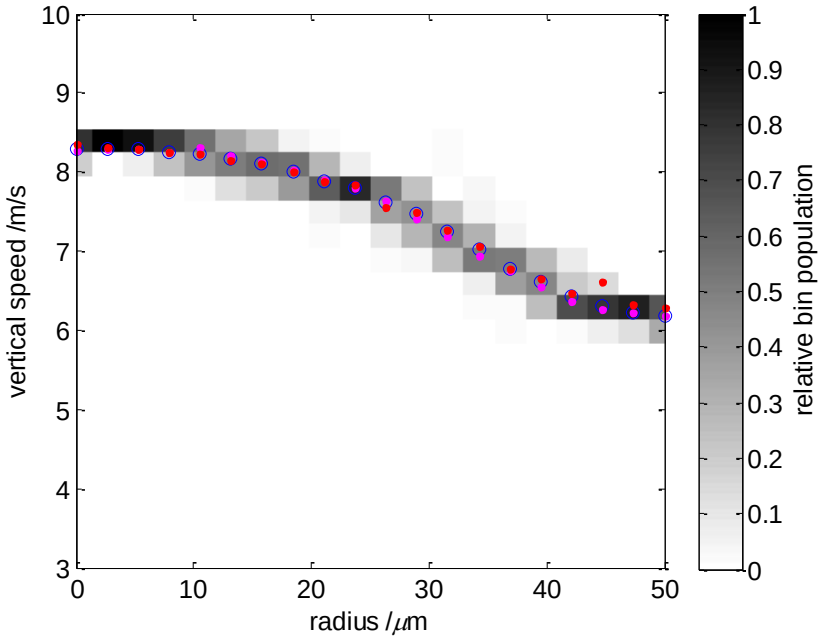

Figure 6.3 Radial profile, after correcting the sample position. The sample is a jet flowing at 7 m/s, measured 700 μm downstream from the nozzle. Each column shows a histogram of the vertical speed of the jet. The blue circles show the mean velocity obtained from averaging over the full angular range at each radial bin, the red markers show the result obtained from averaging vectors from only the front half of the jet and the pink markers are the result of averaging over only the back half of the jet.

I believe that the error manifested in the original dataset was caused largely by the uncertainty in the conversion of the particle positions from Cartesian to polar coordinates – specifically the error in locating the centre position of the axis of symmetry in the z direction. The same effect can be seen in synthetic data (figure 6.4).

In this instance, the centre has been offset from the axis of the jet and the results appear similar to those observed in the real data.

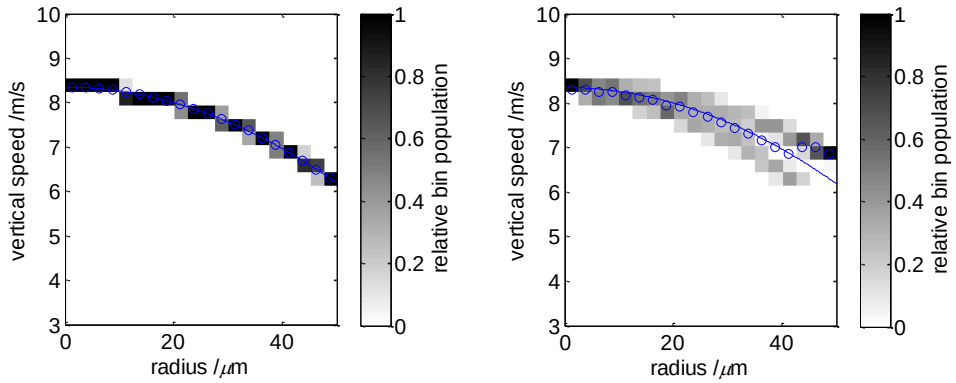

Figure 6.4 The effect of a small error in the position of the centre when converting coordinates on model data.

To generate the synthetic data a randomly distributed field of particle coordinates was generated, and each particle was assigned a vertical speed by

$$u_{\mathrm{synth}}(r) = -\frac{u_{\max} - u_{\min}}{\mathrm{R}^2} r^2 + u_{\max}, \tag{6.1}$$

where r is the particles true radial coordinate, $u_{\max}$ and $u_{\min}$ are the maximum and minimum velocities respectively inside a sample with radius R. Particles were also assigned an erroneous radial coordinate, r_{err}, given by

$$r_{\mathrm{err}} = \sqrt{x^2 + (z - \varepsilon_z)^2}, \tag{6.2}$$

where ε_z is the error in the location of the sample centre in the z direction. Figure 6.4 shows the histogram produced using the modified radial coordinate with $\varepsilon_z = 8\ \mu$m. The figure indicates that simply averaging at each radial position gives the correct answer. Close to the centre, averaging gives a slight underestimate of 0.7 % but close to the edges, the average is an overestimate of 9 %. The error associated with incorrect positioning of the sample surface is avoided by first processing a small number of hologram pairs, assessing whether the surface needs to be shifted and running the whole dataset with the correct surface position.

To confirm that an error in the positioning of the sample gives rise to the mismatching velocity profiles between the front and back of the sample, light was propagated through both sides to reconstruct the original illuminating focus – the same analysis that was described in section 4.5.1. This analysis yields two results, the first showing that the position of the reconstructed focus along the optical axis was unaffected (to within 1 μm) by errors in positioning the sample of up to 5 μm. The largest effect observed concerned the sharpness of the focus, with the position which yields the most symmetric velocity profile giving a focus with a 60 % higher maximum intensity than the erroneous initial estimate. It is reasonable to assume that, if the sample is in exactly the correct position in the reconstructions, aberrations disappear and the focus is sharpest; for this reason I believe that the shifting the sample is justified and that the source of the mismatch between the front and back of the sample arise from a small error in locating its position.

Incorrect sample location is caused during the initial reconstructions since the edges appear sharp over a range of positions along the optical axis. Figure 6.5 gives a top-down view of a slice through a stack of reconstructed planes. Note that, in this image, the change in refractive index has not yet been accounted for, it is only for the purpose of showing the smoothness of the change in the appearance of the edges of the jet with distance along the optical axis. The lines on the figure show the centre line of the sample in both the erroneous and correct reconstruction. A plot of the intensity across each line (figure 6.6) shows how similar the edges are at each plane.

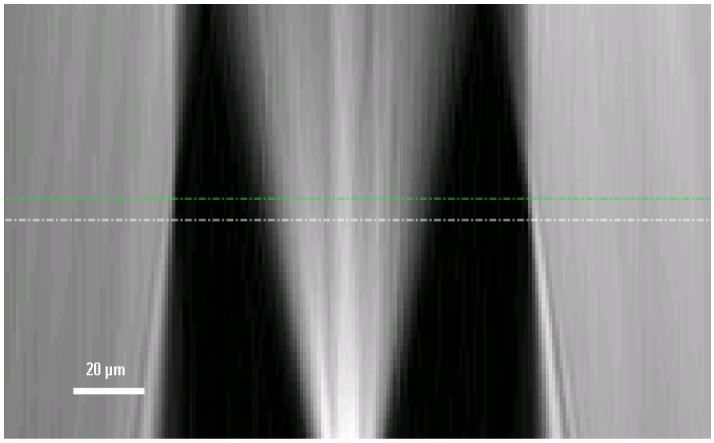

Figure 6.5 A slice through a stack of reconstructed planes at different distances along the optical (***z***) axis; ***z*** varies in the vertical direction on the figure, illumination comes from above. The white broken line shows the central plane of the initial estimate of the sample position and the green broken shows the postion of the refined estimate.

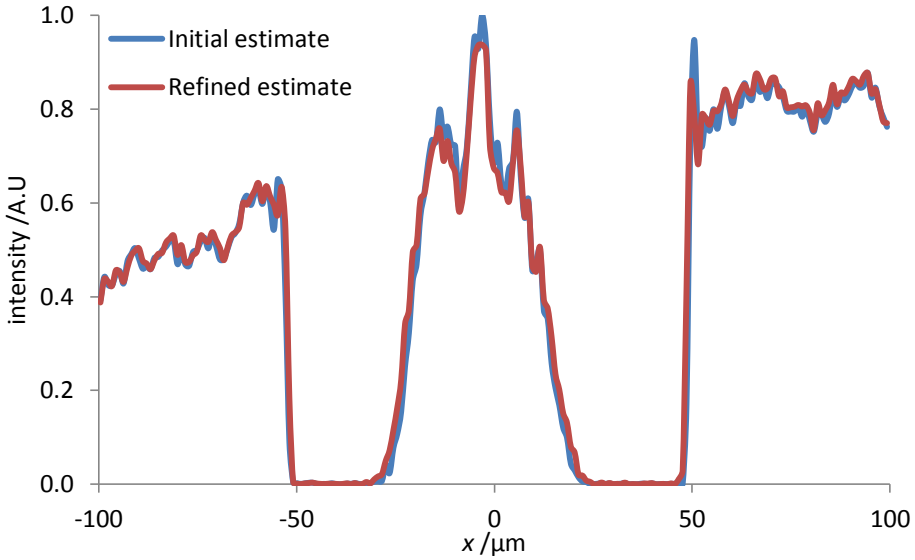

Figure 6.6 The similarity in change in intensity across a sample for both the initial estimate of the sample's position and the refined estimate.

Given the similarity in the change in intensity across the sample edges, it is to be expected that there is an error in the location of the sample to a necessary level of precision, however, by examining a preliminary set of velocity profiles, the error can be found and corrected for.

6.1.2 Experimental Parameters

There are two main parameters that can be adjusted in a particle velocimetry experiment, the particle seeding density and the time delay between the laser pulses (Dt). The particle seeding density needs to be low in holographic PIV to avoid noise due to multiple scattering and speckle noise. Correlations of holographic PIV data can be affected by the light from particles other than the one being interrogated – in these experiments it is this problem that sets the lower limit. So that particles are on average separated from their nearest neighbours by a distance larger than the dimensions of the correlation windows, I have chosen seeding densities which correspond to 50 – 100 particles per frame. This seeding density, allows 3000 vectors to be calculated in a total time of less than 2 hours (Intel Core i7-3770 3.4 GHz) which yields sufficient data to build up an averaged velocity map with 15 bins along the radial coordinate and 15 along the axial coordinate, with each bin averaging over at least 10 particles.

The effect of increasing the inter-frame time, Dt, is that particles move farther between exposures. In PIV experiments it is assumed that particles do not change velocity during the time between frames – so naively, it seems as though the smallest possible Dt would yield the highest quality data. However, the movement of particles between frames must be large enough so that the shift can be detected to a good degree of accuracy. It is typical in PIV to assume that the shift can be measured to a precision of 0.1 pixels.[2] The greater the shift of the particle between images, the smaller the percentage error on its mean velocity between the two exposures. Another limit is applied to Dt in that the particle must look similar in both exposures to get a reliable output from the correlation. In these experiments as the flow inside the jet is periodic, it was deemed reasonable that the inter-frame time should be no longer than 1 % of the jet period (0.5 – 1 μs) with a shorter inter-frame time better for correlations. The mean velocity from correlation analysis is compared to the known mean velocity for two different inter-frame times in the next section.

6.1.3 Mean Velocity

It is useful now to look at a flow profile obtained in a cylindrical section of the jet. In the first ~2.5 mm from the nozzle, the jet is effectively cylindrical with a velocity profile that gradually relaxes towards plug flow – i.e. the velocity does not depend on radius. For the time being, we are not concerned with the shape of the profile itself; the aim here is to compare the average velocities obtained to the average velocity measured by another method. Mean jet velocity is measured at the time of experiments by recording the time taken to jet 10 ml of liquid. The volume flow rate (Q) can be estimated from the radial flow profiles ($u(r)$) provided by the correlation analysis with the following integral, assuming the flow is independent of the polar angle, α (figure 6.1),

$$\mathrm{Q} = 2\pi \int_0^{\mathrm{R}} u(r) r \mathrm{d}r$$

where r is the radial coordinate. Dividing by the cross-sectional area, an expression for mean velocity ($\bar{u}$) is obtained

$$\bar{u} = \frac{2}{\mathrm{R}^2} \int_0^{\mathrm{R}} u(r) r \mathrm{d}r$$

where R is radius of the jet. Table 6.1 compares the holographically measured flow rates for different stream-wise measurement positions, and a speed measured by the volume of fluid collected over a known time. The errors in both values are dominated by the uncertainty in the jet radius equal to the transverse resolution in holographic reconstructions.

Table 6.1 Comparison of mean flow rate at different positions and inter-frame times.

Mean velocity by volume flow rate /m s^{-1}	Dt / μs	Downstream distance /μm	Mean velocity by HPIV /m s^{-1}
6.31 ± 0.13	0.5	700	6.34 ± 0.13
6.31 ± 0.13	0.5	1700	6.29 ± 0.13
6.31 ± 0.13	0.5	2700	6.36 ± 0.13
7.06 ± 0.14	1.0	700	7.04 ± 0.14
7.06 ± 0.14	1.0	900	7.08 ± 0.14
7.06 ± 0.14	1.0	1100	7.07 ± 0.14
7.06 ± 0.14	1.0	1300	7.07 ± 0.14

The results measured by holographic velocimetry and by the volume flow rate approach are in agreement within error. The agreement suggests the measured velocities reflect the real behaviour of the fluid inside the jet.

6.1.4 The Radial Component of Velocity (u_r)

The extraction of the radial component of velocity is not straightforward due to its small magnitude compared to the mean vertical speed, $\bar{u}_y$. In the best case, velocity is measured to the same absolute error in both the radial and axial directions, and therefore if the absolute velocity is an order of magnitude lower in the radial than axial direction, the percentage error is an order of magnitude higher. There is no reason however why the absolute error should be equal in both the radial and axial velocity measurements. Particle images, while relatively sharp points in the xy plane are somewhat extended in z (along the optical axis). This is an intrinsic property of numerical aperture limited recording. The particle's actual displacement in z is small compared to its extent in that direction and the component of velocity in the z-direction is extremely noisy as a result. The displacements measured and hence the component of velocity, u_z, are unreliable and cannot reasonably be used to calculate u_r.

The measured component of velocity u_x could potentially be used to calculate the radial component. Assuming that the flow is axisymmetric, a simple trigonometric relationship can be used calculate u_r from u_x, it is

$$u_r = \frac{\sin \alpha}{u_x}. \tag{6.3}$$

The limitation with this approach is that towards the axis of the sample, the apparent motion of the particles is very small in the x-direction. The impact of the small apparent motion in the x-direction is shown in figure 6.7. Assuming the sample has a radius of 50 μm, an actual radial component of velocity of 1 m/s and an inter-frame time of 1.0 µs and that particle displacement can be measured to ±0.1 pixels, percentage error in the measured radial component of velocity is plotted against distance from the axis of the sample in the x-direction for particles at different radial coordinates within the sample. The percentage error is proportional to both the absolute error in measurement and the radial position of the particle and inversely proportional to the inter-frame time, the radial component of velocity and the x-coordinate of the particle.

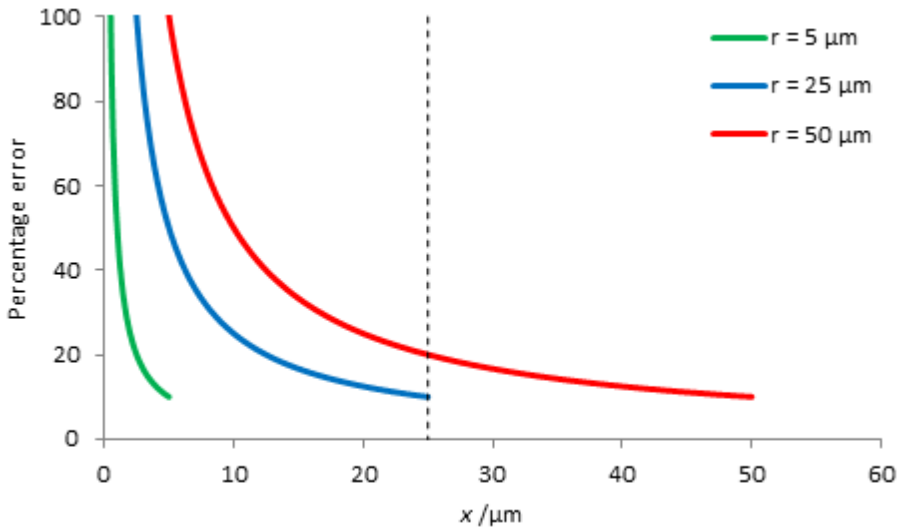

Figure 6.7 The percentage error in the radial component of velocity with horizontal position $\boldsymbol{x}$. The graph shows the error for a particle close to the surface of a 50 µm radius jet with a radial component of velocity of 1 m/s. The red dashed line shows the limit in the x-direction where particles are visible to the particle detection code.

The best case is a particle travelling parallel to the plane of the camera, having only a 5 % error, however this is seldom possible as the measured volume is truncated in the x-direction; only particles in a central stripe 50 μm or so wide are visible to the particle detection software. This limit is marked with the dashed line in figure 6.7. Assuming that particles with greater than 100 % error are discarded by comparison with their neighbours, the average errors in the measured radial component of velocity for the remaining particles detected at r = 5, 25 and 50 μm are 24, 13 and 12 % respectively.

Another option to obtain the radial component of velocity is by using a continuity approach. The continuity equation is based on the conservation of mass, stating that the rate at which mass leaves a volume element must match the rate at which mass enters; in cylindrical polar coordinates the continuity equation is written:

$$\frac{\partial \rho}{\partial t} + \frac{1}{r}\frac{\partial (\rho u_r)}{\partial r} + \frac{1}{r}\frac{\partial (\rho u_\alpha)}{\partial \alpha} + \frac{\partial \left(\rho u_y\right)}{\partial y} = 0, \tag{6.4}$$

where, ρ is the fluid density; the coordinate system has been defined in figure 6.1. By making two assumptions that the jetted fluid (water) is incompressible and that the angular component of fluid velocity is zero, it is theoretically possible to calculate the radial component of velocity (u_r) from the vertical component of velocity (u_y). The process involves differentiating the measured stream wise velocities with respect to the stream wise coordinate and integrating with respect to the radial component. In order for this operation to be successful, data must be very quiet as differentiating can cause any amount of noise to be amplified. When attempted on my data, this was the case and no useful information could be gained.

6.1.5 Conclusions on the Validation

I have shown here that the results obtained from holographic PIV inside cylindrical jet streams are physically reasonable although the measured radial component of the flow is unlikely to be useful.

6.2 Flow in a Cylindrical Stretch of Jet

We have already used the velocity profiles inside a cylindrical stretch of a liquid jet to establish whether the holographic particle velocimetry method yields reasonable results for the mean vertical speed of the jet. In this section, the shapes of the profiles are examined in more detail. Without a computational model of the flow, fully quantitative analysis is difficult, here the data is analysed in a semi-quantitative way.

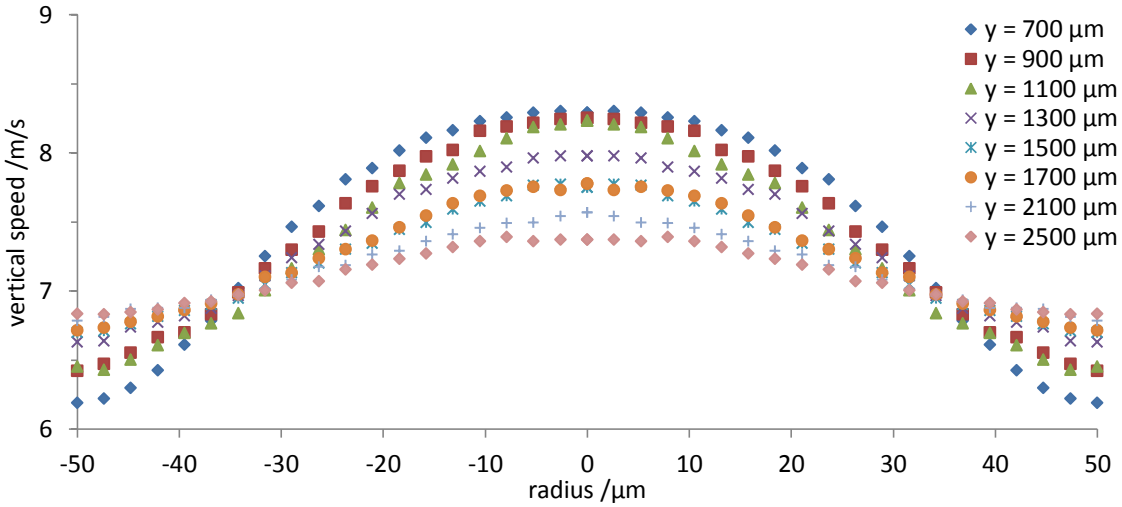

Figure 6.8 Radial velocity profiles inside an ink jet stream with 49.5 µm radius flowing at 7 m/s.

The flow profiles in the cylindrical section of the jet (figure 6.8) show that the flow in the centre is faster than at the sides. This is consistent with the fact that, inside the nozzle, fluid close to the walls is slowed down by friction. At the nozzle exit, ignoring the presence of air, the fluid at the sides of the jet no-longer experiences any drag and momentum diffuses over time from the centre to the sides. Experimental flow profiles farther down the jet show that the flow profile has flattened significantly. In order to establish if this observation is physically viable, it is useful to estimate whether momentum is able to diffuse over this distance in this time.

The time before a system reaches a steady state, i.e. in this case until the flow profile is fully relaxed and velocity is constant with radius can be estimated by

$$t_{\text{long}} \approx \frac{L^2}{\nu} \tag{6.5}$$

where ν is the kinematic viscosity of the fluid and L is the lengthscale of the flow – in this case equal to the jet radius. Equation (6.5) predicts a time of 2.5 ms, which estimates that, at a speed of 7.0 m/s, the flow profile will not have fully relaxed until a distance of 17 mm from the nozzle exit. We therefore do not expect to observe a fully flat velocity profile within the cylindrical stretch of the jet (~2.5 mm long). This is consistent with the experimental observations.

6.3 Velocity Measurements inside Curved Regions of the Jet

As well as in the cylindrical stretch of the jet, velocities have been measured where the jet begins to swell and neck, carrying on all the way to very close to the point where a drop breaks off. The results are shown in figure 6.9, Figure 6.10 and figure 6.11.

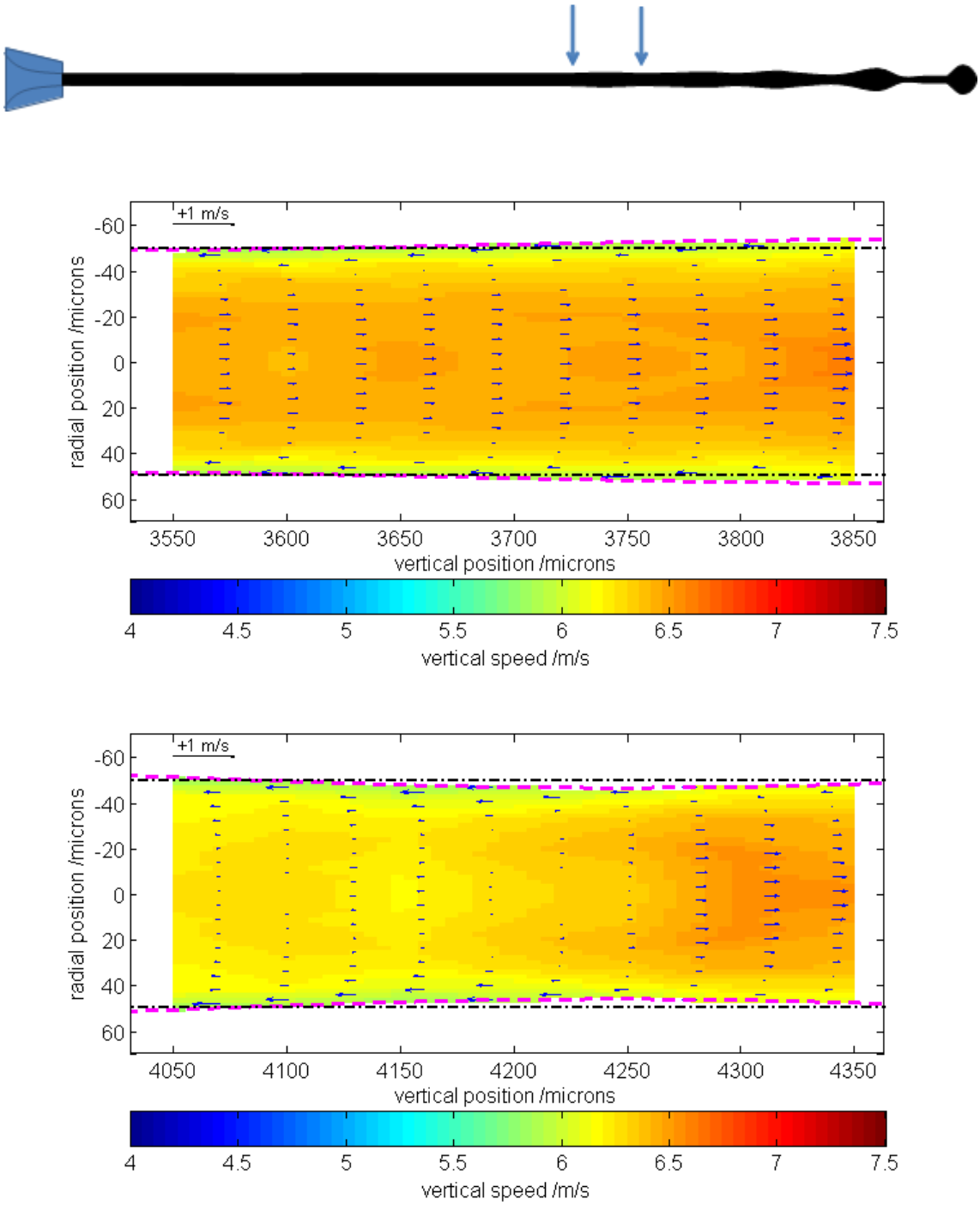

Figure 6.9 Flow inside an inkjet stream 3.7 and 4.2 mm downstream from the nozzle, the mean flow rate is 6.3 m/s. The flow is from left to the right. The colour scale shows the absolute velocity of the jet and the arrows show the local flow speed relative to the mean. The pink dashed lines show the edge of the jet and the black dot-dash lines show the size of the unperturbed jet. Top: a scale drawing of the jet stream with arrows showing the centres of the measured volumes. Middle: the measured flow 3.7 mm away from the nozzle. Bottom: the measured flow 4.2 mm away from the nozzle.

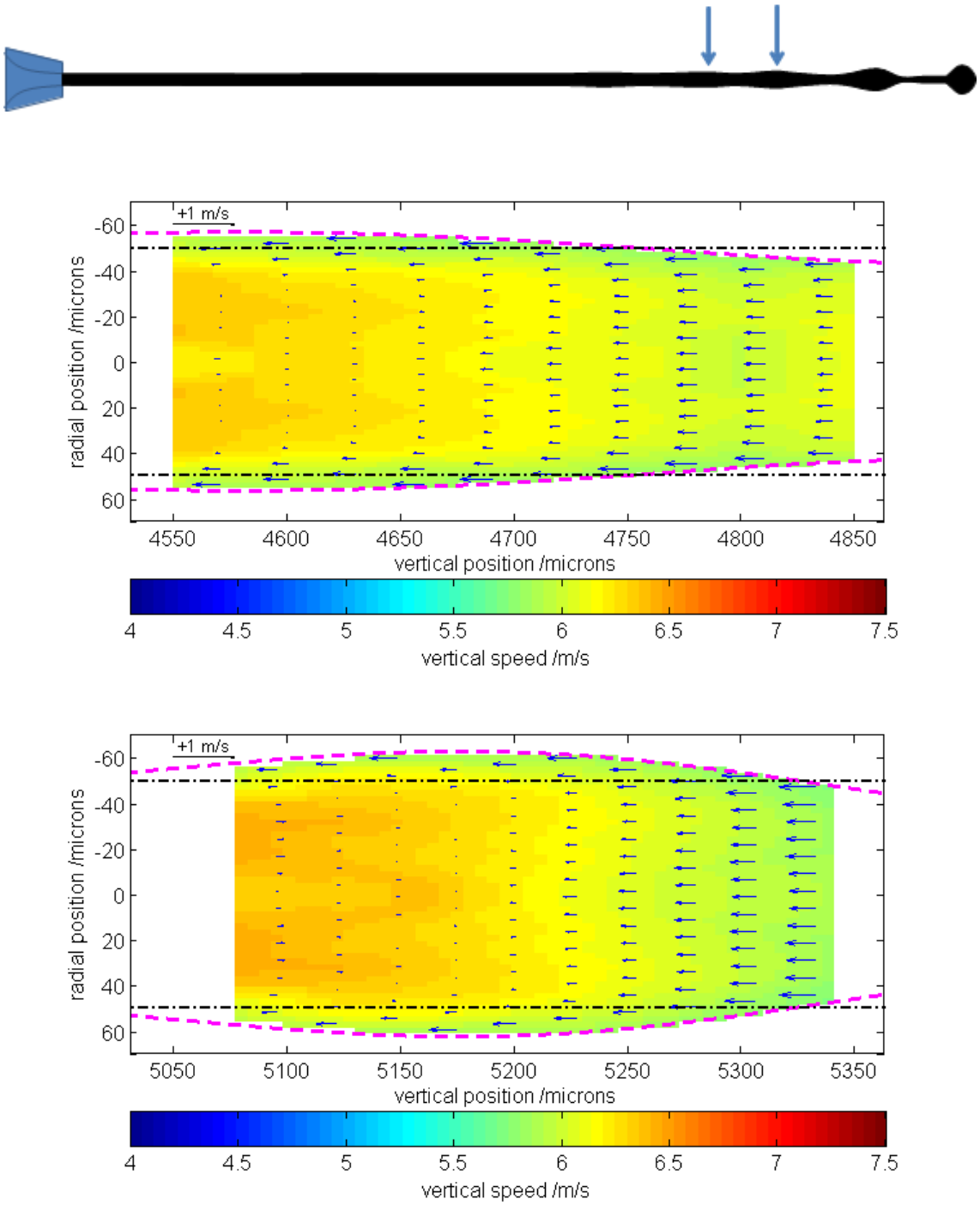

Figure 6.10 Flow inside an inkjet stream 4.7 and 5.2 mm downstream from the nozzle, the mean flow rate is 6.3 m/s. The flow is from left to the right. The colour scale shows the absolute velocity of the jet and the arrows show the local flow speed relative to the mean. The pink dashed lines show the edge of the jet and the black dot-dash lines show the size of the unperturbed jet. Top: a scale drawing of the jet stream with arrows showing the centres of the measured volumes. Middle: the measured flow 4.7 mm away from the nozzle. Bottom: the measured flow 5.2 mm away from the nozzle.

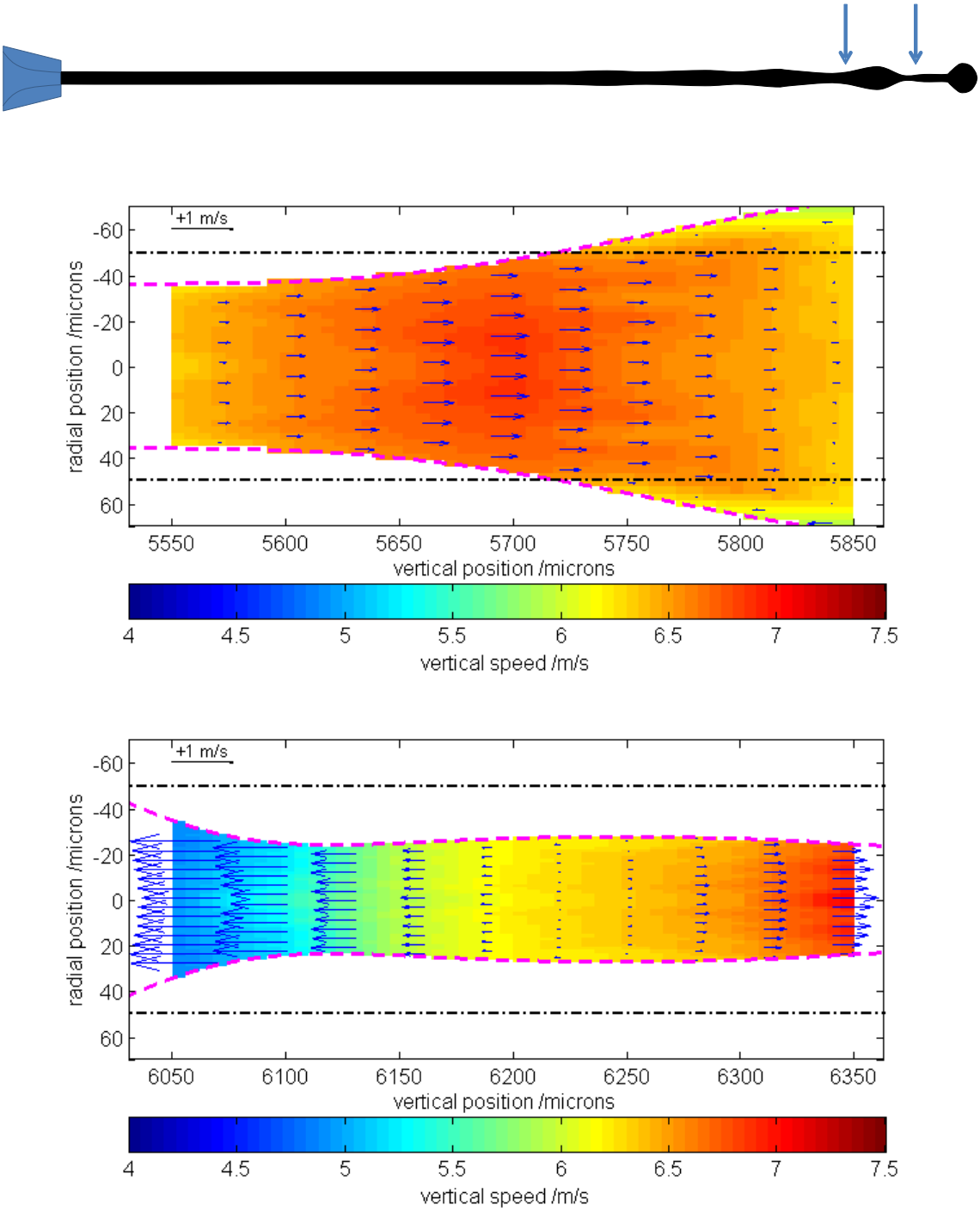

Figure 6.11 Flow inside an inkjet stream 5.7 and 6.2 mm downstream from the nozzle, the mean flow rate is 6.3 m/s. The flow is from left to the right. The colour scale shows the absolute velocity of the jet and the arrows show the local flow speed relative to the mean. The pink dashed lines show the edge of the jet and the black dot-dash lines show the size of the unperturbed jet. Top: a scale drawing of the jet stream with arrows showing the centres of the measured volumes. Middle: the measured flow 5.7 mm away from the nozzle. Bottom: the measured flow 6.2 mm away from the nozzle.

The most useful way to view the velocity inside a liquid jet is from the reference frame of the jet itself – i.e. the jet velocities minus the mean velocity of the jet. The arrows on figure 6.9 to figure 6.11 show the difference in velocity from the mean. Qualitatively, the results appear reasonable, fluid appears to leave the necks (thinner parts) and enter the swells (thicker parts) this is a consequence of Laplace pressure – the driving force behind jet breakup. 6.2 mm away from the nozzle where the jet is thinnest, the rate at which fluid is pumped from the neck into the swells either side is highest.

In the parts of the jet that swell and neck, the radial component of velocity is possibly more relevant and some datasets were recorded with an increased Dt in an effort to increase the accuracy in that component. Results obtained for Dt of 1.0 µs and 2.0 µs are shown in figure 6.12. From the change in the shape of the surface between the two exposures, it is reasonable to suppose that the radial component of velocity was greatest, and directed outwards at the wider end (less than -50 µm relative to the centre of the image), where the jet noticeably dilates during the measurement time. In the thinner part, the jet does get thinner but to a much lesser extent. Some of the vectors in both cases are directed outwardly at the swell, however there are several measured vectors which are in disagreement with this, the reasons for increased noise in measurements of the radial component of velocity have been discussed in section 6.1.4.

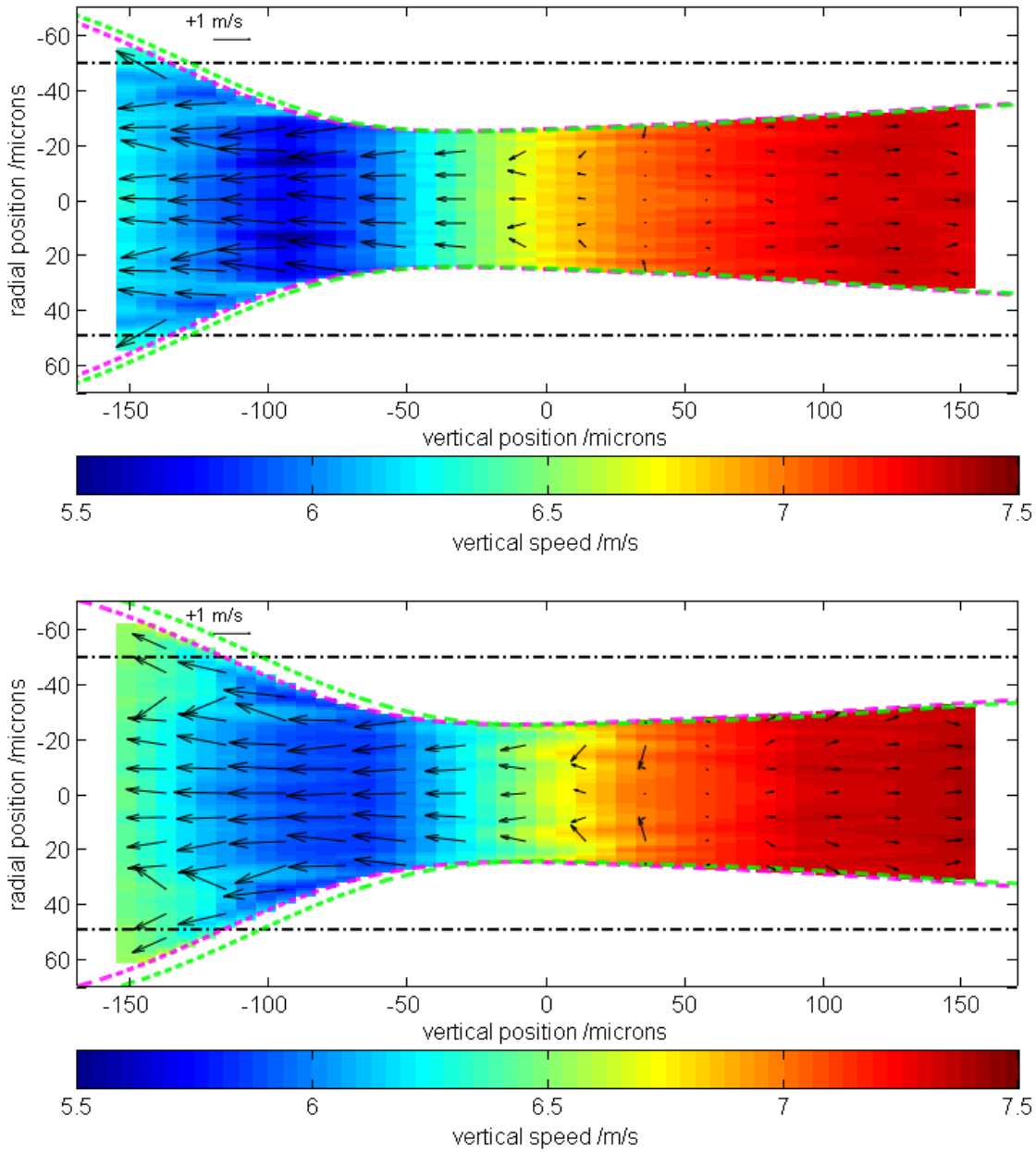

Figure 6.12 Flow inside a neck at two different inter-frame times. The colour scale shows the speed of the jet relative to the static microscope and the arrows show the velocity relative to the mean jet velocity. Both the radial and vertical components of velocity are shown. The dashed pink line shows the edge of the sample in the first frame and the dashed green line shows the position of the surface in the second frame. Top: Dt = 1.0 µs. Bottom: Dt = 2.0 µs.

The most challenging area of an inkjet stream in terms of velocity measurement – and also the most interesting – is the region very close to breakup. Some results are presented in figure 6.13 showing the vectors collected within these regions. The vectors have been superimposed on an image of the jet at the different stages to show the

relative position of the main drop. Shortly before breakup, fluid appears to flow back down the neck toward the following swell but shortly after breakup, the fluid appears to stop almost completely. Given that the extended free ligament of fluid is unfavourable, I expected the flow to speed up as the ligament quickly receded into the following swell. It appears as though, rather than snapping back into the following swell, fluid collects towards the centre of the ligament – presumably the mechanism by which satellite drops are formed. However, in this case no satellite drop is formed as the following swell is able to catch up with and absorb the fluid in the ligament.

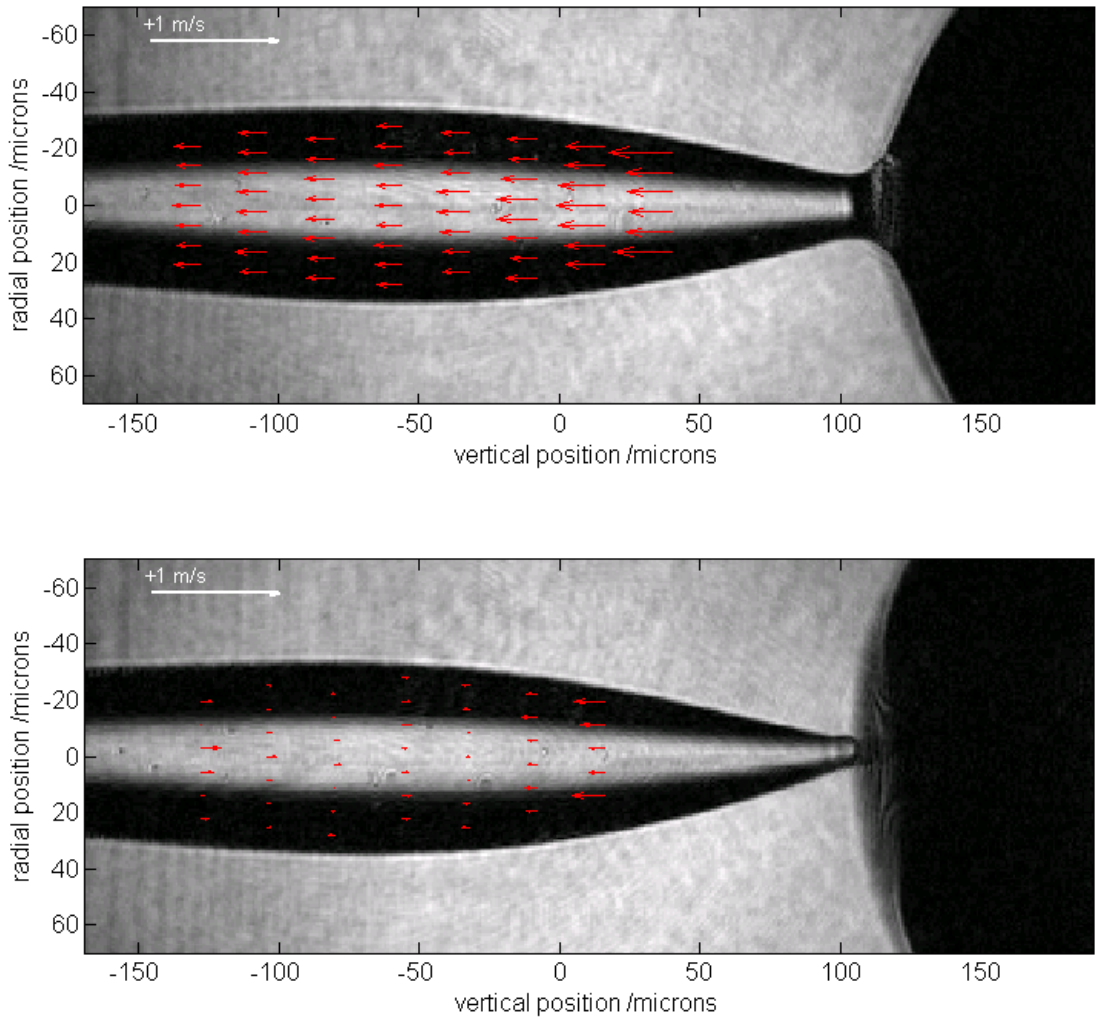

Figure 6.13 Flow inside a jet close to the time of breakup. Superimposed red arrows show the vertical speed relative to the mean jet speed (7.0 m/s). Top: Shortly before breakup. Bottom: Shortly after breakup.

No data is shown in the region where the ligament has thinned below a radius of ~20 μm. Most of the correlations from the particles detected in these regions did not have a sufficient signal to noise ratio to be included. Correlation analysis will fail if particle images are corrupted in one exposure, and there are three reasons why this may be the case where the jet has thinned significantly. Firstly, the reconstruction is more sensitive to the position and shape of the surface applied. The finite resolution of the microscope in the transverse direction results in a relative error in the radius of curvature which is inversely proportional to the sample size. This error will distort particle images and affect the strength of the correlation peak. Secondly, the background subtraction method I employed is based on the assumption that light scattered from particles diverges much more rapidly than the background light around them. This assumption is weaker in the narrower parts of the jet where the back surface acts to focus the light more strongly. The consequence of using the spatial filtering method of background removal in these regions is that some of the information contributing to particle images may be removed as well, resulting in particle images which are less sharp. Finally, because the field inside the sample is generated by propagating a set of finitely-spaced sources on the surface of the sample, as the radius decreases the number of sources contributing to the field inside decreases proportionally. There will, therefore, be fewer unique pieces of information contributing to each particle image, which will increase the amount of noise.

In the following section I will discuss these results in the context of the existing literature.

6.4 Discussion

This section compares the holographic velocimetry method to existing methods in the literature and puts the results into context. The limitations of and potential improvements to the holographic velocimetry technique will also be discussed.

The application of holographic velocimetry to the flow inside ink-jet streams, or any small (micro-scale), tightly-curved flow, has not been reported previously. Wormald and Coupland[3] have reported a proof-of-principle experiment that recovers particle images by the propagation of light through the surface of an inkjet droplet in flight. The work in this thesis uses the same mathematical framework as Wormald and Coupland but a different experimental design. The microscope used in the original experiments (figure 6.14a) was designed for use on microfluidic cells and has completely separate paths for the object and reference beams. The sample is illuminated by a plane wave. The microscope used for the work in this thesis (figure 6.14b) was built for experiments on ink jets, the reference and object beams share the same objective lens. The simpler design reduces cost and delivers diverging wave illumination – increasing the illuminated volume inside curved samples.

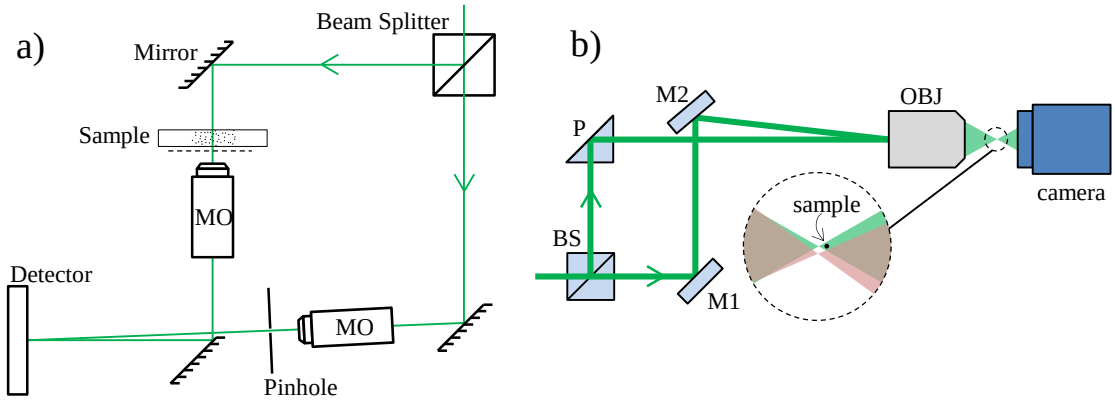

Figure 6.14 The microscope used by Wormald and Coupland[3] (a), and the microscope used for the work in this thesis (b). The microscopes are described in more detail on pages 39 and 99 respectively.

In their paper, Wormald and Coupland proposed a simple method to propagate optical field data, recorded holographically, inside curved samples. The method accounts for refractions at the liquid/air interface allowing particles inside to be imaged. Their paper introduced the mathematical method and included two applied examples where it was used to recover undistorted particle images. The work in this thesis extends their work in a number of ways. The implementation of the underlying mathematics is faster, taking advantage of a 3D convolution method,[4] whereas the original implementation involved a direct numerical integration of the Rayleigh-Sommerfeld equation over the surface of the sample which takes hours rather a minute. A faster implementation improves the applicability of the technique to useful velocimetry analysis where it is desirable to collate results from a number of instantaneous measurements to produce a more finely-grained velocity map. Wormald and Coupland suggested that if the known form of the illuminating wave front could be recovered by propagating the light all the way through the sample then it would be a good method of validating the technique. This validation has been performed in this thesis and has shown that the original wave front can be recovered successfully. Finally, pairs of holograms have been recorded and the movements of particles between the reconstructed 3D images have been measured to produce velocity maps inside a 99 μm diameter ink jet stream. This process involved designing an appropriate background subtraction, particle detection and correlation algorithms. The preliminary velocimetry analysis showed that velocity profiles were sensitive to the position of the surface. An error of ~5 μm in the position of the surface along the optical axis, a tiny fraction (< 0.02 %) of the total distance from the camera to the sample, gives rise to unphysical velocity profiles. This had to be corrected in this work but would go unnoticed in a purely imaging experiment as particle images are relatively insensitive to such a small change. To date, I can find no record in the literature of the use of Wormald and Coupland's method of optical distortion compensation by other groups.

Internal velocities have been measured inside liquid jets ranging in scales from millimetres upwards by the techniques of laser Doppler velocimetry (LDV) and particle image velocimetry (PIV) (with ray tracing-based optical distortion compensation methods).[10,11,15] Recently, the fluid velocity inside a drop-on-demand printed droplet (~ 25 μm diameter) has also been measured indirectly by monitoring the changes in the

droplet shape and assuming plug flow.[5] As well as experimental work, there has also been a great deal of effort put into modelling the flow inside jets.[1,6-8]

LDV is a point-wise measure of one component of velocity whereby two laser beams are crossed at their waist, and the scattering of light from the resultant fringes in the interference pattern provides the signal.[9] As the spacing of the fringes is known (from the wavelength and crossing angle), the component of velocity perpendicular to the plane of the fringes can be easily found from the frequency of the signal. To apply LDV to a curved sample, its refractive index, position and the form of its surface must be known in order to estimate the deflection of the probe (crossing point). In 2003, Battal *et al.* accurately measured the flow inside millimetre-scale liquid jets with LDV.[10] The purpose of the measurements was to provide accurate surface velocities in an investigation into the adsorption of surfactants at expanding liquid interfaces. The measurements were of only the stream wise component of velocity and were confined to the parts of the jet before the onset of breakup i.e. where the jet was still cylindrical. Flow profiles measured inside jets of pure water were in good agreement with a computational fluid dynamics model – the agreement was better in the front of the jet (towards the point of entry of the optical probe) than the back.

As far as I am aware, no LDV results have been published on micro jets. Any attempt to apply LDV to ink jets close to real size would potentially present a number of problems, namely resolution, alignment and the effects of surface curvature parallel to the jet axis. Resolution in LDV is limited by the size of the optical probe. The smallest possible probe volume gives the best possible spatial resolution in velocity maps however, a smaller probe volume contains fewer fringes, and it is the number of fringes that dictates the precision with which the modulation frequency and hence velocity can be measured. Without interpolation of the Fourier spectrum of the signal, 100 fringes are required for 1 % uncertainty in the velocity measurement. 1 % is a reasonable limit, since we are concerned with small deviations from the mean velocity when studying ink jets. In a realistic LDV setup (figure 6.15), with a frequency-doubled Nd:YAG (532 nm) laser providing the light source and the beams crossing at a full angle of 70° in the jet, 100 fringes requires a probe volume which extends 50 µm × 35 µm × 28 µm ($x \times y \times z$), large compared to the size of an ink jet stream. It would be possible to illuminate with a shorter wavelength, for example a frequency-quadrupled Nd:YAG

(266 nm) with a probe volume containing 20 fringes and, with interpolation of the spectrum by a factor of five, achieve 1 % uncertainty. The probe would be 5 µm long (in x) in this case, and the resolution would be comparable to that achieved using the holographic method described in this thesis. LDV is only likely to be practical where the surface of the jet can be assumed to be cylindrical. Any curvature in the jet parallel to its axis of symmetry distorts and deflects the beams and any asymmetry in the crossing of the beams tilts the fringes and biases the result toward slower speeds. Deflection of the beams not only moves the probe volume away from its expected location but also causes the beams to cross away from their waist, enlarging the probe volume and reducing spatial resolution. LDV is also likely to be much more sensitive to small changes in the position of the jet since its position must be stable to less than the size of the probe volume whereas the holographic approach is robust to relatively large vibrations in the jet. As long as the sample remains in the field of view (within ±100 μm of the centre of the field of view) velocities can still be measured with the holographic method described in this thesis.

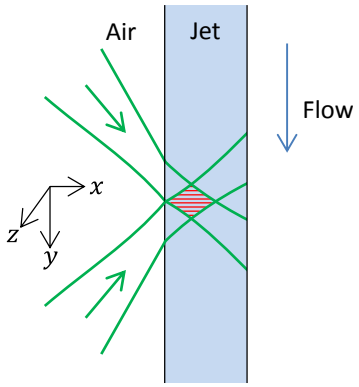

Figure 6.15 A hypothetical LDV experiment on a 100 µm jet, two 532 nm laser beams enter the jet and cross at their waist, creating the interference pattern which acts as the probe. The probe and jet are drawn to scale. The probe volume drawn would contain 100 fringes, but only a few are drawn for clarity.

Particle image velocimetry (PIV), invented around 40 years after LDV, is currently the most prevalent flow measurement technique. Multiple images of seeding particles, illuminated by a plane sheet of light, are recorded and the local movements of particles between images are measured providing a powerful and popular technique whereby a large area of flow can be measured at once. To apply PIV to curved samples a ray-tracing technique may be used to correct the position of the vectors, again requiring

knowledge of the surface and its refractive index. The holographic optical distortion compensation method described in this thesis also requires this information; the shape of the surface is extracted from the same holograms that are used for the velocimetry analysis. The scattered field from a seeded sample is recorded holographically, and then numerically propagated back to the sample surface. This information is used to define the field on a series of sources across the surface which are then propagated inside the sample to fully account for any distortion due to the lensing effect of the curved sample surface.

Flow inside millimetre-scale liquid jets was measured by Castrejon-Pita *et al.*, using a PIV technique with ray-tracing analysis to account for the curvature of the surface.[11] The setup used to record the images is the same as a basic PIV experiment, where the particles within the sample were illuminated by a planar light sheet (< 200 μm thick), and images were recorded with a camera orientated normal to it. The jets studied measured 2.2 mm in diameter and were produced using a scaled-up model of a continuous ink jet print head, and all measurements conducted were confined to the cylindrical part of the jet, from ~1 to ~7 nozzle radii away from the nozzle exit. Correlation analysis was carried out on the images and the positions of the vectors were corrected to compensate for the lensing effect of the jet's surface. Castrejon-Pita *et al.* compared the rate at which flow profiles decayed toward plug flow to a simulation. It is difficult to draw a comparison between my work and theirs as there appears to be a larger discrepancy between the model and their data at larger downstream distances. The eclipsing of the illumination by the nozzle mount on the print head used in my work means that my closest measurements recorded to the nozzle exit are ~14 nozzle radii downstream; this is a drawback of using a focus as the source of illumination. It could be overcome by either modifying the protective plastic nozzle mount or using a different design of microscope if the flow close to the nozzle exit is of interest.

The PIV method could conceivably be scaled down to allow the study of micro-scale liquid jets as it would be possible to illuminate particles with a light sheet with a small depth compared to the diameter of the jet. However, it would not be possible to measure velocities close to the edges of the sample due to refractions at the liquid/air interface. Refraction effectively compresses the light scattered from particles in a relatively large area close to the side onto a relatively small area of the image. The ray-tracing method

of compensation pulls information from the sides of the image towards the centre – it has been found that applying the correction to the velocity data rather than the images provides the most reliable results. As an example of the effect of the refraction on the amount of recoverable data, in a realistic experiment, where a 50 μm radius water jet is imaged with an effective pixel size of 0.5 μm, and 16 × 16 pixel correlation windows, the closest measured vector is centred 4 μm away from the surface in the image. The corrected position however is 12 μm away from the surface; velocity information from the last 24 % radially is therefore lost. In fact, in order to recover velocity in the final 10 % radially, particles need to be reliably detected within the last 0.46 μm before the surface in images. This is not practically possible with visible light and recording high resolution images in the UV poses problems of its own, such as user safety and the cost of UV transmitting imaging optics. The restoration of images or velocity data by a ray tracing method therefore cannot provide access to the flow close to the edges of a sample and this is one area where the holographic method described in this thesis provides an advantage. He and Duan[12] have reported a ray tracing method where velocities near the edge of a curved sample may be measured by tilting the camera with respect to the light sheet, but it has the constraint of requiring a 1:1 imaging system – limiting its usability to objects much larger than the pixels of the camera.

In the curved parts of the jet, I found that, in the reference frame of the jet, fluid flows out of the narrower necking parts of the jet and into the wider swells. This mechanism of jet breakup, where higher Laplace pressure in the narrow parts forces fluid out causing them to become even narrower, is accepted[13] and has been known for over 130 years since its suggestion by Rayleigh.[14] None of the work cited so far in this chapter has attempted measurements where the jet begins to swell and neck. Mansour and Chiger[15] studied a 3 mm diameter water jet with an LDV system capable of recording both the axial and radial components of velocity. Their measurements extended to approximately 70 nozzle diameters downstream from the nozzle where the jet had started to swell and neck. Their results are shown in figure 6.16, showing both the measured axial and radial components of velocity. They quote an error in the radial component of 10-20 %, but it is unclear exactly how the deflection of the probe by the curvature of the jet surface parallel to its axis of symmetry is compensated for. The results of Mansour and Chiger show that the radial component of velocity is close to zero at the neck and at the crest of a swell the radial component is at a maximum and

directed away from the axis of the jet. My findings are broadly in agreement, with the caveat that the errors on the radial component are large for the reasons discussed previously in section 6.1.4.

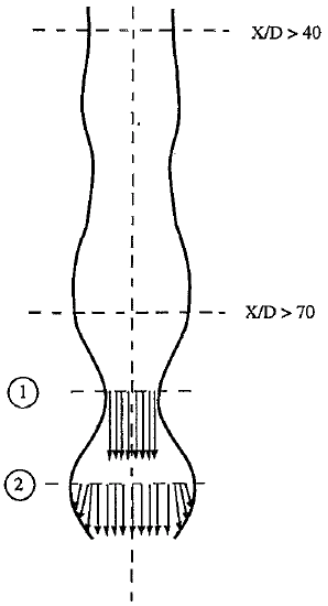

Figure 6.16 Schematic of a jet profile. The ratio X/D refers is the ratio of stream wise distance from the nozzle to the nozzle diameter. Reproduced from reference [15].

There are ways in which the technique used in this thesis could be improved and some fundamental limitations. The limitations are likely to not only affect holographic particle velocimetry but also other particle velocimetry methods since they are due to the interaction between light – either the illumination light or the signal from scattered particles – with the interfaces between the jet medium and the outside world. At a point close to breakup, the surface of the drop is angled very steeply towards the viewing direction and much of the scattered visible light from particles in this region is totally internally reflected making these particles effectively invisible. The same is true of a free spherical drop, very little of the light emanating from particles close to the extremes will reach collection optics.

The limitation with the technique described in this thesis is encountered in instances where the neck thins close to breakup of the jet. There are several contributing factors to this problem. Firstly, as the jet thins, the volume in each axial slice decreases. For a neck of radius 10 μm the volume is around 4 % of its original value and therefore 25×

fewer particles are visible. Particle loading should not however be increased by a factor of 25 to compensate due to the fact that particles inside swells outside of the 'field of view' still contribute to the collected hologram and very high seeding densities will result in a speckle noise problem. If particles in the thinner parts of the neck were visible and yielded usable correlations, then the number of instantaneous measurements could simply be increased to increase the number of particles contributing to the final result. However, correlations in this region do not have a sufficient signal to noise ratio to be included and no velocity vectors could be extracted. I think that the problem lies in the holographic recombinations themselves and could be caused by incorrect positioning of the surface of the neck – because it is smaller a small error in positioning the surface has bigger consequences. Another potential reason is due to the lack of information available to reconstruct the particles in the neck. The front surface of the narrow (<10 μm radius) neck has far fewer points in the numerical reconstruction than the surface of the unperturbed jet. This limits the information available in the reconstruction of particles and perhaps causes the problems with gaining reliable correlations.

6.5 References

1 J. Eggers, 1997, *Reviews of Modern Physics*, 69(3), 865-929.

2 R. J. Adrian, J. Westerweel, *Particle Image Velocimetry*, Cambridge University Press, Cambridge, 2011.

3 S. A. Wormald, J. M. Coupland, 2010, *Journal of Modern Optics*, 57(9), 700-708.

4 J. M. Coupland, J. Lobera, 2008, *Meas. Sci. Technol.*, 19, 074012.

5 A. van der Bos, M-J. van der Meulen, T. Drissen, M. van der Berg, Hans Reinten, H. Wijshoff, M. Versluis and D. Lohse, 2014, *Physical Review Applied*, 1, 014004.

6 D. B. Bogy, 1979, *Ann. Rev. Fluid. Mech.*, 11, 207-228.

7 J. Eggers, E. Villermaux, 2008, *Rep. Prog. Phys.*, 036601.

8 C. McIlroy, O. G. Harlen, N. F. Morrison, 2013, *Journal of Non-Newtonian Fluid Mechanics*, 201, 17-28.

9 C. Tropea, A. L. Yarin and J. F. Foss eds., *Springer Handbook of Experimental Fluid Mechanics Vol. 1*, Springer, 2007.

10 T. Battal, C. D. Bain, M. Weiss, R. C. Darton, 2003, *J. Colloid and Interface Science*, 263, 250-260.

11 J. R. Castrejon-Pita, S. D. Hoath, I. M. Hutchings, 2012, *Journal of Fluids Engineering: Transactions of the ASME*, 134, 011201-12.

12 B. He, F. Duan, *Applied Physics Letters*, 2013, 103, 053508.

13 J. Eggers, E. Villermaux, 2008, *Reports on Progress in Physics*, 71(3), 036601.

14 Lord Rayleigh, 1879, *Proc. London Math. Soc.*, 10(4).

15 A. Mansour, N. Chigier, 1994, *Physics of Fluids (1994-present)*, 6, 3380.

7 Summary and Conclusion

Ink jets precisely deliver tiny quantities of material to exact locations. They have a wide range of applications including graphical printing, 3D rapid prototyping, printing of electronic circuits, as well as emerging techniques like bioprinting.[1,2] Modern inkjet technology is developing rapidly to address new markets requiring new classes of fluid. This project seeks to aid technology development by designing a tool capable of measuring flow inside ink jet streams. The greatest difficulty with measuring velocities non-intrusively in small, tightly curved samples is the optical distortion, due to the change in refractive index, at the interface. We were able to overcome this difficulty using a holographic approach. Holography records both the amplitude and phase of the light scattered from particles, and with this information, the scattered light can be replayed back through a replica of the sample's surface, accounting fully for all refractions. A digital holographic microscope allows this process to be performed, with the help of specialist algorithms, in a fully numerical environment. The particles are located within volumetric 'images' and their velocities are measured by comparing their positions to particles in a second volumetric image taken a short time later.

The microscope developed for this work was a simple off-axis design using a single objective lens, although there is nothing in the mathematics to limit which type of microscope can be used, so long as faithful holograms are recorded. The algorithms used to propagate light inside the sample are based on the mathematical framework developed by Wormald and Coupland.[3] Their method has been validated in this thesis by propagating the light through both interfaces of the sample to reconstruct the original illuminating diverging wave.

Measurements of velocity within continuous ink-jet streams were made both where the stream is cylindrical, and extending towards the point of breakup. The velocity profiles in annular rings were integrated and the mean velocity was found to match the mean velocity obtained from another method, i.e. recording the volume of fluid jetted over a known time. Measurements at moderate swells and necks show that fluid is pumped out of the more tightly curved regions (necks) and into the less curved regions (swells) by Laplace pressure.

The technique developed here has for the first time provided measurements of particle velocity inside a continuous ink-jet stream with a diameter of 100 µm. Previously, particle image velocimetry (PIV), combined with ray-tracing to compensate for curvature, and laser Doppler velocimetry have only been successfully applied to jets of millimetric dimensions. The nozzle sizes of modern ink jets are ~20 µm for drop on demand systems and ~40 µm in continuous ink jets, although the jets studied in this thesis are larger, they are close enough in size that the flow phenomena are likely to be the same as those seen in commercial systems. Without any further adaptations, the technique could be applied to jets containing surfactants and viscosity modifiers to assess their effect on the flow inside the jet and provide insights into break up mechanisms. Another application is flow inside micro-capillaries, with the added complexity that the light propagates through an extra optical interface between the detector and the fluid.

The limitations of the technique result from the need for a very precise estimate of the position of the sample, to allow for the extraction of reliable velocity maps. It is possible to infer the sample position from the information contained within a single hologram, and although this is slow, it only needs to be done once for a single set in the current system as the jet does not move significantly during the time required to accumulate a sufficiently large set of holograms. It may, however, prove useful to include a separate imaging camera, at 90° to the normal recording direction, to accurately record the position of the sample along the holograms optical axis. I believe that this addition will enable a sufficiently accurate positioning of the sample surface in 3D reconstruction, so that it is possible to measure velocity accurately in the parts of the jet where ligaments of fluid thin to less than ~20 µm. Velocity measurements in these areas were not possible using the current system.

Another limitation of the technique is that the radial component of velocity cannot be reliably measured, although it may be possible through a continuity approach if a suitably large number of instantaneous measurements are averaged to produce a finely grained and smooth velocity map. The final limitation arises from the focussing of the incident light by the curved rear (toward the illumination) surface of the jet. The surface acts like a cylindrical lens that focuses the light towards the centre of the jet leaving peripheral dark areas; particles in the dark regions are not illuminated and hence do not

scatter any light onto the detector. These areas do not present a problem in the measurement of jet velocity over the full width of jets as an axisymmetric approximation can be applied. It does however mean that this technique, as well any other particle imaging technique that uses a single direction of illumination, cannot be yield a full map measurement inside free droplets of fluid.

I believe that this thesis presents a useful tool which, in its current state, is capable of reliably measuring the particle velocities inside micro-scale continuous ink jets of transparent fluid, and that this in itself is a valuable tool for the continued development of novel ink jet technologies. Moreover, the equipment required to record the holograms is by no means complex and consist of a single objective lens, a non-polarising beam splitter, three mirrors and a spatial filter (consisting of a pair of singlet lenses and a pinhole). Although the laser and camera used are from a commercial PIV system, this equipment tends to be standard within the labs of those interested in studying fluid flows. In the future, it will be possible to modify the reconstruction algorithms to measure flows within micro-scale capillary tubes. It may also be possible, by including a second purely imaging camera, to record the position of the jet to a high enough precision so that measurements inside a sub-20 μm ligament of fluid are possible.

7.1 References

1 G. D. Martin, S. D. Hoath, I. M. Hutchings, 2008, *Journal of Physics: Conference Series*, 105, 012001.

2 B. Derby, 2012, *Science*, 338, 921-926.

3 S. A. Wormald, J. M. Coupland, 2010, *Journal of Modern Optics*, 57(9), 700-708.